UNIVERSITÀ
DEGLI STUDI
FIRENZE

DOTTORATO DI RICERCA IN SCIENZE CHIMICHE

CICLO XXXIV

COORDINATORE Prof. Piero Baglioni

ELECTRODEPOSITION AND CHARACTERIZATION OF INDUSTRIAL AND TECHNOLOGICAL INTERESTING SURFACES

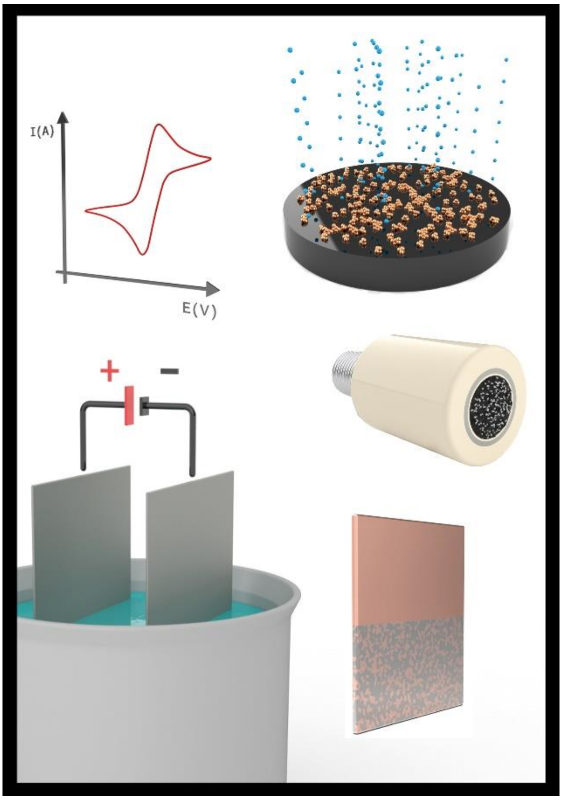

Dottorando
Dott. Lorenzo Fabbri

Tutore
Prof. Massimo Innocenti

Co-Tutore
Dott. Emanuele Piciollo

UNIVERSITÀ
DEGLI STUDI
FIRENZE

DOTTORATO DI RICERCA IN SCIENZE CHIMICHE

CICLO XXXIV

COORDINATORE Prof. Piero Baglioni

ELECTRODEPOSITION AND CHARACTERIZATION OF INDUSTRIAL AND TECHNOLOGICAL INTERESTING SURFACES

Settore Scientifico Disciplinare CHIM/01

Dottorando
Dott. Lorenzo Fabbri

____
(firma)

Tutore
Prof. Massimo Innocenti

____
(firma)

Co-Tutore
Dott. Emanuele Piciollo

____
(firma)

Coordinatore
Prof. Piero Baglioni

____
(firma)

Anni 2018/2021

To my efforts along these three years.

Table of contents

Preface

Abstract

During this *Ph.D.* thesis, I worked to solve two different issues exploring the role of applied electrochemistry in the near future of industrial and technological research. From one side I focused my attention on the energy production from photovoltaic technology. In this context I studied the environmental impact and performances of one of the most widely used processes in the electroplating industry: bronze electrodeposition.

The goal of the work was the obtainment of a copper-tin alloy with 2:1 atomic ratio of the two metals able to be considered a starting point in the obtainment of the Cu_2ZnSnS_4 compound called kesterite via the electrodeposition technique; an intrinsic semiconducting material able to open new alternatives in photovoltaics. The production of kesterite compounds via electrodeposition represents a sustainable and scalable process from an industrial point of view. Nowadays, bronze coatings are widely applied in plating industry to replace nickel films on objects in contact with skin, as a barrier-layer against corrosion. The most popular bronze plating baths are cyanide-based due to their stability over work cycles and deposition performances (deposition rate, film quality, etc.) but they involve issues regarding employees' safety and waste-water disposal. In this context, was developed a cyanide-free bronze plating bath based on methanesulfonic acid as the electrolyte, which is considered environmental-friendly. Bronze coatings obtained from the bath were studied from the compositional, structural, and morphological points of view. The results showed good performance in terms of bath stability, alloy structure, and composition

Modifying the previously studied solution, was formulated a copper plating bath based on methanesulfonic acid. This bath was used as a model-bath, to explore the possibility to understand if an organic additive has a relevant effect on the structure and morphology of an electrodeposited copper film (e.g., brightener) exploiting an "a priori" kinetic study instead of only morphological analysis on the metal coating. Applying the Scharifker-Hills theoretical model to chronoamperometric data was studied the modification by thiourea of the metal film nucleation and growth mechanism, and its effect on the copper surface morphology. Thiourea is known to be a brightener additive in copper deposition. I verified that analyzing the effect of thiourea on the nucleation and growth mechanism of the metal film was possible to optimize its concentration in the solution. Moreover, the comparison between the kinetic data and the morphological analysis on deposited samples showed that the modification of the nucleation mechanism is a key step to tailor the metal structure in order to develop kesterite compounds.

On the other side of my *Ph.D.* thesis, I faced the issue of the sustainability of electrodeposited catalysts for energy production and storage devices such as fuel cells.

In the case of non-PGM-based catalytic surfaces, was studied the enrichment of chars derived from the pyrolysis of waste tyres by the electrodeposition of cobalt, as alternative catalytic material for oxygen reduction reaction in alkaline fuel cells. Applying various deposition conditions was obtained different Co-enriched catalytic chars. RRDE technique was exploited to study the catalytic properties for the oxygen reduction reaction. The enrichment strategy resulted in samples with very good catalytic performances. Moreover, the catalyst obtained showed optimal stability over work time and attractive economic sustainability.

In the case of PGM-based catalytic surfaces, was developed a combined electroless process to produce palladium coatings free of defects and with a tailorable thickness on copper substrates, in order to use minimal quantities of precious metal. Studying two different electroless techniques (displacement plating and chemical plating) I managed to produce nanometered continuous palladium films able to be implemented as catalytic surfaces. Combining the two deposition methods I obtained micrometered palladium films, which constitutes a valid alternative to the electrodeposited ones in the luxury goods plating industry.

Scientific production

Published papers

- Fabbri, L.; Giurlani, W.; Biffoli, F.; Bellini, M.; Miller, H.; Fontanesi, C.; Vizza, F.; Innocenti, M. Exploiting the Combination of Displacement and Chemical Plating for a Tailored Electroless Deposition of Palladium Films on Copper.
  Appl. Sci. 2021, 11(18), 8403 DOI: 10.3390/app11188403
- Passaponti, M.; Lari, L.; Bonechi, M.; Bruni, F.; Giurlani, W.; Sciortino, G.; Rosi, L.; Fabbri, L.; Vizza, M.; Fontanesi, C.; Innocenti M. Optimization study of Co deposition on chars from MAP of waste tyres as green electrodes in ORR for alkaline fuel cells.
  Energies 2020, 13(21), 5646 DOI: 10.3390/en13215646
- Fabbri, L.; Sun, Y. K.; Piciollo, E.; Salvietti, E.; Zangari, G.; Passaponti, M.; Innocenti, M. Electrodeposition of White Bronzes on the Way to CZTS Absorber Films.
  J. Electrochem. Soc. 167 022513 DOI: 10.1149/1945-7111/ab6c59
- Vizza, M.; Giaccherini, A.; Giurlani, W.; Passaponti, M.; Cioffi, N.; Picca, R. A.; De Luca, A.; Fabbri, L.; Lavacchi, A.; Gambinossi, F.; Piciollo, E.; Salvietti, E.; Innocenti, M. Successes and Issues in the Growth of Moad and MoSe2 on Ag(111) by the E-ALD Method.
  Metals 2019, 9, 122 DOI: 10.3390/met9020122
- Salvietti, E.; Giurlani, W.; Foresti, M. L.; Passaponti, M.; Fabbri, L.; Marcantelli, P.; Caporali, S.; Martinuzzi, S.; Calisi, N.; Pedio, M.; Innocenti, M. On the Contrasting Effect Exerted by a Thin Layer of CdS against the Passivation of Silver Electrodes Coated with Thiols.
  Surfaces 2018, 1, 29–42 DOI: 10.3390/surfaces1010004

Papers in progress

- De Beni, E.; Giurlani, W.; Fabbri, L.; Emanuele, R.; Santini, S.; Martellini, T.; Cincinelli, A.; Innocenti, M. Graphene-based nanomaterials in the electroplating industry: a suitable choice for heavy metal removal from wastewater.
- Fabbri, L.; Piciollo, E.; Fontanesi, C.; Giurlani, W.; Mencherini, G; De Luca, A.; Passaponti, M.; Innocenti, M. Effect of Thiourea on the Nucleation and Growth of Copper Electrodeposited from a Methanesulfonic acid-based Solution.

List of abbreviations

CAGR = Compound Annual Growth Rate

PGM = Platinum Group Metals

CZTS = Copper-Zinc-Tin Sulphide

ELTs = End of life tyres

PSA = Phenylsulfonic Acid

MSA = Methanesulfonic Acid

CV = Cyclic Voltammetry

LSV = Linear Sweep Voltammetry

Hyd = Hydroquinone

NTA= Nitrilotriacetic Acid

2-Pic = 2-Picolinic Acid

Cu(II)SFT = Copper(II) Sulfate

Cu(II)MSA = Copper(II) Methanesulfonate

Sn(II)MSA = Tin(II) Methanesulfonate

OCP = Open Circuit Potential

TU = Thiourea

S.H. = Scharifker-Hills

EROEI = Energy Returned On Energy Invested

FC = Fuel Cell

PEM= Proton Exchange Membrane

ORR = Oxygen Reduction Reaction

AEM = Anion Exchange Membrane

RRDE = Rotating Ring-Disk Electrode

PDP = Palladium Displacement Plating

PCP = Palladium Chemical Plating

NPs = Nanoparticles

MAP= Microwave Assisted Pyrolysis

General background and aims

Over the last decades, the interest in scientific and industrial research within the surface coatings field is growing and consolidating. The practice to modulate the surface properties of an object modifying the surface itself instead of the bulk material is worldwide recognized as an advantageous choice in terms of a variety of application techniques and sustainability in terms of industrial scale-up. The function and the composition of the films cover a lot of different fields: dielectrics, (organic, like polymers, or inorganic, such as metal oxides), semiconductors and metals. The application of one or more layers and their thickness depends on the function of the coating. The surface properties obtained by the application of a film lay over a broad range, e.g., corrosion protection, wear resistance, catalytic activity enhancement, semiconducting properties, or aesthetical appearance.

Metals and alloys represent the election materials in the production of coatings facing a wide range of applications from automotive and aerospace to machinery and jewellery. Metal films could be obtained applying different techniques and the more relevant are electrodeposition and physical vapour deposition. The latter method is showing its increasing importance in the coatings research field due to its capability to obtain not only metal films but also metal compounds such as oxides and nitrides which can be applied as functional coatings (e.g., high wear resistance films). Physical vapour deposition is also considered an environmentally safe procedure with reduced risk of potential release of dangerous substances. The main disadvantage lies in the affordability of PVD technology. Electroplating is recognized as a mature procedure to produce metal coatings. The first example of electrodeposition of a metal is due to the Italian scientist Luigi Brugnatelli who, at the beginning of the nineteen-century, managed to produce a gold film over a silver medal exploiting a Volta pile and a gold-complex solution. Since the first method to produce metal films over conductive substrates exposed by Brugnatelli, the interest in the development of the so-called electrodeposition science grew, disclosing the broad field of application of metals and alloys coatings that nowadays plays an important role both in academic research as in the industrial production. The major advantages of electrodeposition with respect to the other techniques of surface finishing reside in the tunability of film properties and competitiveness of large-scale industrialization.

Although the major technological advancements occurred in the past forty years, galvanic electrodeposition accounts today for almost 13 billion USD. Although North America and Western Europe are leading the scenery is estimated that their primary role can be injured by the Asia Pacific region due to the role played by consumer electronics and automobile manufacturers, which have large manufacturing sites in countries like India and China. The Global electroplating market is projected to reach almost 16 billion USD by 2026 with a CAGR (Compound Annual Growth Rate) ≈ of 3%. The fuel that pulls the electroplating market growth is the increasing number of end-use industries that found in the electroplating the suitable way to improve their products, from electronics, automotive, and machinery to luxury goods.

Increasing concerns over dangerous wastes produced during electroplating treatments and price volatility of the highly demanding precious metals could mine the market growth, for this reason, the research, and development in the electroplating field is facing new problems to solve, not only regarding the properties of coatings but also the safety of the processes and the economic sustainability of the materials.

Along with this panorama, this *Ph.D.* thesis is devoted to find a solution regarding these two latter arising problems on two distinct applications of surface science and technology.

From one side I decided to pose my attention to the safety and tunability of the bronze electrodeposition process and on the other side, I worked on the sustainability of electrodeposited catalysts based on PGM and non-PGM for energy production devices.

The spread of the electrodeposition of copper-tin alloys (bronze) as an industrial process can be addressed to the use of cyanide-based baths. This type of solution is still the most widely used today in large-scale-plating because the cooperation of copper cyanide and sodium cyanide simplifies the co-deposition of copper and tin guarantying the stability of the bath. The presence of cyanide represents a concern which researchers are struggling to solve preserving the properties of the traditional cyanide-based solutions and of the alloy coatings obtained. In this sense, during my *Ph.D.* I developed a novel bronze electrodeposition solution with the aim to overcome the mentioned issues. The development of green copper-tin alloy plating baths with tailored performances is a new step on the way to obtain a sustainable class of semiconducting materials called kesterite or CZTS which represent an alternative to the traditional doped silicon devices. kesterite is currently the most promising emerging fully inorganic thin film photovoltaic technology based on critical raw-material-free and sustainable solutions.

Part of the work sought to improve the deposition process of pure copper in order to reduce the environmental impact for an increasingly eco-sustainable production, and to tailor the metal structure in view of the development of semiconducting materials. In galvanic industry copper plating is a very important treatment and is often the first and irreplaceable step in the electrodeposition of metal films such as bronze for both technological and decorative purpose.

To improve this well know process I studied a new formulation based on the methanesulfonic acid electrolyte, and I explored the effect of an organic brightening agent on the nucleation and growth of copper films on the way to obtain a performant deposition solution.

On the other hand, in parallel with the transition from fossil fuels to alternative energy sources and the always more restrictive environmental standards for fossil fuel engines, an arising problem can be solved with the help of new functional coatings. One of the best promising alternatives to fossil fuels is hydrogen, considered the greenest fuel possible (due to its famous combustion product: water!). Fuel cells represent the device by which chemical energy can be converted into electrical energy. This type of device studied since the late '30s of the twentieth century presents some issues which researchers tried to overcome over the decades. One of the major concerns is the electrode materials, which are the key to the efficiency of the cell. In terms of performance, PGM are the election materials for fuel cell electrodes, but the increasing cost and shortage of these materials pulled researchers to find alternative solutions. In this perspective, I proposed two distinct strategies: in the effort to use non-PGM materials were tested chars derived from the microwave-assisted pyrolysis of end-of-life tires (ELTs) as a sustainable substrate on which cobalt was deposited to produce green electrodes in ORR for alkaline fuel cells. In the case of the use of PGM materials was tried to optimize the deposition of palladium thin films on copper via electroless techniques. These types of techniques, involve redox reactions and allows the production of thin and ultra-thin metal films through an easy-access procedure. In this way, were tried to tailor the catalytic properties of a copper substrate using a competitive amount of precious palladium. This procedure resulted interesting also from an industrial point of view for luxury accessories and jewellery, where palladium is used as an intermediate layer or top layer. Palladium films obtained from an electroless deposition could open the doors to a more cost-effective industrial process respect to the electrodeposition one.

1 Towards an innovative bronze plating process

1.1 Introduction

Bronze plating baths can be divided in two main categories: cyanide-based solutions and cyanide- free solutions. The first category represents the oldest and tradition type of formulations developed for the deposition of bronze coatings. In cyanide baths copper is dissolved as cyanide complex while tin can be found in different forms such as stannate or tin pyrophosphate, in most cases. The other components of a typical commercial bath are sodium or potassium cyanide, hydroxides, and brighteners which could be both organic compounds, inorganic compounds, and small amounts of metal ions (such as zinc, lead or bismuth ions). From an industrial standpoint the first time that this type of bath became important for the plating sector was after the second world war when the shortage of nickel forced plating companies to find a valuable alternative for corrosion protection, decorative purposes, and sub-coats for chrome plating. Nowadays, bronze plating is facing a new interest from plating industries (decorative plating companies) due to the concerns arise from the risk of allergies caused by nickel in applications where this material could go in contact with human skin. Some countries have already released a specific regulation on this topic as in the case of the European community who banned objects with a Ni release higher than 0.5 $mg \cdot cm^{-2} \cdot week$ (UNI EN 1811:2011).

In contrast with the undoubted advantages of bronze plating (i.e., corrosion protection and application as under-coat in decorative plating), its use is not free from problems such as a content of 15-60 g/L of free cyanide in the deposition baths, which represents an issue to the safety of galvanic plant technicians and to the disposal of exhausted solutions. Although inexpensive compared to coatings of noble metals, bronzing process is characterized by high production costs (approximately double the industrial deposition of nickel). To overcome these problems, a lot of work was done in the past fifteen years. Acid baths based on sulphates [1–4], but also on pyrophosphate [5], and oxalates [6], which represent the conventional matrices for copper deposition, were extensively studied. Similarly, formulations obtained as upgrades of solutions used for the deposition of tin were studied, as in the case of phenylsulfonic acid (PSA) [7], but alkaline baths free from cyanides have also been developed [8]. In recent years, a particularly studied electrolyte has been methanesulfonic acid (MSA) which, thanks to its advantages, is excelling over all electrolytes studied so far. MSA has proved to be an ideal electrolyte for many electrodeposition processes, being convenient from a chemical and economic point of view. Among its advantages, the high solubility of metal salts, the low oxidizing power both towards organic compounds and metal ions and the conductivity of its aqueous solutions. In this regard, it is important to emphasize that, the conductivity of the solution from which the electrodeposition is made, is a fundamental parameter to guarantee good process performances. Last but not least important, this electrolyte is also extremely advantageous from an environmental point of view since, being part of the natural sulphur cycle, it is considered a biodegradable product [9]. As regards the precursors of the two metals to be deposited, the salts used vary according to the electrolyte solution chosen. In the case of the acidic baths, chlorides were used for pyrophosphate-based baths, while the sulphate salts of metals were widely used for sulfuric acid, phenylsulfonic acid, oxalic acid and methanesulfonic acid baths. In the case of the latter electrolyte, methanesulfonate salts have also recently been used. In all the baths described so far, many additives must be used to achieve uniform and shiny coatings. Organic substances were historically chosen empirically. The effect of adding additives on the electrodeposition process and the quality of the obtained coatings is determined by the nature of the organic compound and its content in the bath. For example, additives such as polyethers or polyesters are added to sulphate-based baths as they act as wetting agents and inhibitors (levelling agents) [1,2] producing smooth surfaces. Furthermore, a second organic substance containing double bonds or aromatic rings is usually used as a brightener to obtain glossy and shiny coatings [2]. This is the case of benzyl alcohol, which was used to obtain bright bronze coatings with 20%$_{wt}$ tin [10], and of benzaldehyde, whose effect on sulphate electrolytes was studied by Survila et al as already cited. To promote adsorption on the cathode surface it is necessary to use additives containing a positively charged group, the most used is the amino group. In this regard, Kasach et al recently studied the effect of additives, containing amino groups, for the electrodeposition of the Cu-Sn alloys in an oxalic acid bath. They demonstrated that the introduction of trimethylammonium chloride and N-octylpyridinium bromide inhibits the deposition of tin and promotes the formation of shiny coatings containing 24.4-35.8%$_{wt}$ of Sn; on the contrary, the presence of N-benzylpyridinium bromide intensifies the cathodic reduction of tin leading to the formation of opaque coatings containing up to 42.5%$_{wt}$ of Sn [6]. The large difference between the reduction potentials of Cu^{2+} and Sn^{2+} ($\Delta E = 0.5$ V) represents a criticality for the co-deposition of the two metals.

$$Cu^{2+} + 2e^- = Cu \qquad E_0 = +0.34 \text{ V vs. SHE}$$

$$Sn^{2+} + 2e^- = Sn \qquad E_0 = -0.14 \text{ V vs. SHE}$$

In the last decade it has been observed how EDTA (ethylenediaminetetraacetic acid) is able to complex the Cu^{2+} and Sn^{2+} ions in sulfuric acid-based solutions whose pH have been adjusted by adding NaOH (pH = 3.4), obtaining a deposition of tin which varies from 27%wt to 60%wt depending on the applied potentials [4]. An alternative to endorse the potential gap problem has been the development of new baths based on electrolytes used commercially for the electroplating of tin, for example phenylsulfonic acid (PSA)[7]. In this regard, Bengoa et al. studied a PSA bath containing $CuSO_4$ and $SnSO_4$ using Diphone VI (D6) (a sulfonated compound containing aromatic rings) and benzyl alcohol as additives. These additives synergistically increase the deposition of tin and make it possible to obtain, with an efficiency of 92%, bronze coatings containing up to $22\%_{wt}$ of tin [7]. In recent years, several methanesulfonic acid-based baths have been formulated. Although MSA has a poor oxidizing power, compared to other acids, the oxidation of stannous tin to stannic still represents a problem in systems based on this electrolyte. For this reason, antioxidant compounds are usually included in galvanic baths to inhibit the formation of stannic oxide. Recently some authors have proposed the use of hydroquinone as an antioxidant for Sn^{2+}, thus obtaining the deposition of the desired percentage of Sn for the formation of the bronze (Cu-Sn) and white bronze (Cu-Sn-Zn) alloy. In 2013, Pewnim and Roy [11] had obtained bronze deposits containing $96\%_{wt}$ of tin using MSA as electrolyte (pH=1.17), hydroquinone as antioxidant and with the support of commercial perfluorinated surfactants (DuPont™ ForaFac® 1098). In this regard, some studies [11–13] report how the use of the perfluorinated cationic surfactants has no effect on the deposition potential of tin but, at the ideal concentration of $0.01\%_{vol}$, facilitates Cu-Sn co-deposition making the deposition potential of copper more negative, as well as limiting the development of hydrogen. Low et al. also studied the effect of hydroquinone on slowing the oxidation of the Sn^{2+} ion to Sn^{4+} generated on the anode [14]. The development of innovative electroplating baths for the electrodeposition of bronze and white bronze has become a very coveted and defended brand also from the point of view of intellectual property, which is why the panorama of patents dealing with this topic has become very vast. Patent US 7,780,839 B2 [15] reports the use of mercaptans (mercaptotriazoles and mercaptotetrazoles) as stabilizers of metal ions in their lowest oxidation states, using H_2SO_4 or MSA as matrices. These compounds favour the formation of uniform deposits and, with the support of other organic additives such as antioxidants, chelators, brighteners, grain refiners and wetting agents, allow to obtain excellent white bronze deposits. On the same line, subsequent patents, such as the American one US 9,145,617B 2 [16] ,report the use of mercaprotriazoles and mercaptotetrazoles together with other organic additives, for a performing deposition of white bronze starting from Cu(II) and Sn(II) or, in the case of the recent patents US20160298249A1 and EP3002350B1 [17,18], also starting from Cu (I). In the cited patents, among the mercaptan compounds, 1-(2-dimethylamino-ethyl)-5-mercapto-1,2,3,4-tetrazole and 5-ethyl-3-mercapto-4-phenyl-1,2,4-triazole were the most widely used mercaptotetrazoles and mercaptotriazoles, respectively.

In addition to constant current and potential techniques, alloy deposition may be carried out in pulsed mode, where the current density or potential may be alternated between set values. Higher throwing power deposition can be realized by applying pulse plating, leading also to deposition on irregular shapes and surfaces that can be effectively levelled up. These is the case of the work by Beattie and Dahn where they tried to obtain Cu-Sn multi-layered structures using pulsed electrodeposition from a commercial tin plating bath enriched with a copper salt [19] and the recent work by Zanella et al. [20] where the effect of pulsed deposition parameters and anodic materials was studied for the optimization of the electrodeposition process of the Cu-Sn alloy in an acid bath of MSA, thus evaluating the quality of the deposit also in terms of corrosion resistance. In this regard, a recent work by the Applied Electrochemistry group of the University of Florence, published by Berretti et al. reported a comparative study on corrosion resistance in an aqueous solution of 3.5% NaCl of two white bronzes, Zn-bearing and Zn-free, respectively with or without zinc [21]. The results showed that corrosion occurs with two different mechanisms, and that the Zn-free white bronze alloy shows greater resistance to corrosion in this environment. Recently Rosley et al. studied the effect of different complexing agents on the deposition of the Cu-Sn-Zn ternary alloy on a carbon substrate, starting from an aqueous solution in which chloride salts as precursors of the three metals and sodium hypophosphite as reducing agent were dissolved. They observed that by adding 0.20M sodium formate it was possible to deposit a uniform and smooth ternary alloy [22].

1.1.1 Bronze plating in photovoltaics

The development of different strategies to overcome the problems of traditional bronze plating has opened the doors also to innovative properties of the coatings from a chemical and physical point of view. The ability to realise controlled deposit morphology, composition and structure has been improved by newer electrolytes, improved electrolyte additives and pulse plating. Traditional uses of tin-copper alloy deposition have included jewellery and antique finishes, speciality electronics and bearings.

One of the more ambitious application of bronze electroplating is the production of a semi-conducting material as a sustainable alternative to doped-silicon for photovoltaic application. The solar photovoltaic (PV) market in recent times has steadily grown, achieving at the end of 2018 a global operating capacity of 520 GW ; this may play an important role in electricity generation in a few countries, but still does not contribute a sizeable fraction of the global energy needs, being capable of producing roughly 4% of the worldwide electricity [23]. Various reasons contribute to the limited adoption of PV technology. Silicon solar cells currently make-up ~ 85% of the PV market [24] but are still more expensive (per unit energy produced) than conventional energy sources. Thin-film chalcogenides present advantages over Si, as they feature a direct bandgap that results in a high absorption coefficient ($\alpha > 104$ cm^{-1}) [25], and lower sensitivity to grain-boundary recombination, allowing the use of thinner and polycrystalline materials, thus decreasing raw materials and manufacturing costs. CdTe [24] and chalcopyrite $CuInGa(S,Se)_2$ [26] based devices exhibit high efficiency (up to 22.9 %) [27], but recently have experienced limited growth, due to the fact that these technologies rely on relatively rare elements in the earth's crust (In, Te) [28], and/or to the toxicity of Cd, whose use is subject to stringent regulations. An alternative material for PV absorbers made up of abundant elements only, stable in air, and with demonstrated > 10% efficiency [29] are thecompounds Cu_2ZnSnS_4/$Cu_2ZnSn(S, Se)_4$ (CZTS/CZTSSe) [30].

While CZTS/CZTSSe crystallize in various structures, the thermodynamically stable one is the kesterite structure [31]. Both CZTS and CZTSSe exhibit a direct bandgap of 1.4 – 1.5 eV, p-type doping (1015 to 1020 cm^{-3}) controlled in part by stoichiometry [32], and most importantly the low sensitivity to grain boundary recombination. Despite these characteristics, CZTSSe which is more efficient than CZTS [33], has so far reached an efficiency of only 12.6 % [34]. The inferior performance is usually ascribed to the complexity of this compound and the limited stability range of the chemical potential of the constituent elements. Various electrodeposition methods [35] have been targeted a pure kesterite phase [36], which aimed for pure phases and ideal stoichiometry, also using a top electrode to avoid gravity effects [37,38]. While the overall target is the electrodeposition of Cu_2ZnSn precursor films for a CZTS/CZTSSe absorber, in this work was sought to develop a novel, low environmental impact electrodeposition bath capable to reliably form a smooth, dense Cu-Sn alloy with a 2:1=Cu:Sn stoichiometry.

This novel Bronze (Cu-Sn alloy) electrodeposition formulation avoids the use of cyanide as a complexing agent; this is in contrast with current industrial bronze deposition baths which include highly concentration cyanide (15-60 g/L) [39]. Moreover, methanesulfonic acid (MSA) was used both as the electrolyte and complexing agent. MSA is a useful compound from various points of view [9]; it is biodegradable (undergoes the sulphur natural cycle), it shows poor oxidizing behaviour against metal ions and organic compounds and features a conductance comparable with that of commonly used acids.

1.2 Development of a new green formulation for bronze plating

In this section will be presented the development of an innovative formulation for the deposition of copper-tin alloy (bronze). This work represents the first step for the obtainment of the previous mentioned kesterite compound, a sulphurated Cu-Zn-Sn alloy with a stoichiometric ratio of the metals equal to 2:1:1. The solution developed during this *Ph.D.* thesis also represent a valid alternative to traditional bronze plating baths being a sustainable cyanide-free formulation.

1.2.1 Experimental

1.2.1.1 Electrodeposition of copper-tin alloys

Throughout the development of the various formulations, to find the best one, various additives and ion precursors have been investigated, with the aim to identify the best combination in terms of electrochemical performance and bath stability. The reagents used for the proposed deposition baths and their abbreviations are listed in Table 1.1. Note that the water utilized in all the experiments had a maximum conductance of 3 $\mu S \cdot cm^{-1}$. The films studied were deposited on Cu–Zn(bulk)/Ni(~20 μm)/Au(~0.5 μm) substrates and from various electrolytes, as detailed in Table 1.2. Deposition areas were controlled by immersion area of the substrates in the deposition baths. Voltammetric analyses were carried out in a three-electrode cell using a 3 × 0.5 cm^2 polycrystalline platinum plate working electrode and a 9 × 2 cm^2 polycrystalline platinum plate counter electrode. The tests were performed with a Metrohm Autolab mod. PGSTAT302N Potentiostat/Galvanostat computer-controlled by Nova® 2.1.4 software (Metrohm) using Ag|AgCl

(0.197 V vs SHE at 25 °C and KCl sat.) electrode as reference, with respect to which all potentials recorded in this study are referred. The potential range for cyclic voltammetry (CV) measurements started at −0.7/−0.8 V to +1.0 V and return, with a scan rate of 50 $mV\cdot s^{-1}$[40]. Samples grown under potentiostatic conditions were made using the PGSTAT302N applying a potential in the range from −0.25 V to −0.65 V. Samples obtained under galvanostatic conditions were grown using an ELC bench power supply mod. ALR3002M (voltage undulation < 3 mV peak to peak or 1 mV RMS and current undulation < 1 mA RMS [41]) ranging from 0.865 $A\cdot dm^{-2}$ to 2.173 $A\cdot dm^{-2}$ (corresponding to a current range from 0.039 A to 0.163 A). The range of potentials and consequently of current densities had been selected to cover a wide range of electrochemical conditions of metal deposition and study the evolution of the film composition and crystalline structure.

Reagent	Supplier	Purity grade	Abbreviation
Methanesulfonic acid	Sigma Aldrich	Reagent Plus ≥ 99%	MSA
Hydroquinone	Sigma Aldrich	Reagent Plus ≥ 99%	Hyd
Nitrilotriacetic Acid	Sigma Aldrich	Sigma Grade ≥ 99%	NTA
2-Picolinic Acid	Sigma Aldrich	≥ 99%	2-Pic
Copper Sulfate heptahydrate	A.M.P.E.R.E. s.r.l	technical grade	Cu(II)SFT
Copper(II) Methanesulfonate	Todini & co. s.p.a.	Solution 125 g/l, technical grade	Cu(II)MSA
Tin(II) Methanesulfonate	Todini & co. s.p.a.	Solution 300 g/l, technical grade	Sn(II)MSA

Table 1.1 - Reagents of the experiment.

#	MSA	Hyd	NTA	2-Pic	Cu(II) SFT	Cu(II) MSA	Sn(II) MSA	pH
1	200 ml/L (3,08 M)	10 g/L (0.09 M)	20 g/L (0.105 M)	-	11 g/L (0.17 M)	-	11 g/L (0.09 M)	<1
2	200 ml/L (3,08 M)	10 g/L (0.09 M)	-	20 g/L (0.105 M)	11 g/L (0.17 M)	-	11 g/L (0.09 M)	<1
3	200 ml/L (3,08 M)	10 g/L (0.09 M)	20 g/L (0.105 M)	1 g/L (0.01 M)	11 g/L (0.17 M)	-	11 g/L (0.09 M)	<1
4	200 ml/L (3,08 M)	10 g/L (0.09 M)	20 g/L (0.105 M)	1 g/L (0.01 M)	-	11 g/L (0.17 M)	11 g/L (0.09 M)	<1
5	200 ml/L (3,08 M)	10 g/L (0.09 M)	-	20 g/L (0.105 M)	-	11 g/L (0.17 M)	11 g/L (0.09 M)	<1
6	200 ml/L (3,08 M)	10 g/L (0.09 M)	20 g/L (0.105 M)	1 g/L (0.01 M)	-	11 g/L (0.17 M)	22 g/L (0.18 M)	<1

Table 1.2 - Prototypes composition.

1.2.1.2 Materials characterization

The SEM images and alloy compositions were acquired from a FEI Quanta 650 with an Energy Dispersive Spectroscopy (EDS) attachment, with an acceleration voltage of 20 kV. The interaction of the 20 keV electron beam with $Cu_{0.5}Sn_{0.5}$ film was simulated using Casino v2.4821 with 50000 electrons.

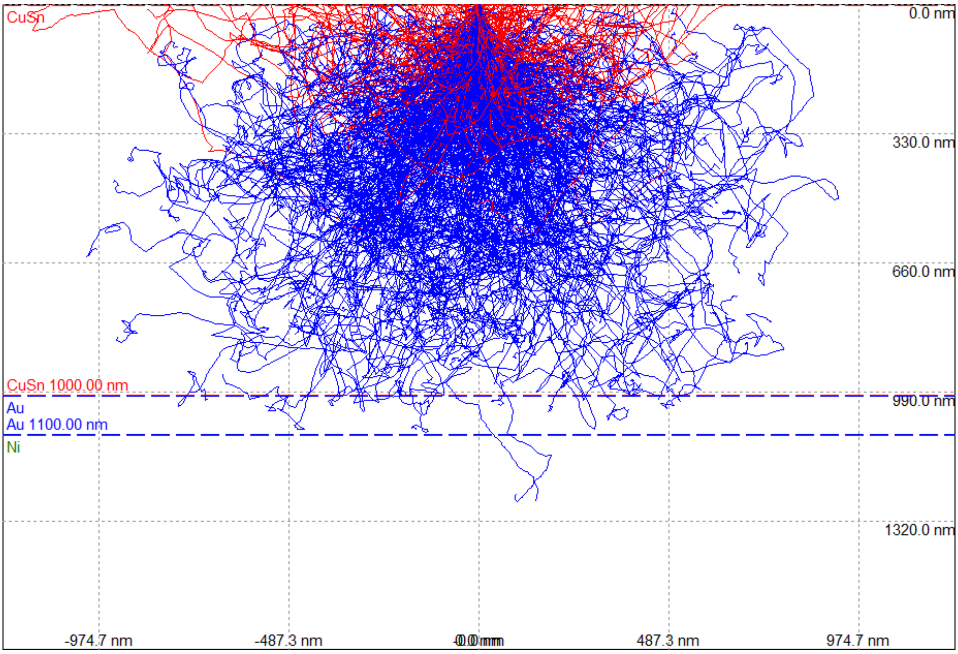

Figure 1.1 - Interaction volume of 20keV e-beam with $Cu_{0.5}Sn_{0.5}$, with red trace indicates backscattered electrons and blue traces for secondary electrons.

The thermodynamics of the Cu–Sn system was calculated by a custom-made Python program, with the energetic and entropic data extracted from references[42,43] while the crystallographic analyses were conducted using the CrystalMaker suite [44,45] combined with the Inorganic Crystal Structure Database (ICSD) [46] The X-ray Diffraction patterns were collected in the $\theta-2\theta$ (Bragg-Brentano) configuration, using a PANalytical Empyrean X-ray diffractometer with Cu Kα as the source (dual-wavelength $l_{K\alpha1} = 0.1540$ nm, $l_{K\alpha2} = 0.1544$ nm, $I_{K\alpha2}$: $I_{K\alpha1} = 0.5$). The cross-sectional views of the samples were prepared by gluing the deposit with Si wafer pieces as the protective counter by Crystalbond™ (Ted Pella) at the temperature of 150 °C for 30s. The samples were then mechanically clamped, followed by a conventional grinding-polishing recipe and setup, finished with 1 μm diamond paste. The Si support was removed mechanically at 150 °C within 30s, while the residue Crystalbond was cleaned by immersing in acetone and methanol for 6 h each.

1.2.1.3 Preparation of prototype baths

Each bath prototype was prepared adding the constituents in the presenting order in Table 1.2 from left to right, under stirring and at ambient temperature, except for the NTA, where the system had been warmed to 50 °C to accelerate its dissolution. The solutions were prepared utilizing MSA as the supporting bath, resulting in all solutions having pH < 1. Prior to the study of the complete formulations, some preliminary tests were carried out to understand the physicochemical and electrochemical behaviour of the constituents. During these tests it was observed that the dissolution of nitrilotriacetic acid in the water/MSA system gave an unstable solution as reported in the literature. However, under the presence of hydroquinone, NTA was dissolved, and the solution was observed to be stable, which had never been reported to the best of my knowledge. The change in the solubilization behaviour of NTA could be due to intermolecular weak interactions between NTA and hydroquinone, which may facilitate the dissolution of the commonly water-insoluble nitrilotriacetic acid.

1.2.2 Results

1.2.2.1 Cyclic voltammetry results

Cyclic voltammetry (CV) was used to qualitatively assess the redox potential peaks for each metal ion, while varying formulation with the aim to minimize the separation among the cathodic peaks. The CVs were carried out between -0.7 V and 1 V. The initial metal precursor couple being studied were Cu(II)SFT and Sn(II)MSA. Two types of organic additives had been used in this first formulation: hydroquinone and nitrilotriacetic acid. Hyd acts as an antioxidant, helping to avoid tin precipitation as tin oxide or hydroxide [14].

Hyd oxidizes to benzoquinone (Fig. 1.2), preventing the oxidation of Sn^{2+} to Sn^{4+}, through the appropriation of the electrons derived from the oxygen solubilized in water.

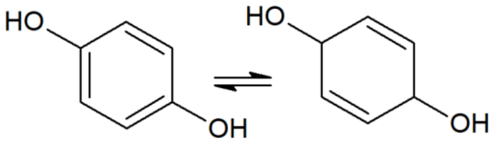

Figure 1.2 - Hydroquinone/benzoquinone couple.

Its action could be easily explained by the simple redox reactions as follows:

$$2C_6H_4OH_2 \rightarrow\ 2C_6H_4O_2 + 4H^+ + 4e^-\ E^0 = +0.699\ V_{vs\ SHE}$$

$$O_2 + 4H^+ + 4e^- \rightarrow 2H_2O\ E^0 = 1.299\ V_{vs\ SHE}$$

NTA (Fig. 1.3) is a chelating agent, which at acidic pH values forms univalent complexes with copper and allows a two-monoelectronic steps mechanism for the reduction of Cu^{2+} ions [47–49].

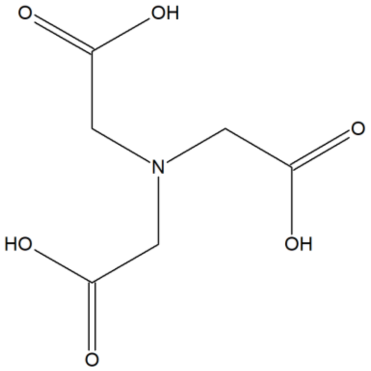

Figure 1.3 - Nitrilotriacetic acid structure.

The two following reactions could explain the chelating behaviour of NTA:

$$Cu^{2+} + NTA^- \rightarrow [Cu(NTA)]^+\ \ pK_{stab1} = 12.96$$

$$[Cu(NTA)]^+ + NTA^- \rightarrow [Cu(NTA)_2]\ \ pK_{stab2} = 4.3$$

Using the above components, was formulated the prototype formulation #1 (see Table 1.2).

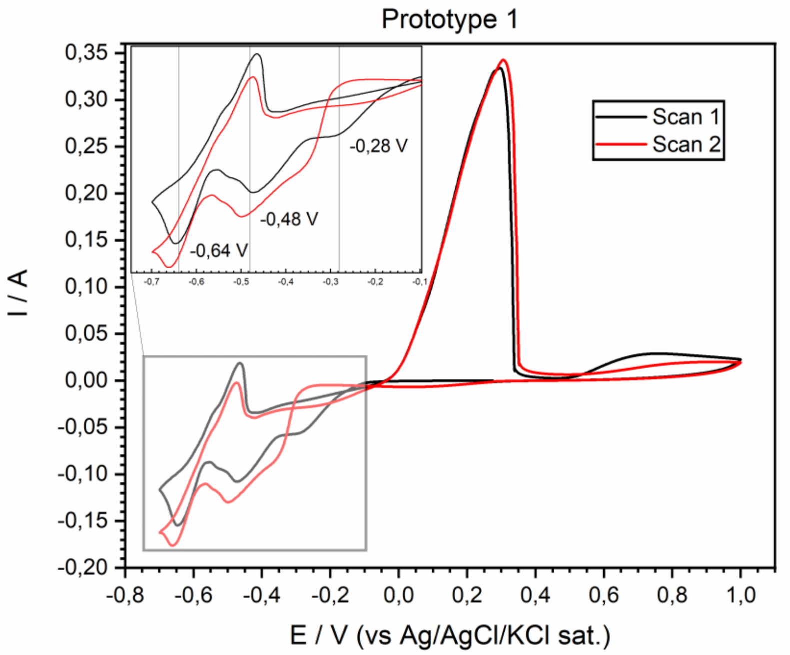

Figure 1.4 - Cyclic Voltammetry (50 mV/sec) of prototype # 1

Figure 1.4 depicts the CV diagram due to the combined redox processes of Hyd, copper, and tin. The cathodic direction of the first scan (black line) showed two reduction peaks of copper with $V_{p,c}$ = -0.28 V, a peak at -0.48 V (highlighted in the inset) due to two-monoelectronic-steps mechanism assigned to NTA, and the tin reduction peak with $V_{p,c}$ = -0.64 V. In the anodic direction the tin oxidation peaks at $V_{p,a}$ = -0.46 V, copper oxidation occured at $V_{p,a}$ = +0.3 V, and a broad signal was obtained due to the oxidation of Hyd to benzoquinone with $V_{p,a}$ = +0.74 V. In the second scan a peak appeared at $V_{p,c}$ = 0.00 V, corresponding to the broad reduction of benzoquinone. From an electrochemical point of view this solution appeared to be suitable to produce alloy samples, because the reduced separation between the second copper reduction peak ($V_{p,c}$ = -0.48 V) and the tin reduction peak ($V_{p,c}$ = -0.64 V) made them overlap, obtaining a range of potentials in which the two elements could co-deposit. Deposits from this bath prototype however were not made, because within a few days this solution formed a white precipitate (probably $Sn(OH)_4$) suggesting limited and unsuitable stability.

To improve the bath stability, was investigated a different complexing agent, 2-Picolinic Acid.

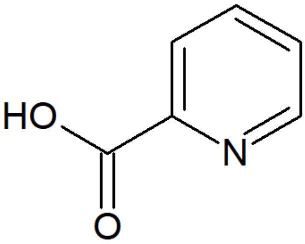

Figure 1.5 - 2-picolinic acid structure.

The two following reactions explain the chelating behavior of 2-Pic:

$$\mathrm{Cu^{2+} + Pic \rightarrow [Cu(Pic)]^{2+} \quad pK_{stab1} = 8.6}$$

$$\mathrm{[Cu(Pic)]^{2+} + Pic \rightarrow [Cu(Pic)_2]^{2+} \quad pK_{stab2} = 7.4}$$

2-Pic is another Copper chelating agent [50], which allows one dielectronic-step mechanism for the reduction of Cu^{2+} ions [51]. Two different electrolyte formulations utilizing this molecule were produced (prototypes #2 and #3), allowing studies of bath stability and the behaviour of Cu^{2+} ions. Bath prototype #2 contained only 2-Pic, while prototype #3 contained both compounds.

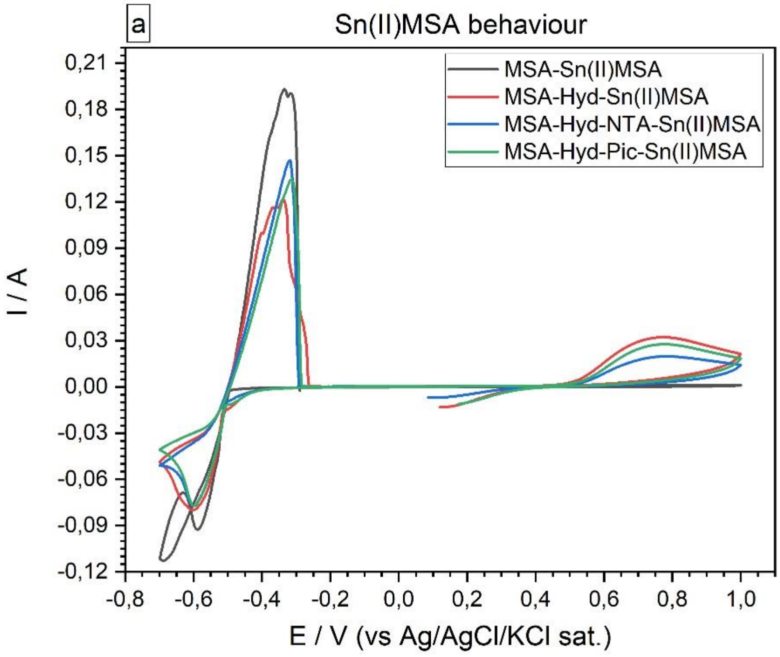
a
Sn(II)MSA behaviour
MSA-Sn(II)MSA
MSA-Hyd-Sn(II)MSA
MSA-Hyd-NTA-Sn(II)MSA
MSA-Hyd-Pic-Sn(II)MSA
I / A
0,21
0,18
0,15
0,12
0,09
0,06
0,03
0,00
-0,03
-0,06
-0,09
-0,12
-0,8
-0,6
-0,4
-0,2
0,0
0,2
0,4
0,6
0,8
1,0
E / V (vs Ag/AgCl/KCl sat.)

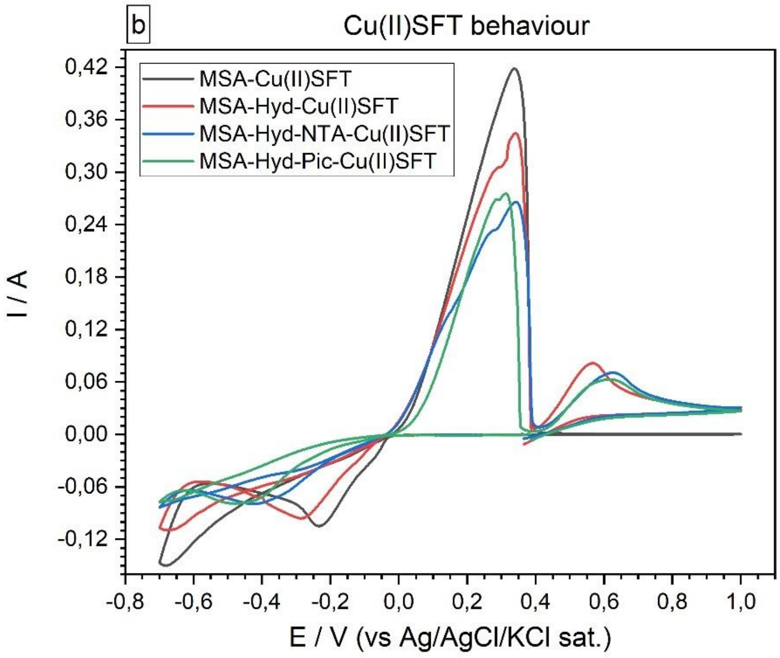
b
Cu(II)SFT behaviour
MSA-Cu(II)SFT
MSA-Hyd-Cu(II)SFT
MSA-Hyd-NTA-Cu(II)SFT
MSA-Hyd-Pic-Cu(II)SFT
I / A
0,42
0,36
0,30
0,24
0,18
0,12
0,06
0,00
-0,06
-0,12
-0,8
-0,6
-0,4
-0,2
0,0
0,2
0,4
0,6
0,8
1,0
E / V (vs Ag/AgCl/KCl sat.)

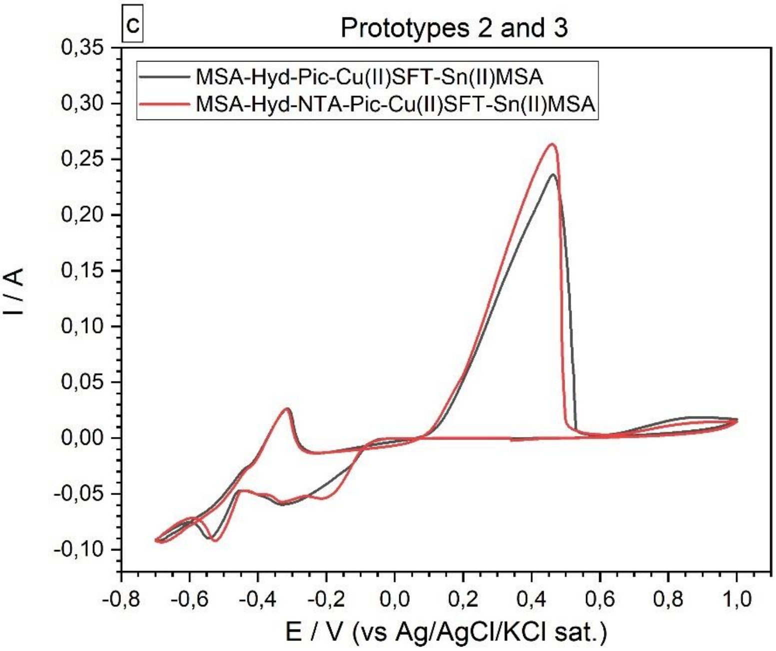

Figure 1.6 - Cyclic voltammetry comparison (50 mV/sec) of single metal precursor (a) and (b) formulations versus protypes formulations # 2 and # 3 (c).

As can be seen in the CV of single metal precursor formulations (Figures 1.6.a and 1.6.b), the addition of Hyd affected the electrochemical behaviour of both metallic ions in solution, while NTA and Pic interacted only with copper ions. Figure 1.6.a (Sn(II)MSA solutions data) shows that Hyd reacted both as an Sn^{2+} complexing agent and as a hydrogen discharge inhibitor, while NTA and 2-Pic did not have an appreciable effect on Sn^{2+} electrochemical behaviour. Figure 1.6.b shows the activity of organic additives on Cu(II)SFT ions. As shown in the voltammograms, Hyd had a retarding effect both on the onset cathodic potential and the peak current potential of Cu^{2+} ions, but the addition of NTA and 2-Pic resulted in a greater shift on the cathodic peak potential of these ions.

Figure 1.6.c compares the CV of the two alloy deposition baths. These results illustrated that the cooperation of NTA and Pic caused a splitting of the copper reduction peak, suggesting a difference in the Cu reduction mechanisms due to different complexing agents. As can be deduced from Figs. 1.6.a and 1.6.b, NTA presented a similar effect to 2-Pic, affecting the redox potentials of both Cu^{2+} and Sn^{2+}. Thus, the differences observed in the redox potential of metal species in the alloy deposition formulations (Fig. 1.6.c) with respect to the single metal precursor formulations (Figs. 1.6.a and 1.6.b) were probably related to enthalpic interactions induced by alloying [52]. The use of two complexing agents also resulted in the improvement of bath stability.

Both solutions showed limited stability, so an alternative combination of metal precursors were tested to further improve stability. Specifically, Cu(II)MSA was used in place of Cu(II)SFT as a precursor , thus formulating two additional prototypes. These two solutions were listed as #4 and #5, and their additive composition was comparable with that of prototypes #2 and #3 (see Table 1.2).

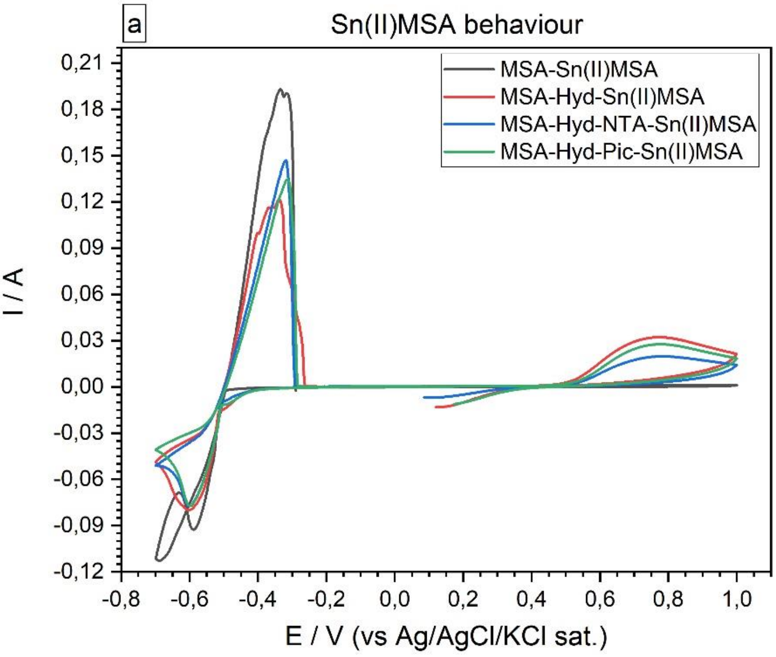
a
Sn(II)MSA behaviour
MSA-Sn(II)MSA
MSA-Hyd-Sn(II)MSA
MSA-Hyd-NTA-Sn(II)MSA
MSA-Hyd-Pic-Sn(II)MSA
I / A
0,21
0,18
0,15
0,12
0,09
0,06
0,03
0,00
-0,03
-0,06
-0,09
-0,12
-0,8
-0,6
-0,4
-0,2
0,0
0,2
0,4
0,6
0,8
1,0
E / V (vs Ag/AgCl/KCl sat.)

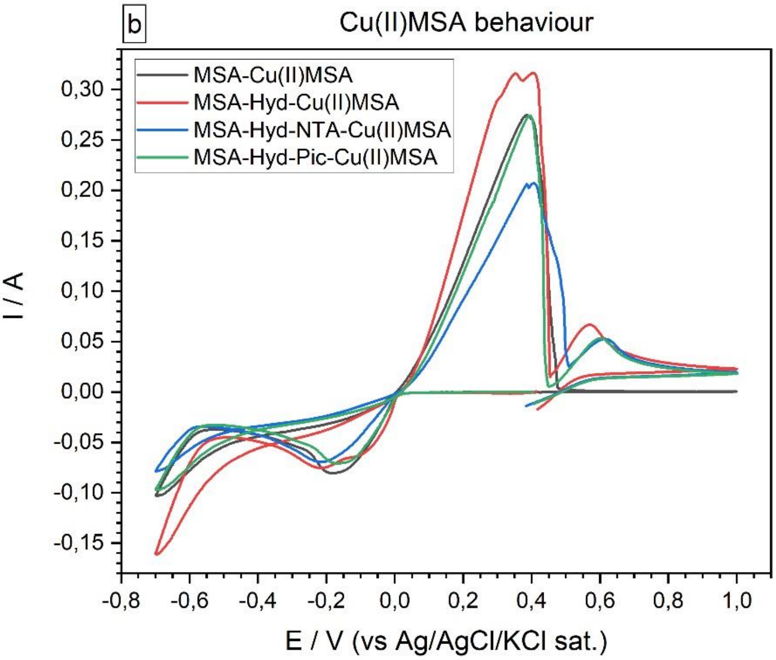
b
Cu(II)MSA behaviour
MSA-Cu(II)MSA
MSA-Hyd-Cu(II)MSA
MSA-Hyd-NTA-Cu(II)MSA
MSA-Hyd-Pic-Cu(II)MSA
I / A
0,30
0,25
0,20
0,15
0,10
0,05
0,00
-0,05
-0,10
-0,15
-0,8
-0,6
-0,4
-0,2
0,0
0,2
0,4
0,6
0,8
1,0
E / V (vs Ag/AgCl/KCl sat.)

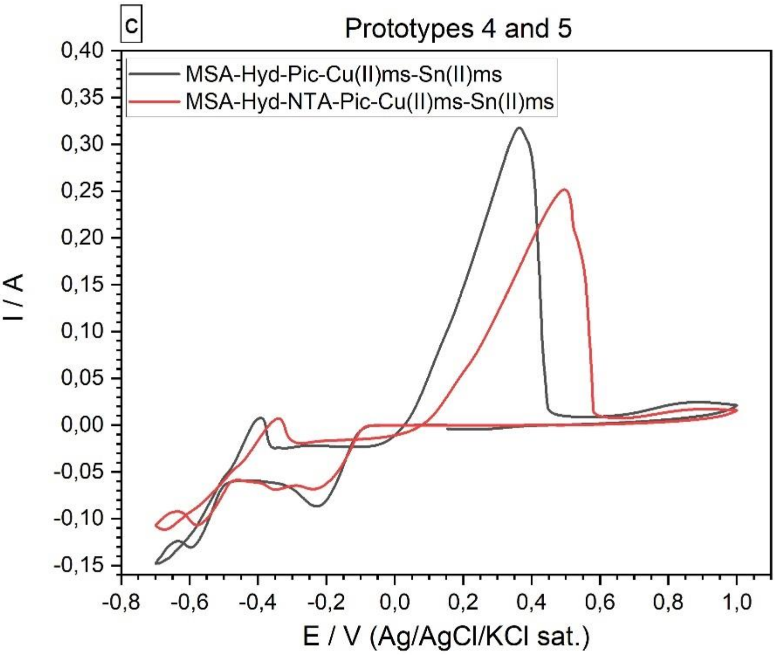

Figure 1.7 - Cyclic voltammetry comparison (50 mV/sec) of single metal precursor formulations (a and b) vs prototypes # 4 and # 5 (c).

Fig. 1.7 reports the comparison between the new single metal precursor formulations labelled as Fig. 1.7.a and 1.7.b and the alternative Cu and Sn precursors formulations (Fig. 1.7.c) corresponding to prototypes # 4 and # 5. In the voltammograms in Fig. 1.7.c the presence of two metallic ionic species in solution with different standard reduction potentials caused for the less noble element (tin) a reduced area signal respect to the same cathodic signal in Fig. 1.7.a (in Fig. 1.7.c $V_{p,c}$, red = -0.56 V or $V_{p,c,}$ black = -0,6 V) due to the limiting current of the more noble metal (copper), whose reduction peaks in Fig. 1.7.c are $V_{p,c,}$ red = -0.36 V and -0.24 V or $V_{p,c,}$ black = -0.22 V. Comparing the CVs in Figs. 1.7.a and 1.7.b (i.e. the single metal formulations) to the CV in Fig. 1.7.c (i.e. alloy deposition formulations) the onset potential of copper reduction was negatively shifted by 0.1 V in both the bath prototypes.

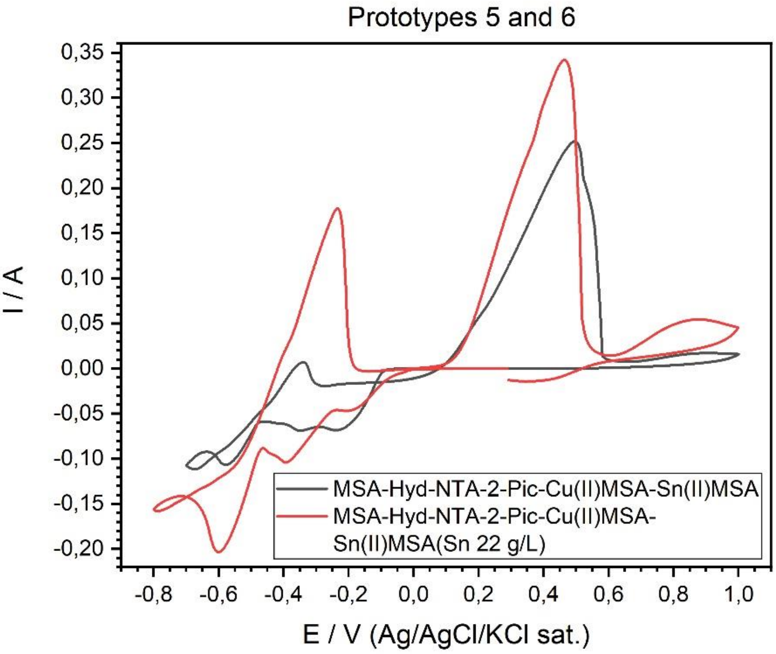

Figure 1.8 - Cyclic voltammetry (50 mV/sec) of prototype # 5 compared with prototype # 6.

The location of the reduction peaks suggested that Cu and Sn were stabilized by each other, but this stabilization didn't derive from the mechanism of the anomalous co-deposition as in the case of Fe-Ni or Zn-Ni alloys [53], because in this case the nobler element is always present in greater quantity in the films deposited.

The characteristic effect of the cooperation of 2-Pic and NTA was the evident differentiation in the Cu^{2+} reduction mechanism, as already observed in Figures 1.4 and 1.6.c. The last prototype (# 6) had the same composition of prototype #4 but with a doubled concentration of Sn(II)MSA, in order to obtain a 1:1 copper:tin molar ratio in the electrodeposited film, necessary in the attempt to synthesize Cu_2ZnSnS_4.

CV data of bath #6 are compared to bath #5 in Fig. 1.8; doubling the concentration of tin precursor caused an increase of its cathodic and anodic peak area (red line, anodic peak current at -0.26 V and cathodic peak current at -0.57 V). Moreover, the resulting CV showed a variation in the cathodic Cu^+ traces: the reaction $Cu^+ \rightarrow Cu^0$ (peak current at -0.38 V) was significantly increased with respect to the same peak obtained from the solution with a Cu:Sn precursor molar ratio equal to 1:0.5 (black line).

Overall, the various additives introduced in the electrolyte did not significantly change the equilibrium potential of both Sn and Cu, suggesting that limited complexation occurs at pH below 1. However, NTA and 2-Pic was found to slow down the kinetics of Cu, while the Sn deposition rate was almost unaffected. Tentatively, was hypothesized that the local pH increase due to hydrogen evolution enabled NTA and 2-Pic to dissociate and complex with Cu, thus slowing the kinetics of Cu reduction.

1.2.2.2 Thermodynamics and crystal structure of electrodeposited films

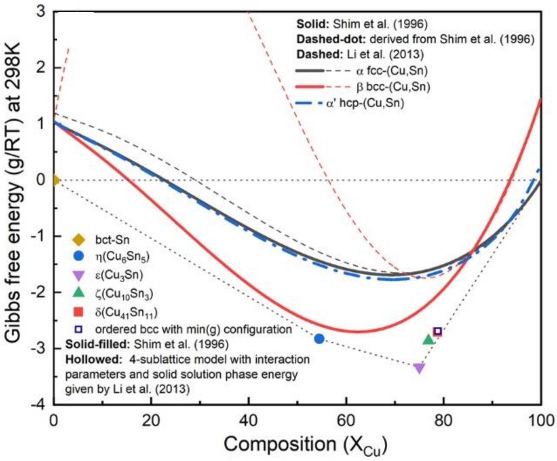

Figure 1.9 - Free energy (G/RT) vs. X_{Cu} curve for the Cu-Sn binary system at T=298K, extracted from various CALPHAD works [42,43].

Due to the importance of Cu-Sn interfacial reactions in soldering processes, the phase diagram of Cu-Sn alloys was studied extensively. Low-temperature annealing of the Cu-Sn diffusion couple yields the phases of ε(Cu_3Sn) and η'(Cu_6Sn_5). Moreover, even at room temperature, other intermetallic phases more stable than the disordered α(fcc) phase can be formed, showing a strong affinity between Cu and Sn and their strong tendency for ordering. At high temperature around 15%$_{Sn, at}$, the bcc solid solution phase *β* is more stable than the fcc solid solution phase *a*, suggesting the possibility of a stable bcc phase owed to the presence of Sn. Modelling of the binary Cu-Sn system was investigated since 1996 [54–59]; different models revealed varying stability of *β*(bcc) at low temperature in the Sn-rich region, as shown in Figure 1.9. The models considered suggested that metastable δ and ζ phases are very close to the stability line ε - α, indicating their small degree of metastability.

Crystal structure of the phases present in the experimental Cu-Sn phase [42,43] (including the α'(hcp) phase in electrodeposited Cu-Sn) [3,4,10,60] are summarized in Table 1.3. The calculated XRD profiles of these phases had similar, strong reflections, making it difficult to identify such phases. Was hypothesize that these intermetallic phases were somehow related to each other, therefore was used the software CrystalDiffract [44] to fit the patterns to face-centered and body-centered structures by continuously varying their lattice parameters. Through this process, were categorized the intermetallic phases as different parent phases and fitted their corresponding parent-phase lattice parameter, which is listed in columns 7-9 of Table 1.3. For some phases, however, the choice for the bcc lattice was not unique; for example, each set of Miller indices $\{\bar{2}21, 11\bar{3}, 311\}$ and $\{22\bar{1}, \bar{1}13, \bar{3}1\bar{1}\}$ may represent the (001) planes of the bcc structure but could also be related by 2-fold rotation along (010) of η'. Therefore, was assumed that these bcc units were related to symmetry operations for the crystal through either 2-fold or 3-fold rotational axes as listed in Table 1.3, which was visualized by reducing the symmetry of the crystal to P1 (consisting only of translations) before calculating their XRD profile in CrystalDiffract, such that the original degenerate planes with respect to the rotation axes could be reduced and all possible combination of the planes could be shown.

Phase	**Stoichiometry**	**Space group**	**ICSD collection code**	**Range of composition from phase diagram $\%_{at,Sn}$**	**Stability WRT 298K**	**Parent phase**	**Fitted lattice parameter WRT parent phase**	**Orientation relationship WRT parent phase**
$\boldsymbol{\alpha}$	(Cu,Sn)	$Fm\bar{3}m$	43493	$0\sim9$	Stable	fcc	a=3.616 Å	
$\boldsymbol{\alpha'}$	(Cu,Sn)	$P6_3$ $/mmc$	N/A	N/A	Not in Phase diagram	hcp	a≈2.7 Å, c≈4.3 Å Based on the reference [41-43]	
$\boldsymbol{Sn}$	Sn	$I41$ $/amd$	106072	100	Stable	Compressed diamond cubic	a=5.831 Å c=3.181 Å	
$\boldsymbol{\beta}$	(Cu,Sn)	$Im\bar{3}m$	103107	$12\sim17$	Unstable $<586\ °C$	bcc	a=3.026 Å	
$\boldsymbol{\eta'}$	Cu_6Sn_5	$C2/c$	106530	$44\sim46$	Stable	bcc	a=2.970 Å	bcc-$0\ 0\ 1 \rightarrow \bar{2}\ 2\ 1, 1\ 1\ \bar{3}$, $3\ 1\ 1$ and their symmetric equivalent planes set WRT 2-axes along $\vec{b}$
$\boldsymbol{\eta}$	Cu_6Sn_5	$P6_3$ $/mmc$	56282	$43\sim46$	Unstable $<189\ °C$	bcc	a=2.943 Å Symmetry of bcc-$0\ 1\ 1$ plane broken into two set of peaks	bcc-$0\ 0\ 1 \rightarrow 0\ 1\ 1, 1\ 0\ \bar{1}$, $1\ \bar{1}\ 1$ and their symmetric equivalent planes set WRT $\bar{6}$-axes along $\vec{c}$.
$\boldsymbol{\gamma}$	Cu_3Sn	$Fm\bar{3}m$	185003	$16\sim28$	Unstable $<520\ °C$	bcc	a=3.108 Å	bcc-$0\ 0\ 1 \rightarrow 0\ 0\ 2$
$\boldsymbol{\delta}$	$Cu_{41}Sn_{11}$	$F\bar{4}3m$	439	21	Unstable $<350\ °C$	bcc	a=2.994 Å;	bcc-$0\ 0\ 1 \rightarrow 0\ 0\ 6$;
$\boldsymbol{\zeta}$	$Cu_{10}Sn_3$	$P6_3$	1847	$21\sim22$	Unstable $<582\ °C$	Unknown. With bcc characteristic peaks	a_{bcc}=3.004 Å	bcc-$0\ 0\ 1 \rightarrow 1\ 1\ \frac{3}{2}, 1\ \bar{2}\ \frac{3}{2}, \bar{2}\ 1\ \frac{3}{2}$ and their symmetric equivalent planes set WRT 3-axes along $\vec{c}$.
$\boldsymbol{\varepsilon}$	Cu_3Sn	$Cmcm$	103102	$24\sim25$	Stable	hcp	a=2.7523 Å, c=4.3453 Å	hcp-$0\ 1\ 0 \rightarrow 1\ 5\ 0, 1\ \bar{5}\ 0$, $0\ 1\ 0$ hcp-$0\ 0\ 1 \rightarrow 0\ 0\ 1$

Table 1.3 - Crystal structure and relations of Cu-Sn phases appearing in the phase diagram (with one additional α'(hcp) phase came from Cu-Sn electrodeposition papers).

The trend of phase stability in electrodeposited Cu-Sn alloy with respect to their elemental compositions has been discussed in several works [3,4,10,60–62]: in 2005, Cavallotti et al. summarized the phase diagram of electrodeposited Cu-Sn, as follows: $\alpha[100,89]\%_{Cu,at} \rightarrow \alpha'[88,82]\ \%_{Cu,at} \rightarrow \beta\ [82,75]\%_{Cu,at} \rightarrow \eta'$, and possibly $\zeta[80,75]\%_{Cu,at}$ [61–63]. Using a rotating disk electrode at brass or Cu substrate, Juškėnas et al. (2006) [60] and Survila et al. (2010) [3] observed the trend of phase formation from sulphate Cu-Sn deposition bath with $\alpha'[95,84]\%_{Cu,at} \rightarrow \beta[86,84]\%_{Cu,at} \rightarrow \delta\ [84,82]\%_{Cu,at} \rightarrow$ Sn. Beattie and Dahn (2013) [62] used pulsed deposition from a pyrophosphate bath in a Hull cell with Ni substrate and observed the following trend for elemental and phase composition: $\delta[80,65]\ \%_{Cu,at} \rightarrow \eta'\ [67,50]\%_{Cu,at} \rightarrow$ Sn$[62,50]\%_{Cu,at}$. Barbano et al. [4] and Bengoa et al. [10] suggested that the ε phase may also contribute to the hcp diffraction peaks in the XRD profile, with the film composition around $80\%_{Cu,at}$ and $85\%_{Cu,at}$, respectively. However, the superlattice peaks of ε at low angles were not observed in their papers, perhaps due to low crystallinity of the hcp-derived phase.

1.2.2.3 XRD and SEM-EDS characterization of Cu-Sn alloys

The films were grown either under 5 different deposition potentials, denoted as "P" for potentiostatic deposition, varying in the range [-0.65, -0.25] $V_{Ag/AgCl}$, or under current control with the same current as the steady-state current in the potentiostatic deposition, denoted as "G" for galvanostatic deposition. The film elemental composition was investigated using SEM-EDS, and the phase composition was characterized by XRD.

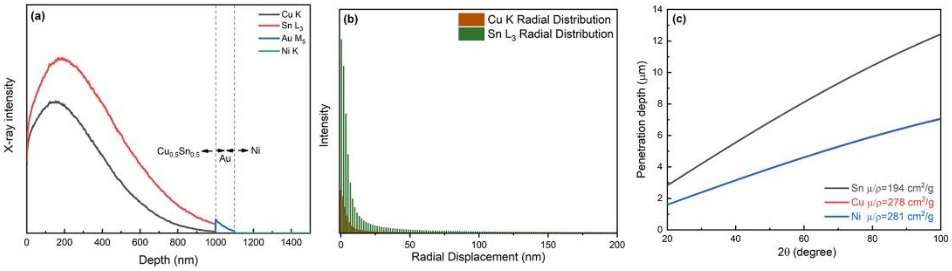

Figure 1.10 - (a) MC simulation (Casino v2.48, 50,000 electrons, 20keV) of the emission intensity of characteristic X-rays for Cu, Sn, Au, and Ni at different depths of the film; (b) radial distribution of the CuK and SnL3 characteristic X-ray intensity; (c) calculated X-ray penetration depth (>1% incident beam intensity) along the normal of the sample for the Bragg-Brentano θ-2θ diffraction geometry with incident X-ray energy (9 keV) slightly higher than Cu Kα, based on mass attenuation coefficients from NIST tables [64].

In order to limit peak overlapping at low energy, an acceleration voltage of 20 keV was chosen. To understand where the SEM-EDS signals came from, the intensity of the characteristic X-ray from $Cu_{0.5}Sn_{0.5}$ was simulated using CASINO v2.48, revealing that 20 keV electrons could sample an EDS depth of ~250 nm and sampling radius ~50 nm for both Cu and Sn, as presented in Figure 1.10.a,b and Figure 1.1. To evaluate the influence of the brass substrate, the X-ray sampling depth with Bragg-Brentano θ-2θ optics was calculated (Figure 1.10.c). Based on Lambert-Beer's law with the X-ray mass attenuation coefficients for Cu, Ni and Sn from the NIST tables [64], the signal probed the entire Cu-Sn deposit and part of the Ni substrate, and in some cases the brass substrate.

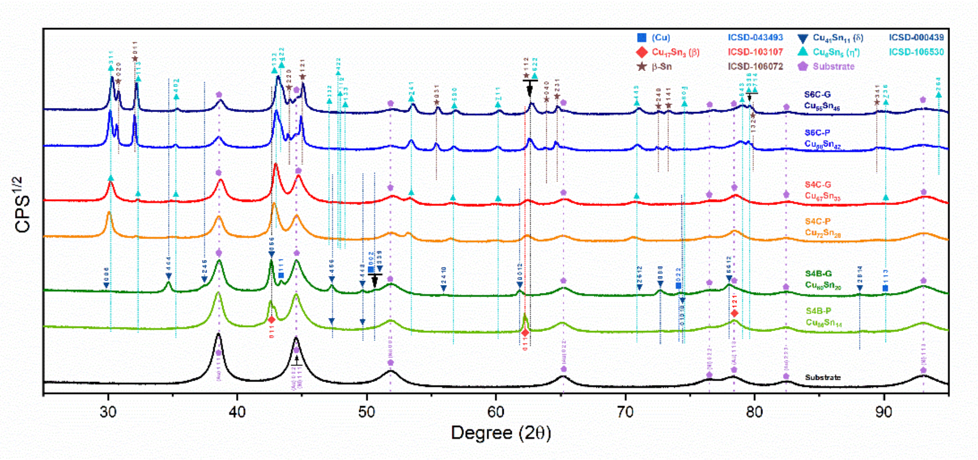

Figure 1.11 - XRD profiles profile for the films S6C-G, S6C-P, S4C-G, S4C-P, S4B-G and S4B-P.

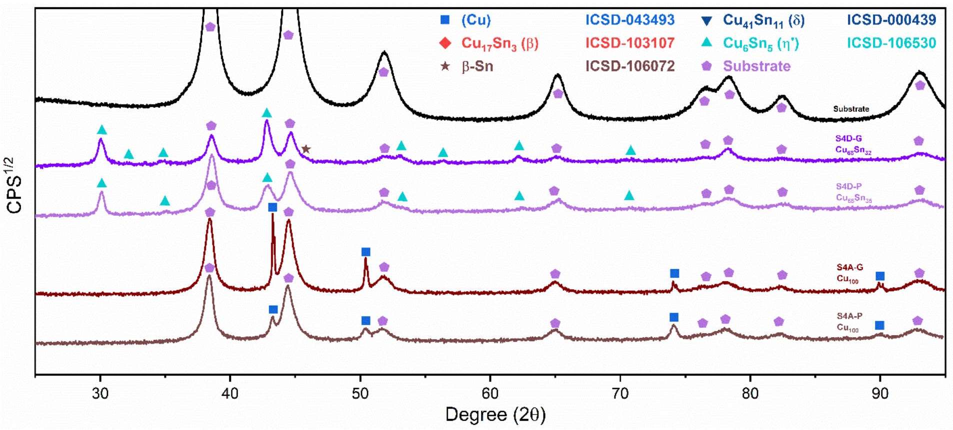

Figure 1.12 - XRD profile for the films S4A-P, S4A-G, S4D-P, and S4D-G.

The XRD profiles of the Cu-Sn films are shown in Figure 1.11 and Figure 1.12. The ε-Cu_3Sn phase was not present in any of the samples. As discussed above, because of their similarity in the crystal structure, the characteristic peaks of different Cu-Sn phases were difficult to distinguish (β, γ, δ), except for the phases with superlattice diffraction of the (3 1 1) plane for η'(Cu_6Sn_5) or (0 1 1) plane for η(Cu_6Sn_5) at 2θ ≈ 30°, the structures of which are shown in Figure 1.13. Considering the possibility of preferred orientation formation for the intermetallic phases, and the large tolerance for their composition variance [65,66], the phase constitution analysis was not definitive. Considering the EDS analysis, the phase composition of each film was proposed and summarized in Table 1.4. From the XRD results (Figure 1.12) within the samples S4D-P and S4D-G, which were deposited below the reduction peak at -0.60 $V_{Ag/AgCl}$, limited β-Sn phase was observed, suggesting that the nucleation of β-Sn phase was inhibited by the competition for Sn by the η' the and δ phases [67].

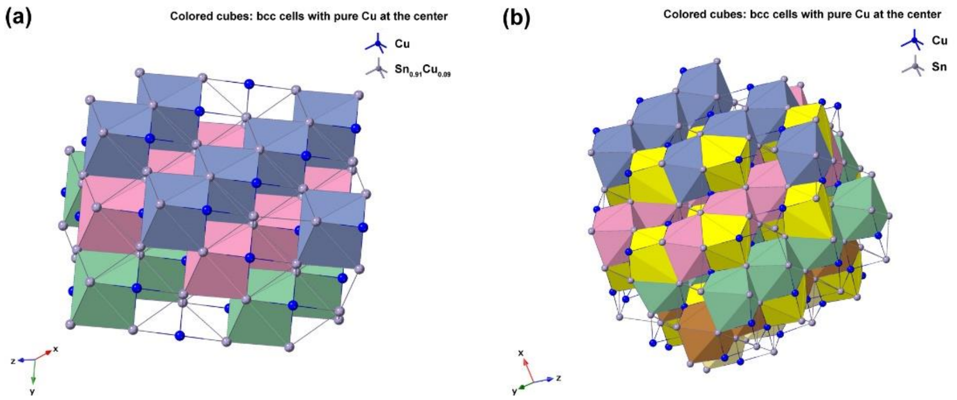

Figure 1.13 - Crystal structures of (a) η (ICSD-52682) and (b) η' (ICSD-106530) phases. Note that the bcc-units with a Cu atom at the center are portraited as solid cubes. Different colors indicate different layers of bcc-001 planes, while additional bcc sites of the low temperature η' phase at each layer is colored specifically in yellow. The vacancies at the body centres break the original symmetry and give rise to bcc-001 diffraction [67]. Considering the large percentage volume difference of Cu and Sn, Ω_{sf} = +83.4% [68], vacancies might be generated by the compressive stress on Cu and a large variation of the size of bcc units may occur due to ordering originated by dissolved Sn in the β matrix.

Sample	Potential	Plan-view composition	Line-scan steady-state composition	Phases composition
S4A-P	-0.25 $V_{Ag/AgCl}$	$100\%_{Cu,at}$		α
S4A-G	~ -0.25 $V_{Ag/AgCl}$	$100\%_{Cu,at}$		α
S4B-P	-0.40 $V_{Ag/AgCl}$	$86\%_{Cu,at}$	$79\%_{Cu,at}$	$\alpha + \beta + \delta$
S4B-G	~ -0.40 $V_{Ag/AgCl}$	$80\%_{Cu,at}$	$78\%_{Cu,at}$	$\alpha + \delta$
S4C-P	-0.55 $V_{Ag/AgCl}$	$72\%_{Cu,at}$	$65\%_{Cu,at}$	$\eta' + \delta$
S4C-G	~ -0.55 $V_{Ag/AgCl}$	$67\%_{Cu,at}$	$58\%_{Cu,at}$	$\eta' + \delta$
S4D-P	-0.65 $V_{Ag/AgCl}$	$65\%_{Cu,at}$		η'
S4D-G	~ -0.65 $V_{Ag/AgCl}$	$68\%_{Cu,at}$		η'
S6C-P	-0.55 $V_{Ag/AgCl}$	$58\%_{Cu,at}$		$Sn + \eta'$
S6C-G	~ -0.55 $V_{Ag/AgCl}$	$55\%_{Cu,at}$		$Sn + \eta'$

Table 1.4 - Elemental composition and phase composition of the deposits.

Analysis of the deposits listed in Table 1.4 showed that the deposition condition (S4B-P and S4B-G), bath constitution (S6C-P and S4C-P), and applied potential (S4B-P, S4C-P) could drastically influence the phase constitution and composition of the film. All films were compositionally uniform under x20k plane-view observation except for deposition from bath S6, which showed a compositional variance as large as $10\%_{at}$ (Figure 1.14).

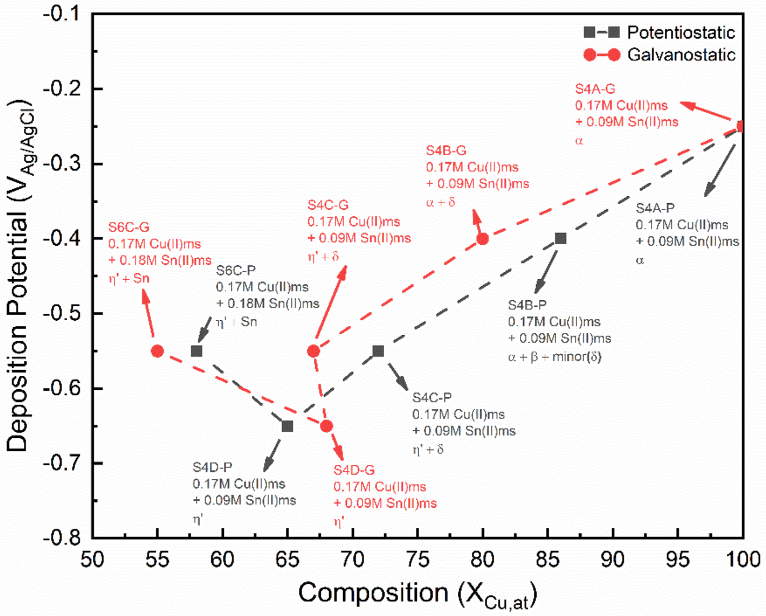

Figure 1.14 - Composition-potential diagram for all the deposited Cu-Sn films.

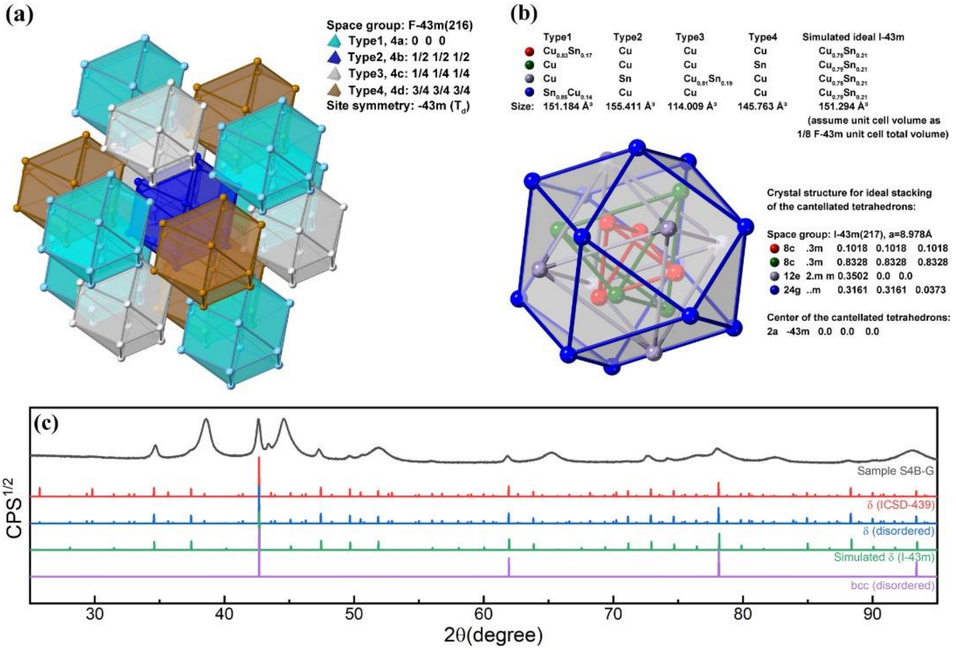

Figure 1.15 - (a) the coordination structure of the cantellated tetrahedrons in δ phase (or cuboctahedron with only Td symmetry); (b) structure of individual cantellated tetrahedrons, with compositions of its four types in Cu41Sn11(ICSD-439) and the simulated fully disordered phase with higher (I-43m) symmetry; and (c) comparison of the XRD profiles between S4B-G, Cu41Sn11 (ICSD-439), simulated fully disordered ICSD-439 structure, and simulated fully disordered I-43m phase.

When comparing the XRD profile of sample S4B-G with the phase $Cu_{41}Sn_{11}$ (ICSD-439), several superlattice peaks at a low angle, especially (333) at 2θ = 26°, were absent or weak. As shown in Figure 1.15.a,b, the crystal structure of $Cu_{41}Sn_{11}$ is the 2x2 "bcc" stacking of 4 types of cantellated tetrahedrons. By setting the occupancy of all sites to the same type of atom in CrystalDiffract, and neglecting the atomic displacement, the simulated XRD pattern of fully disordered $Cu_{41}Sn_{11}$ is shown in Figure 1.15.c. It was noted that the fully disordered $Cu_{41}Sn_{11}$ structure does not show the strong superlattice peak of (333) compared with the original structure. To further determine if the superlattice peak (444) derives from the "bcc" stacking of $Cu_{41}Sn_{11}$, was used the atomic position of a single type of the cantellated tetrahedrons and increased the symmetry to I-43m based on the site symmetry of individual polyhedrons, the crystallography data of which are listed in Figure 1.15.b. It could also be seen that for simulated I-43m stacking, several superlattice peaks around $2\theta = 29°$ were fainter, suggesting that these planar periodicities referred to $Cu_{41}Sn_{11}$ were generated by the size difference between different polyhedron type [68].

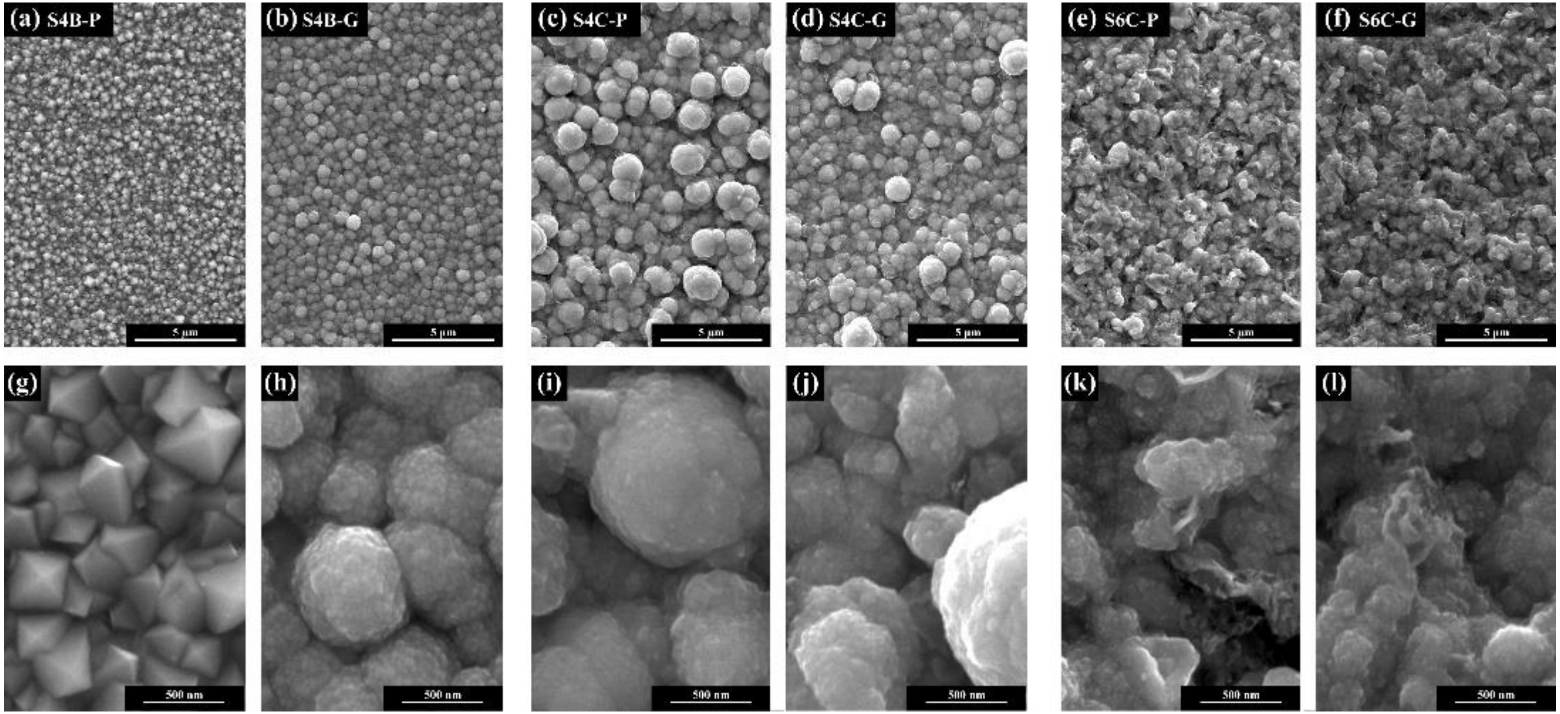

Figure 1.16 - SEM images (top: x5k, bottom: x40k) of (a,g) S4B-P, (b,h) S4B-G, (c,i) S4C-P, (d,j) S4C-G, (e,k) S6C-P, and (f,l) S6C-G.

Figure 1.16 presents the morphology of Cu-Sn films. Deposit S4B-P consisted of highly faceted and apparently large grains with a size about 200 - 300 nm. Considering the XRD data, these large grains should be *β*(bcc) phase. Faceting of bcc sub-μm particles (e.g. Nb [69] and Fe [70–72]) exhibit the shape of rhombic dodecahedra [73,74], as exemplified by the *β*(bcc) phase in S4B-P (Figure 1.16.a,g): the orientation of these pyramids should be (011). A smaller fraction of (001) planes may indicate the slower relative growth rate of (011) planes compared with (001) planes for *β*(bcc) phase. Sample S4B-G in Figure 1.16.b,h, presented quite different features from the potentiostatic counterpart, both in terms of phase constitution and morphology, despite a very close composition. S4B-G mainly consisted of large clusters of size about 500 nm, with each cluster consisting of grains about 10-20 nm. Very few reports discuss that electrodeposition mode (Potentiostatic or Galvanostatic) could influence the phase composition of the films [75–78]. It is uncertain so far whether differences in the phase constitution are dominated by the nucleation behaviour or by the elemental composition, due to the fluctuation of potential caused by the feedback loop necessary to control the Galvanostatic deposition mode.

The morphology of Cu-Sn alloys deposited at higher overpotential (S4C-P, Figure 1.16.c,i) or higher current (S4C-G, Figure 1.16.d,j) however behave similarly. Both sets showed a rough surface consisting of abnormally large grains with size ~ 1-2 μm on top of the film, and small grains with a diameter of less than 1μm at the bottom. Each grain showed a cauliflower shape, probably originated by agglomeration and growth of individual nuclei at high overpotential [4,79–82]. In contrast, potentiostatically deposited film S4C-P exhibited abnormally large grains at the top of the film compared with its counterpart S4C-G, implying some difference between Galvanostatic and

Potentiostatic electrodeposition, despite both modes were designed to have the same steady-state deposition current [83].

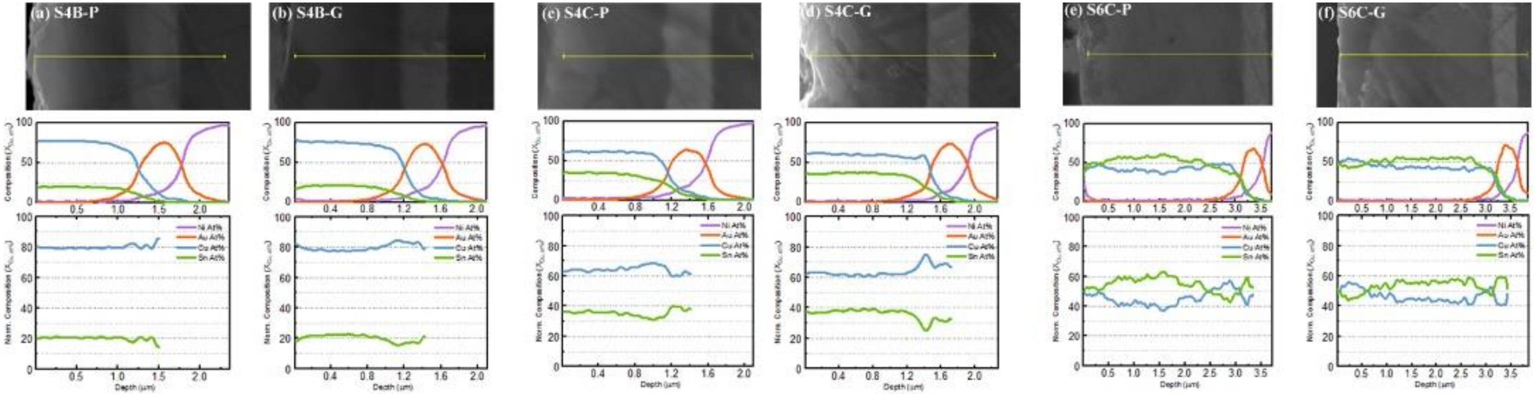

Figure 1.17 - SEM-EDS line-scan of the cross-sections of the sample (a) S4B-P, (b) S4B-G, (c)S4C-P, (d) S4C-G, (e) S6C-P and (f) S6C-G. Raw data was smoothed using Fourier filter in OriginPro 2018 with a low-pass cutoff frequency corresponding to the wavelength ~90 nm [83].

Deposits from bath #6 showed small differences between Potentiostatically (S6C-P, Figure 1.16.e,k) and Galvanostatically (S6C-P, Figure 1.16.f,l) deposited films at the same steady-state current as they exhibited similar morphology. Both samples contained ribbon-like grains and spherical grains, which are likely to be β-Sn [84] and Cu-rich phases, respectively. However, the SEM-EDS data revealed that the correlation between these structures with the elemental distribution is not clear-cut, probably caused by the large sampling volume (depth ~300 nm) of the EDS measurement with an acceleration voltage of 20 keV.

In order to determine the compositional distribution along with the thickness of the film, the sample was cut, ground and polished along its cross-section surface. The thickness of the deposit from bath #4 was around 1 – 1.5 μm, while the thickness of deposits from bath # 6 was around 3 μm. SEM-EDS line-scans of the films were performed with an acceleration voltage of 20 KeV, as shown in Figure 1.17. Using the signal from the Au layer as the reference, the Au peak in the line scan was broadened and slightly shifted, which was attributed to the spatial resolution of the e-beam interaction volume (Figure 1.1) and the drift of the sample. For samples S4C and S6C, the initial growth stage terminated within the first 0.5 μm, and proved to be Cu-rich, suggesting a significant difference between the charge-transfer kinetics for Cu(II) vs. Sn(II). The steady-state composition through the top 0.5 μm of the films is listed in Table 1.4, except for samples from S6C, due to its significant inhomogeneity. The samples S4C and S6C were rich in Cu compared with the steady-state compositions, probably caused by the SEM-EDS sampling of the initial Cu-rich stage (Figure 1.19.a). Considering this effect, a film composition close to Cu:Sn=2:1 was achieved at the steady-state in samples S4C-P and

S4C-G. For S4D samples, despite that the composition was close to 2:1, the films were rough even under visual inspection and thus was not considered to be good films.

However, when more Sn(II) was added to the bath, at the same deposition potential, significant compositional inhomogeneity could be observed in both plan-view SEM-EDS mapping (Figure 1.18) and line-scan perpendicular to (Figure 1.17.d,e) or along the films (Figure 1.19) for the S6C-P and S6C-G samples. Along the film, large variations of the composition could be observed, with the scale from 200-700 nm at the top of the film, to 1.5μm at the bottom of the film with small fluctuations around 200 nm. The average composition was about $50\%_{Cu,\ at}$ at the top of both films, with a composition fluctuation of about 10-20%. An initial Cu-rich region could be observed for both samples at the bottom of the films.

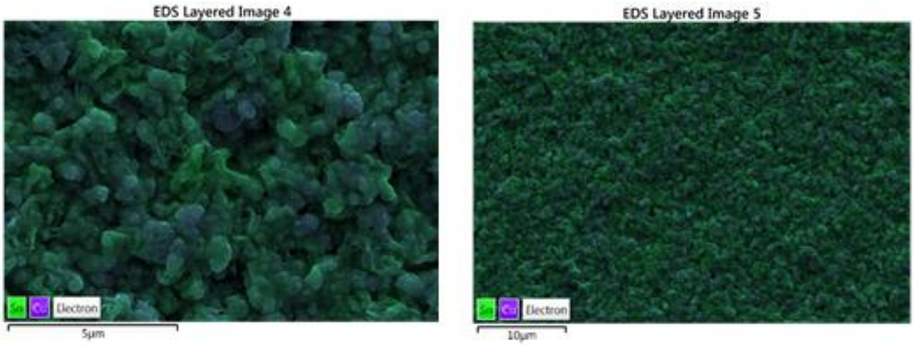

Figure 1.18 - Segregation of Sn and Cu in sample (a) S6C-P and (b) S6C-G by SEM-EDS mapping.

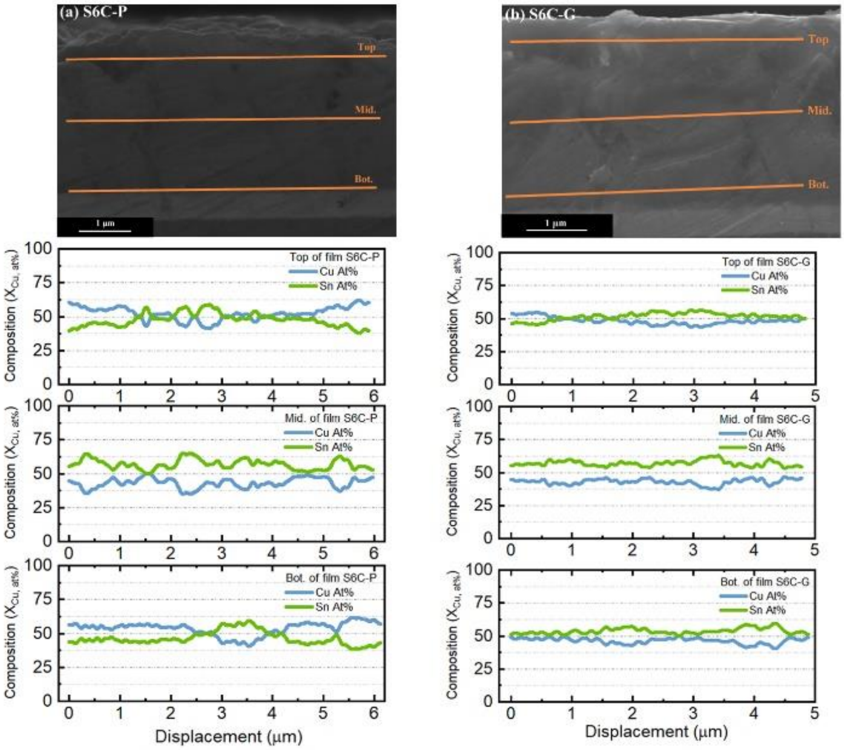

Figure 1.19 - Inhomogeneity of samples (a) S6C-P and (b) S6C-G.

1.2.3 Discussion

As seen in Figure 1.17, due to the high Cu overpotential and transient Cu concentration at the surface, a Cu-rich layer initially grew quickly, until reaching a film thickness of around 0.5 um under the deposition conditions of samples S4C and S6C. This compositional gradient was generated by the depletion of the surface metal ions, after which a steady-state would be reached, resulting in a relatively steady film composition along the film. The initial layer thickness is unavoidable when conventional electrodeposition is used; however, this could be minimized by using a low concentration bath or using for instance pulse electrodeposition.

Sn deposition started to occur at -0.40 $V_{Ag/AgCl}$ based on the CV scans. In presence of Cu ions, however, ~ 20% of Sn in the samples S4B grew *via* underpotential condition due to the enthalpic contribution of the Cu-Sn intermetallic phases compared with β-Sn and fcc-Cu reference phases. From CALPHAD data in Figure 1.15.b, formation of metastable disordered bcc or bcc-derived phases instead of hcp-derived phase ε(Cu_3Sn) could be possibly caused by the favoured energetics or nucleation kinetics of precursor disordered bcc phase vs. disordered fcc or hcp phases.

At high overpotential, the film composition was close to the metal ion ratio in solution; this suggested that during 4 min of deposition from the bath #4 the system was able to reach the limiting current deposition composition, with a mass-transfer coefficient ratio close to 1.

A large composition fluctuation was observed in the S6C depositions, supporting the XRD results that these films consisted of two-phase mixture of Sn-rich and Cu-rich phases; this is reasonable, considering the high Sn content in the deposition bath and the large Sn overpotential, enabling Sn to nucleate, grow independently, and competing with the Cu-rich phases η' or η.

1.2.4 Final remarks and outlooks

In conclusion, it was demonstrated that it is possible to produce a cyanide-free electrodeposition bath for white bronze alloys, based on alternative organic additives and an eco-friendly electrolyte.

It was found that Nitrilotriacetic Acid, a commonly water-insoluble component, is solubilized in presence of Hydroquinone, and it was found that despite the low value of the solution pH, the complexing agents were able to bond metal ions showing a suppressing behaviour for copper. In addition, two stable deposition solutions were identified with Cu:Sn molar ratio in solution respectively of 1:1 and 1:2.

Using the solution with a Cu:Sn molar ratio of 1:1 and a deposition potential of -0.55 V, EDS and XRD data confirmed the formation of a η' single-phase bronze with a Cu:Sn composition ≈ 2:1. Moreover, the SEM cross-section analyses showed a relatively uniform composition of this film. The elemental composition and the crystal structure of the films with deposition condition of S4B made this electrodeposition approach a promising candidate for the synthesis of kesterite compounds.

From the industrial research and development point of view the next step in the study of the formulations developed during this part of the work will be the scale-up of the electrodeposition process in pilot plant, in order to study the aging of the bath more in deeply and to analyse the loss of formulation components during a real working cycle (e.g., consumption during electrodeposition + drag-out).

Future developments and implementations will regard the addition zinc precursor to study the deposition of the ternary alloy Cu-Zn-Sn. Moreover, the development of a sulfurization process by thermal annealing is the mandatory path to synthetize kesterite films.

2 New aspects of copper plating

2.1 Introduction

Copper is an excellent undercoat for subsequent deposits, since it has good capability to compensate substrate defects that could accelerate corrosion and its deposition can be chemically tailored to obtain levelled, high thickness bright films [85]. Of the plating systems that have been studied, only relatively few have revealed a stage of commercial importance for electrodeposition of copper, other types of solutions have been too unstable or lacking in good deposit characteristics over sufficiently wide current density ranges. In first instance, a simple classification can be made based upon the complexing system used: alkaline (cyanide-based and pyrophosphate) and acid (sulfate and fluoroborate) baths.

Alkaline copper solutions have higher microthrowing power (microthrowing power is the ability of a bath to plate into small surface scratches, thereby filling them up with the deposit) compared to acid copper solutions. A solution with good microthrowing power is able to level out surface imperfections and provide a smoother surface)

This type of copper baths has generally lower efficiency than acid solutions because of a low metal concentration and high amount of cyanide in solution (except for high-efficiency alkaline copper baths, used preferentially in the automotive sector, where copper concentration in solution is comparable with that of acid copper baths). These chemical characteristics avoid the formation of a non-adhering immersion layer of copper at the beginning of the plating process, and they guarantee excellent covering.

The principal disadvantage of alkaline copper baths is represented by cyanide handling during the electroplating procedures and the waste treatment of the exhausted bath which has environmental and workers' health concerns.

Most common acid copper baths formulations contain sulfate or fluoroborate salts as copper precursors, organic additives and sulfuric or fluoroboric acid depending on the copper salt. They cannot be plated directly onto active metals, such as zinc or steel, as they will produce non-adhering immersion deposits. Additives and basic ingredients of acidic copper plating fall into one of the following categories.

Copper salts provides the source of copper ions. The acid electrolyte gives conductivity and induces soluble anode corrosion. Chloride is synergistic with organic additives in the brightening and leveling. The brightener, or accelerator, typically contains low molecular weight sulphur and a second atom of high polarity and/or ionic character. Its function is to refine the grain structure in normal copper electrodeposition. Typical brighteners include thiourea, disulfides, thiocarbamates, and thiocarboxylic acid amides. Inhibitors convert an unevenly distributed stationary cathode diffusion layer into a more evenly distributed layer and reduce the variation in copper deposit thickness across the surface. Examples include high-molecular-weight polyether compounds, surfactants, and polyoxyalkylene glycols. The polar leveler slows down the charge transfer of copper ions to copper metal, thus slowing the plating rate in those areas considered high current density.

Acid copper baths are not expensive compared with alkaline baths. The disadvantage of these baths is their low microthrowing power which makes necessary an inner alkaline copper film and the addition of specific brightening agents to the baths. Their use over alkaline copper films is due to their high efficiency and macrothrowing power (macrothrowing power is the ratio of deposit distribution in relation to the distance from anode to cathode; an electrolyte with 100% throwing power will deposit a uniform thickness regardless of anode to cathode spacing).

This part of the work is focused on the chronoamperometric study of an innovative methanesulfonic acid-based copper bath, ready to be upgraded in the eco-compatible white bronze deposition bath I developed [9]. Indeed, a coating of bronze commonly followed the copper deposition in nickel-free processes, increasing the corrosion resistance of the final product [21].

Chronoamperometric studies allow to obtain information about the mechanism of nucleation and growth of an electrodeposited film. The nucleation is a crucial step during the formation of a metal film and its mechanism plays a key role in the formation of the metal surface morphology and structure [86,87]. Controlling the nucleation and growth mechanism it is possible to obtain a fine control on the morphology of the final deposit otherwise obtainable only with atomic layer deposition techniques [88], which are much more complex to scale up and to manage at industrial level. The Scharifker-Hills model is the electro-crystallization model applied in this work to detect the type of nucleation mechanism. Indeed, in this part of the *Ph.D.* thesis I posed my attention on the attempt to find a correlation between the results obtained from the Sharifker-Hills model and the progressive addition of an organic additive in an alternative copper electrodeposition bath. The correlation between kinetic results and copper film morphology I tried to identify, could allow to analyze the effect of electroplating organic additives prior the trial-and-error study commonly applied during the development of new plating formulations. In this way, I managed to tailor the concentration of the addictive I selected to control copper growth in view of an upgrade of the bronze coatings I obtained.

2.1.1 The Scharifker-Hills model

Chronoamperometric studies allow to obtain information about the mechanism of nucleation and growth of an electrodeposited film. When the formation of metal nuclei takes place during an electrodeposition, three different morphologies (one-dimensional, two-dimensional (2-D), and 3-D as in the case of hemispherical growth) can characterize the formation process of the new surface. From the rate-determining step point of view, two different regimes can be established. A kinetic-controlled regime, where the rate-determining step is the reduction reaction of metal ions in the growth point. A diffusion-controlled regime, where the rate-determining step is the mass transfer of the metal ions through the deposition solution toward the cathode surface. Several models have been developed for describing the nucleation and growth of metal during electrodeposition at constant potential. In the present study the Sharifker-Hills model (S.H.) had been used [89–91]. This model has been developed to study the case of an electro-crystallization reaction with a 3-D nucleation mechanism and a diffusion-controlled growth. In these conditions the nucleation is a crucial step during the formation of a metal film and its mechanism play a key role in the formation of the metal surface morphology [86]. The values of current vs time are fitted to a nucleation and growth model which allows obtaining many parameters and information such as type of nucleation (instantaneous or progressive), ions diffusion coefficients, nucleation rate and density of metal nuclei at the electrode surface [92,93].

The initial stages of an electrodeposition process are associated with a three-dimensional multiple nucleation mechanism. Subsequently takes place the growth and coalescence of the nuclei formed on the electrode surface. The growth current of a single hemispherical nucleus depends on the diffusion coefficient, on the concentration of bulk, on the molar charge of the species being deposited and on the molecular weight and density of the deposit [93]. However, in real cases becomes mandatory to consider the interaction, during nucleation and growth, between multiple nuclei that form simultaneously [94]. For a system in which the nucleus growth-phase is determined by diffusion processes (favored by low concentrations and high over-voltages) the overlapping of the diffusion areas around each individual nucleus is described by the Cottrell equation. Ion's diffusion, according to Cottrell, occurs substantially only in a direction perpendicular to the electrode surface (semi-infinite linear diffusion) and the equation applies to stationary flat electrodes and for stationary solutions. Within this picture, the electroplating of a metal is a complex process characterized by several stages: the transport of solvated species from the bulk to the electrode surface, their reduction near the interface between the cathode and the electrolytic solution and finally the formation of nuclei. The growth of the nuclei occurs on the surface of the substrate extending perpendicularly to it and laterally, along the surface, forming three-dimensional deposits [95]. This process is not part of the 2-dimensional process (valid for nucleation in the absence of interactions), which can be treated through Avrami's theorem. According to such approach, each nucleus is in the center of a cylindrical diffusion area. The diffusion cylinder can be projected onto the cathodic surface and takes the name of "planar diffusion zone". The radius of this area is greater than the radius of the nucleus. A planar surface of enough area is thus obtained to achieve the same flow of matter that would be transferred to the accretion center by means of three-dimensional spherical diffusion. Assuming a linear flow, the overlap of the diffusion zones of single adjacent nuclei is reduced to a two-dimensional problem, to which the Avrami's theorem can be applied. As the size of the diffusion areas increases, an overlap condition is reached. At the same time, the supply of material to the growth center is hindered in the directions adjacent to the nucleus. The direction perpendicular to the surface of the substrate becomes the preferential one for mass transfer, thus creating the previously mentioned diffusion cylinder. According to Avrami's theorem, on a real surface the nucleation rate is given by the equation:

$$dN/dt=A(N_0-N) \tag{2.1}$$

where N_0 is the number of active sites per unit area on the cathode surface and A the nucleation rate. The integrated equation, considering $N = 0$ at time $t = 0$, gives rise to the expression that allows to calculate the density of nuclei as a function of time:

$$N(t)=N_0[1-\exp(-At)] \tag{2.2}$$

Based on the considerations made so far, two borderline cases can be obtained [96]:

- instantaneous nucleation, characterized by high nucleation rate ($A \gg 1$) and low numerical density of active sites on the electrode surface; under these conditions the ratio $N_0/A \rightarrow 0$ and the equation become $N(t)=N_0$; the maximum nuclei density is reached immediately after the application of the potential and does not undergo subsequent changes.
- progressive nucleation, which occurs with very low nucleation rates ($A \ll 1$) and in the presence of many active sites available; in this case the ratio $N_0/A \rightarrow \infty$ and the equation becomes $N(t)=N_0 \cdot At$; nuclei are formed at constant speed because under stationary conditions $dN/dt = \text{const.}$ and consequently the density of nuclei increases linearly with time.

In both borderline cases the trend of the current has a maximum and then decays asymptotically by approximating the Cottrell limit current. Knowing the experimental values of current density and time from chronoamperometric measurements a theoretical curve for the two borderline cases can be obtained, using the two fitting equations below.

Progressive nucleation equation:

$$\frac{J^2}{J_m^2} = \frac{1.2254}{\frac{t}{t_m}} \left\{1 - exp\left[-2.3367\left(\frac{t}{t_m}\right)^2\right]\right\}^2 \tag{2.3}$$

Instantaneous nucleation equation:

$$\frac{J^2}{J_m^2} = \frac{1.9542}{\frac{t}{t_m}} \left\{1 - exp\left[-1.2564\left(\frac{t}{t_m}\right)\right]\right\}^2 \tag{2.4}$$

A method to determine the type of nucleation is the comparison of the dimensionless theoretical curves obtained from equations (2.3) and (2.4) with the experimental values obtained, shown in a plot such as:

$$J^2/(J_m^2) \text{ vs } t/t_m \tag{2.5}$$

where with J_m we mean the maximum current density recorded at the minimum time, and with t_m the time at which the maximum current density is recorded. Equations (2.3) and (2.4) are the only ones where is indifferent the use of current density value or current value because $(J/J_m)^2$ and $(I/I_m)^2$ only differs of a constant value (electrode area).

Different kinetic data of nucleation mechanism can be obtained applying the appropriate equation, according with the S.H. model.

For the instantaneous nucleation borderline case can be calculated D, the ions diffusion coefficient (cm^2/s) in solution and N, the metal nuclei surface density (cm^{-2}).

$$k = \left(\frac{8\pi cM}{\rho}\right)^{1/2} \tag{2.6}$$

$$D = \frac{J_m^2 t_m}{0.1629(zFc)^2} \tag{2.7}$$

$$N = \frac{1.2564}{t_m \pi k D} \tag{2.8}$$

For the progressive nucleation borderline case can be calculated D, the ions diffusion coefficient (cm^2/s) in solution, AN_∞, the nucleation rate ($cm^{-2} \cdot s^{-1}$) and N_s, the nuclei density at the surface saturation (cm^{-2}).

$$K' = 4/3(\frac{8\pi cM}{\rho})^{1/2} \tag{2.9}$$

$$D = \frac{J_m^2 t_m}{0.2598(zFc)^2} \tag{2.10}$$

$$AN_\infty = \frac{4.6733}{t_m^2 \pi K' D} \tag{2.11}$$

$$N_s = \left(\frac{AN_\infty}{2K'D}\right)^{1/2} \tag{2.12}$$

Where F is the Faraday constant, z is the number electrons exchanged during copper reduction, ϱ is the density of copper, c is the metal ions concentration in solution, k and K' are calculation constants.

Must be noted that to obtain kinetics data from the equations above the metal precursor concentration must be converted in moles on cm^3 as can be deduct from dimensional analysis.

The application of S.H. model to analyze chronoamperometric data is subordinated to the confirmation of the type of electro-crystallization process

(3-D nucleation with diffusion-controlled growth for S.H.) which can be verified by means of voltametric experiments as already reported in literature [97–99].

The limit of the S.H. model lies in the need to treat the two borderline cases separately and therefore in the inability to derive the descriptive parameters of the reaction in the intermediate cases.

2.2 Effect of thiourea on the nucleation and growth of copper: kinetic data vs film morphology

In this section will be presented the study of an alternative method to state the effect of the addition of an organic additive in an electrodeposition bath. The concept behind this work regards the possibility to understand if an organic additive could have a relevant effect on the morphology of an electrodeposited film (e.g., brightener, leveler, suppressor, etc.) exploiting an “a priori” kinetic study instead of only morphological analysis on the metal coating.

2.2.1 Experimental

The bath studied contained methanesulfonic acid as the electrolyte (4.62 M, MSA), copper(II)-methanesulfonate as copper precursor (0.17 M, abbreviated Cu(II)MSA), nitrilotriacetic acid as copper ions complexing agent (0.1 M, NTA), hydroquinone as NTA dissolving agent (0.09 M, Hyd) and thiourea as the organic additive under study (30-60-90 ppm, TU). Hydroquinone was used as nitrilotriacetic acid (NTA) dissolving agent as already reported in the previous chapter, because the dissolution of NTA in the water/methanesulfonic acid (MSA) system gave an unstable solution due to its poor solubility. Electrochemical measurements and depositions were carried out with a Metrohm (Herisau, Switzerland) Autolab mod. μAutolab type III potentiostat/galvanostat computer-controlled by Nova® 2.1.4 software (Metrohm) using Ag|AgCl (0.197 V vs SHE at 25 °C and KCl saturated) electrode as reference (reference electrode for each potential reported in this chapter, unless different stated). All the potentials recorded in this study were related to this reference electrode. The working electrode was rotating disk (RDE-2) glassy carbon electrode (Metrohm) with a surface area of 0.31 cm^2, RDE-2 by Metrohm. Glassy carbon electrode was cleaned by an electrochemical treatment based on the following steps [100]:

- OCP measurement;
- application of a potential of +1.2 V vs Ag/AgCl/KCl$_{sat}$ for 120 sec.;
- rotation at 2000 rpm;
- during electrode rotation, application of 3 voltammetric cycles in the range [-1/+1.4] V vs Ag/AgCl/KCl$_{sat}$ at 50 mV/sec.

After each electrochemical cleaning the electrode surface was treated with a polishing cloth and alumina water dispersion (0.3 μm diameter particles). The surface cleaning were confirmed by the voltammetric measurement of the reversible couple $[Fe(II)(CN)_6]^{4-}/[Fe(III)(CN)_6]^{3-}$. Each electrochemical measurement and deposition were carried out in a thermostated cell with a set temperature of 25 °C.

The morphology of the electrodeposited films was characterized by scanning electron microscopy (SEM), SEM images were recorded with Hitachi (Tokio, Japan) SU3800 Scanning Electron Microscope using an acceleration voltage of 10 KeV.

Electrodeposition was carried out onto glassy carbon buttons with diameter of 1.5 cm after a previous cleaning procedure. The buttons were cleaned by immersion in aqua regia for 30 seconds and then rinsed with distilled water to ensure the absence of metal residues. Subsequently the GC surface was polished with polycrystalline diamond dispersion (3 μm) followed by distilled water rinsing, acetone rinsing and drying under air flow. The electrical contact for the deposition was made using copper tape, applied in the rear part of the GC button.

X-ray fluorescence spectroscopy of deposited copper on glassy carbon was carried out using a Bowman XRF (Schaumburg, Illinois, USA), previously calibrated with Bowman certified copper standard on bulk carbon [101].

2.2.2 Results

2.2.2.1 Voltammetric studies

According to the literature TU is a well-known organic brightener used in traditional copper electrodeposition baths, modifying the kinetics of copper electrodeposition mechanism. In this case thiourea was added in a copper solution which already contained a complexing agent, necessary to tailor copper electrodeposition potential in the case of an upgrade of the bath into a bronze electrodeposition one. From the standpoint of the mechanism with which thiourea modify the copper film formation in the innovative bath developed during this work, cyclic voltammetry was selected as the election technique to clarify the electrochemical behavior of copper ions in the absence and presence of thiourea. CV was also useful to select the cathodic potentials applied during chronoamperometric measurements. The voltage range used in cyclic voltammetry measurements ([-0.8/+0.5] V) was based on the partial reversibility behavior of the hydroquinone/benzoquinone couple which would bring a degradation of hydroquinone at scanning potentials over +0.5 V. The oxidation could be easily explained by the simple redox reaction as follows:

$$2C_6H_4OH_2 \rightarrow 2C_6H_4O_2 + 4H^+ + 4e^- \quad E^0 = +0.699 \text{ V vs SHE}$$

Moreover, the glassy carbon surface of the electrode would be damaged if the scanning range would overcome +1.5 V in acidic solutions (in this work pH~1) [100,102].

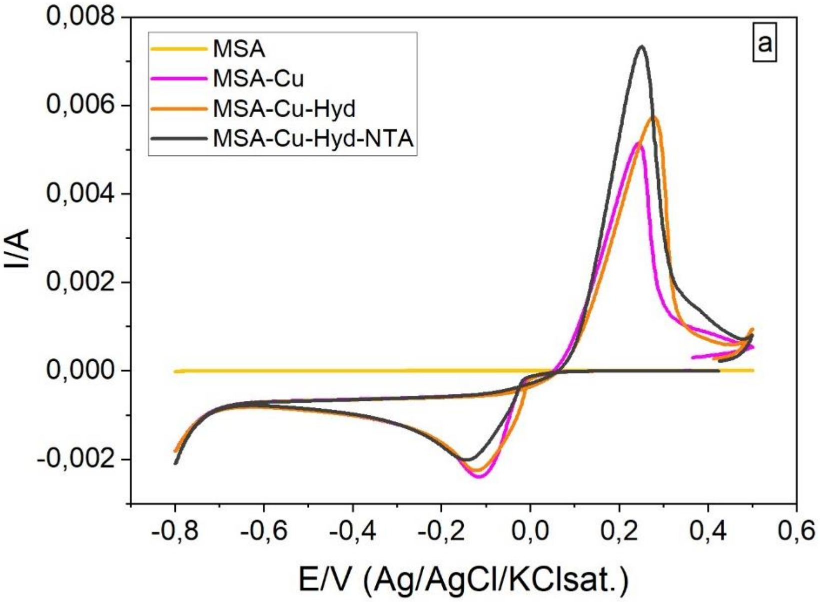

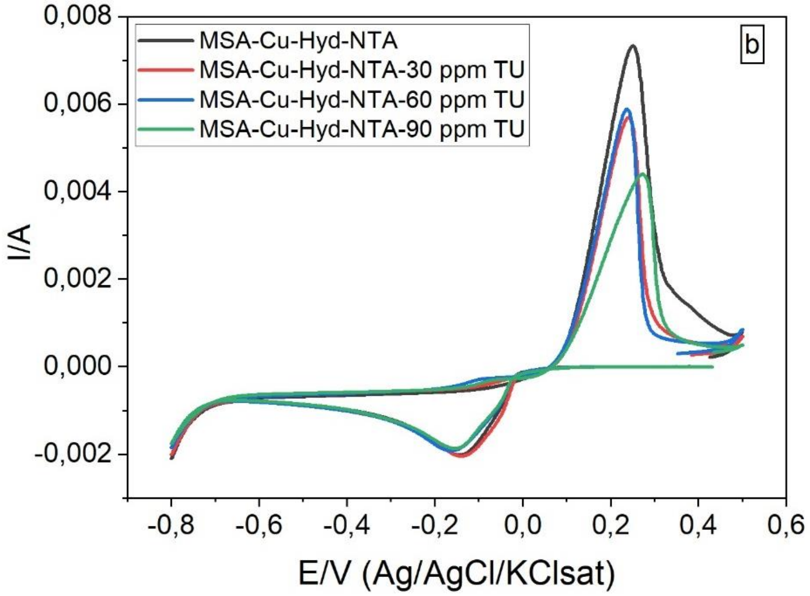

Figure 2.1 - CVs of Cu(II)MSA 0.17 M in MSA 4.6 M aqueous solution. GC-WE, Ag/AgCl/KCl$_{sat}$-RE, Pt-CE, 50 mV·s^{-1} the scan rate. a) addition of Hyd 0.1 M and NTA 0.1 M to the copper solution (as indicated in the plot); b) addition of 30/60/90 ppm of TU to the previous solution (as indicated in the plot).

As already reported in paragraph 1.2.2.1. NTA is a Copper chelating agent, which at acidic pH values forms univalent complexes with Cu^{2+} ions [48,49,103] as proposed by Muralidharan et al.

As can be seen in Fig. 2.1.a, cyclic voltammetry tracks, show the redox behavior of Cu(II) ions in presence of MSA, Hyd and NTA. While Hyd didn't alter appreciably either the redox potentials of the Cu^{2+}/Cu^{0} couple or the CV signals area, NTA shifted the copper reduction to -0.14 V, slightly reduced the cathodic signal area (reduction MSA-Cu=$-2.387 \cdot 10^{-4}$ C, reduction MSA-Cu-Hyd-NTA=$-2.208 \cdot 10^{-4}$ C) and increased the anodic signal area (oxidation MSA-Cu=$4.736 \cdot 10^{-4}$ C, oxidation MSA-Cu-hyd-NTA=$7.150 \cdot 10^{-4}$ C). It was hypothesized the latter effect caused by a partial anodic degradation of NTA as already reported by Wu et al. on a boron-doped diamond anode [104].

After the voltammetric study of the copper electrodeposition solution, increasing concentration of thiourea was added. In this work was tested the effect of 30 ppm ($3{,}94 \cdot 10^{-4}$ M), 60 ppm ($7{,}88 \cdot 10^{-4}$ M) and 90 ppm ($12 \cdot 10^{-4}$ M) of thiourea.

Analyzing the red voltammogram in Fig. 2.1.b, referred to $3.94 \cdot 10^{-4}$ M thiourea in solution, was observed that the copper reduction and oxidation peak potentials remained approximately unchanged in presence of the lowest additive concentration, compared to the dark grey track (absence of TU).

The further additions of thiourea determined some variations in the cyclic voltammetry of the formulation. In the voltammogram relative to the presence of 60 ppm ($7.88 \cdot 10^{-4}$ M and 90 ppm ($12 \cdot 10^{-4}$ M) of TU the cathodic signal of copper was shifted to -0.16 V and there is a progressive reduction of the signal area in both the reduction (reduction TU 60 ppm=$-2.107 \cdot 10^{-4}$ C, reduction TU 90 ppm=$-2.018 \cdot 10^{-4}$ C) and the oxidation peaks (oxidation TU 60 ppm=$5.232 \cdot 10^{-4}$ C, oxidation TU 90 ppm=$4.653 \cdot 10^{-4}$ C). In this case, this feature was tentatively attributed to the capability of thiourea and its byproducts to adsorb both on the bare glassy carbon surface and on the copper-covered electrode surface. As already proposed by Cofré and Bustos thiourea tends to adsorb on GC with an electrode coverage proportional to its amount in solution [105] reducing the electrochemically active area. Moreover, Cu-S affinity [106,107] determines the formation of a polymer-like insoluble film from adsorbed TU-species during the nucleation and growth of the copper film [108,109]. This complex film hinders the electrodeposition and the electro-dissolution of copper and, at sufficiently positive potentials, can be electro-oxidized to produce FDS, S^- and CN-containing species [110] which eventually change the nature of products blocking the copper surface and change the kinetics of the global anodic reaction. The slowing of the copper anodic dissolution kinetics was attributed as the main cause of the reduction of anodic peaks area at the increasing amount of TU in solution. The interaction of thiourea with copper ions in solution to form various complexes, as reported in literature [111,112] was hindered by two factors: the presence of NTA as copper ligand and the high Cu:TU molar ratio (which is respectively 431, 215 and 142 for 30, 60 and 90 ppm TU).

2.2.2.2 Chronoamperometric studies

A chronoamperometric study was carried out at three different deposition potentials for copper, based on the voltammetric measurements (see above). The electro-crystallization of copper from acidic solutions on glassy carbon electrodes evolves through a 3-D nucleation with diffusion-controlled growth [113–115], this type of mechanism allowed to apply the S.H. model to the chronoamperometric data recorded, as reported in Fig. 2.2. In this way was attempted to characterize the nucleation and growth behavior of copper in an alternative deposition bath with selected amounts of thiourea [116] on glassy carbon electrodes. The current values registered by chrono-amperometry was transformed into current density after the measurements. This type of study was already reported in literature using very different deposition conditions and substrates [117,118] from those tested in this case.

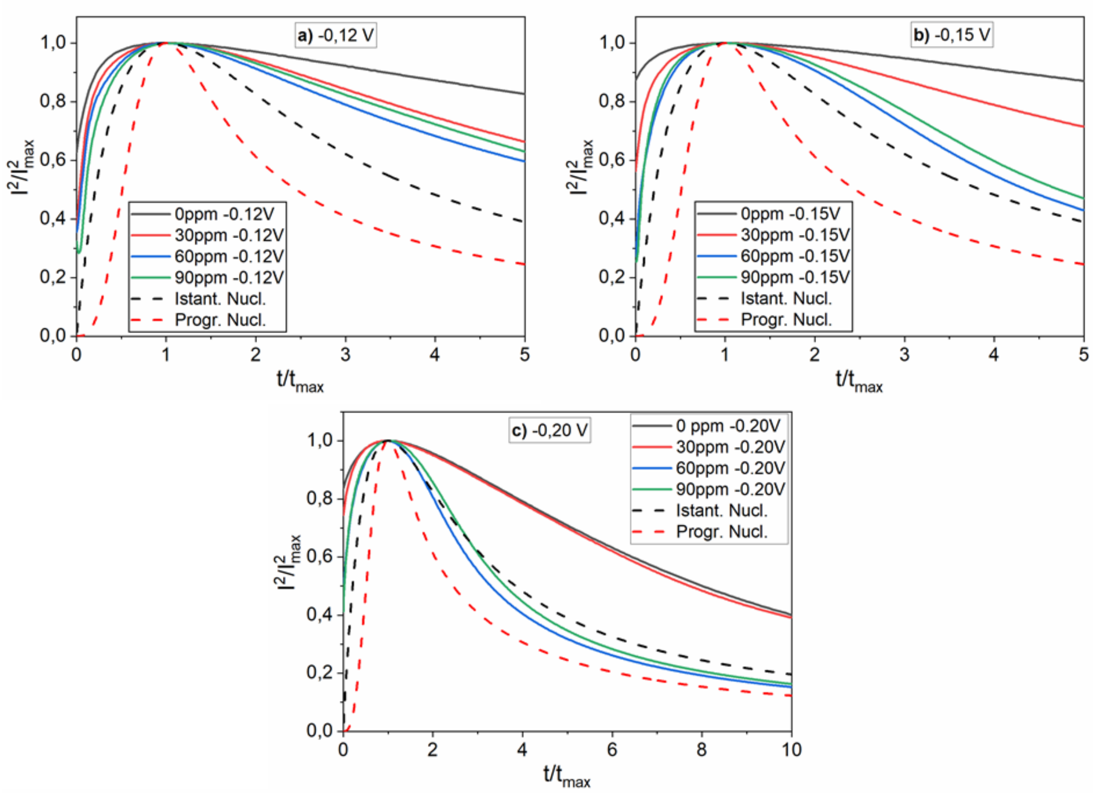

Figure 2.2 - Kinetic analysis. Relevant S.H. plots of one-step current transients recorded at various TU concentration and various potentials (as indicated in the plots a-b-c). In the current transient recording procedure, the initial potential (OCP) is maintained for 10 s, then the potential is stepped at a final.

E (V)	TU (ppm)	t_m (s)	I_m 10^{-3} (A)	J_m 10^{-3} (A/cm^2)	$J_m^2 t_m$ 10^{-5} (A^{2}s/cm^4)	D 10^{-7} (cm^2/s)	N 10^7 (cm^{-2})
-0.12	0	0.180	-2.130	-6.871	0.850	0.485	26.3
	30	0.445	-1.993	-6.429	1.839	1.05	4.92
	60	0.575	-1.809	-5.835	1.958	1.12	3.58
	90	1.105	-1.390	-4.484	2.222	1.27	1.64
-0.15	0	0.095	-2.800	-9.032	0.775	0.442	54.7
	30	0.255	-2.633	-8.494	1.840	1.05	8.59
	60	0.415	-2.840	-9.161	3.483	1.99	2.79
	90	1.021	-1.766	-5.697	3.313	1.89	1.19
-0.20	0	0.08	-4.98	-16.065	2.064	1.177	24.4
	30	0.160	-3.439	-11.094	1.969	1.12	12.78
	60	0.280	-3.937	-12.700	4.516	2.58	3.18
	90	0.370	-3.305	-10.661	4.205	2.40	2.59

Table 2.1 - Kinetic data obtained from S.H. model for the nucleation of copper in presence of different amounts of TU. First column shows the final potential value, in the one-step experiment. Second column shows the amount of TU in the studied solution. Third, fourth and fifth columns show the deposition time of the nucleation peak current, the value of the peak current and the value of the peak current density respectively. The sixth column shows intermediate mathematical operation values necessary to calculate the values of diffusion coefficient of copper ions reported in the seventh column and the nuclei density values at the first stages of nucleation reported in the eight column.

The measures reported in Figure 2.2, allowed to deduce that the nucleation of copper approached the progressive mechanism with increasing concentration of additive and with potentials increasing in absolute value, despite at the concentrations studied, full progression of nucleation was never achieved. Furthermore, the thesis of the inhibition of the copper instantaneous nucleation due to thiourea was supported by the decrease of the nuclei surface density (cm^{-2}), as can be observed from the data in Table 2.1, for each deposition potential set of measurements. The shift towards a progressive nucleation produced a lower number of nuclei at the initial stage of the deposition, compared to an instantaneous nucleation mechanism. The hypothesis on the mechanism of thiourea in the condition studied in this work was reinforced comparing information from cyclic voltammetry and chronoamperometry. The Effect of glassy carbon surface inhibition by thiourea observed at 60 and 90 ppm in the CV, could also be confirmed by chronoamperometric data, in which was observed a hindering of the copper nucleation at the first steps of electrodeposition. At the best of my knowledge, I supposed that the same mechanism of physio-chemical adsorption of TU and related polymer film on glassy carbon already observed during voltametric analysis, caused the reduction of nuclei surface density (cm^{-2}) and the approaching of the progressive nucleation mechanism at increasing TU concentration.

2.2.2.3 Morphological characterization

The electrochemical solutions with 0, 30, 60 and 90 ppm of TU were used to produce copper films using a potentiostatic deposition method with an applied deposition potential of -0.20 V, a deposition time of 600 seconds, a set temperature of 25 °C, in absence of stirring to emulate chronoamperometric tests condition reported above. SEM images and pictures reported in Figure 2.3 allowed to correlate the microstructure of the deposit to the theoretical information obtained by the mathematical model used to analyze chronoamperometric data. The results showed a refinement of the crystallites size up to 60 ppm of thiourea added, while the presence of 90 ppm of TU caused the formation of a copper film with uncontrolled morphology and grain size. As already observed from voltametric analysis the presence of the highest amount of organic additive caused the random formation of an organic film made of adsorbed TU-species both on the glassy carbon surface and on the growing copper nuclei. I hypothesized that this film hindered the formation of copper nuclei on the bare glassy carbon promoting the formation of discontinuities in the copper film as can be observed in Figures 2.3.j and 2.3.k. Moreover, the adsorption of TU-species on the growing copper nuclei caused an undefined growth which cannot be predicted prior the characterization of the film by Scanning Electron Microscopy. From a macroscopic point of view Figures 2.3.c, 2.3.f, 2.3.i and 2.3.l showed the improvement of the aesthetic characteristics of the copper film with the increasing amount of thiourea up to 60 ppm. Adding this concentration of thiourea to the innovative copper bath used in this work the film obtained resulted homogeneous and bright confirming the brightening action of TU and its effect on the nucleation and growth of copper. The concentration of 90 ppm resulted not suitable for the obtainment of a high-quality copper film from the formulation studied.

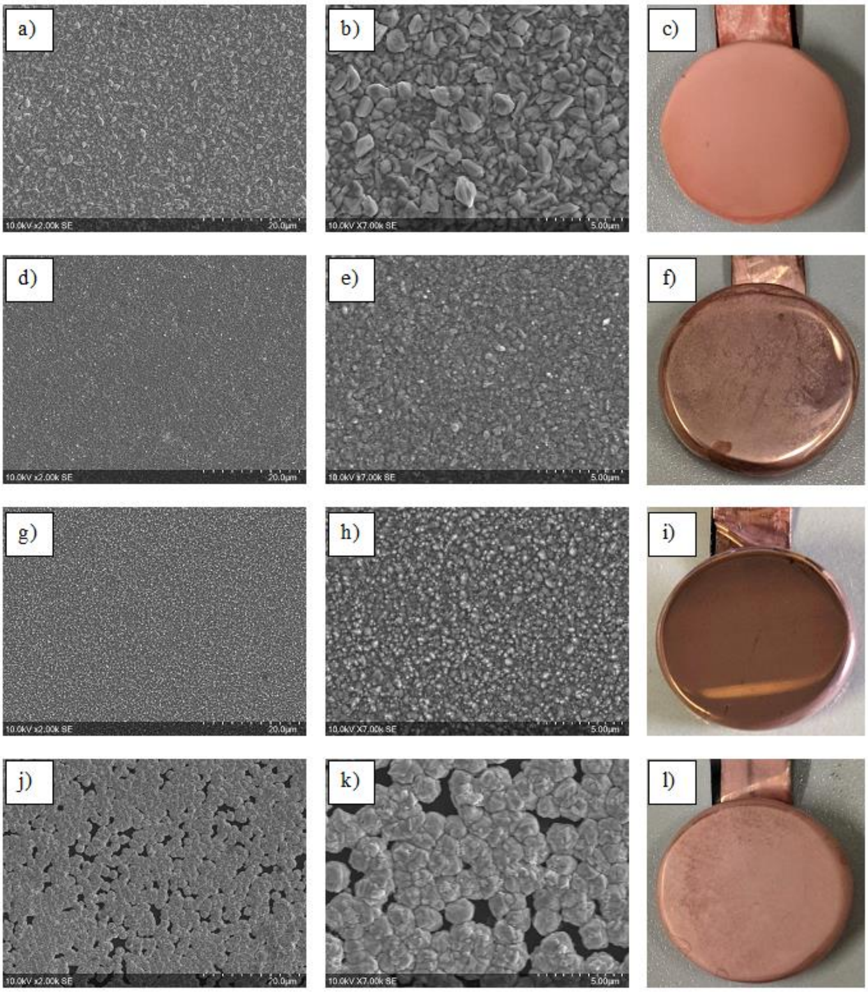

Figure 2.3 - SEM characterization and sample photographs of different copper film deposited onto GC substrates. Electrodeposition parameters: 600 s, -0.20 V, 25°C, no stirring. From left to right of each row SEM micrographs at 2k and 7k enlargements and sample photo. Images a), b) and c) from the copper bath without TU. Images d), e), f) from the copper bath with 30 ppm TU. Images g), h), i) from the copper bath with 60 ppm TU. Images j), k), l) from the copper bath with 90 ppm TU.

2.2.2.4 Film thickness characterization

The copper films obtained on GC were analysed using XRF spectroscopy to obtain the metal film thickness. The measurements were done in three different spots of each sample.

[TU] (ppm)	Cu thickness (μm)	Mean value (μm)	St. dev.
0	1.56	1.56	± 0.03
	1.56		
	1.61		
30	1.34	1.40	± 0.03
	1.40		
	1.40		
60	1.41	1.44	± 0.05
	1.53		
	1.44		
90	1.02	0.97	± 0.03
	0.96		
	0.97		

Table 2.2 - XRF analysis of copper films thickness obtained from the solutions with 0, 30, 60, 90 ppm TU on glassy carbon substrates by potentiostatic deposition.

The reduction of the thickness means value of the deposited samples increasing TU concentration, reported in Table 2.2, confirmed the suppressing behavior of thiourea on the copper growth which is the result of its effect on the nucleation mechanism. Compared to the value obtained without the addition of thiourea, the copper film thicknesses obtained adding 30 and 60 ppm were very similar, and similar were also the aspect of as deposited copper surfaces. The further addition of TU to 90 ppm in solution, caused a drastic reduction in thickness which could confirms the hypothesis on the formation of an electrodeposition-hindering, TU-derived organic film based on the morphological analysis of this sample and the voltammetric analysis of the deposition solution.

2.2.3 Discussion

Thiourea tends to react with copper ions in solution in two distinct ways based on its concentration and on the composition the electrodeposition solution. As seen in Fig. 2.1.b it was proposed that physio-chemical adsorption behavior of thiourea both on the glassy carbon surface and on the growing copper nuclei was the main effect observable from the CV analysis at the increasing of its concentration in solution.

The fitting of chronoamperometric data obtained at -0.12, -0.15 and -0.20 V as deposition potentials and 30, 60, and 90 ppm as TU concentration in solution with S.H. model showed a partial evolution from instantaneous nucleation to progressive nucleation as reported in Fig. 2.2. As reported in Tab. 2.1, the decrease of copper nuclei density with the increasing amount of TU was in accordance with the hypothesis: the addition of thiourea in the copper electrodeposition solution studied in this work promoted a progressive nucleation of copper.

The morphological analysis performed on copper film electrodeposited on GC substrates reported in Fig. 2.3 testified a grain refinement of the coating and an improvement of its aesthetic appearance increasing the thiourea amount up to 60 ppm. Morphological analysis also highlighted the formation of a copper film with an uncontrolled growth in presence of 90 ppm of TU, reasonably due the adsorption of an excess of TU-species on the cathode surface.

The increment of adsorbed TU-species at the increasing amount of dissolved TU in solution was also confirmed by XRF data which reported a reduction in copper thickness going from 0 to 90 ppm of TU dissolved. The electrodeposition tests were made at constant potential and constant time, the reduction in copper thickness due to the reduction in deposited charge were attributed to the hindering effect of thiourea on the electroactive surface of the GC cathode.

2.2.4 Final remarks and outlooks

Comparing the data obtained from solutions featuring different thiourea concentration it was found that this molecule acts as progressive nucleation promoter, increasing the diffusion coefficient of metal ions and lowering the number of nucleation sites on the electrode surface at the begin of the copper nucleation by its predominant physio-chemical adsorption behavior in the condition studied in this work. To verify the brightening agent role of thiourea, copper films were deposited from formulations with different amount of additive. Correlating the nucleation mechanism trend observed from chronoamperometric data with microscopic and macroscopic images it was proposed that the suppression effect of thiourea on the depositing copper charge was the main factor which caused the progressive nucleation mechanism and that this was a key element in the control of copper grain dimensions and structure. Testing the proposed alternative formulation for copper electrodeposition, I obtained that the concentration of 60 ppm of thiourea resulted the best compromise in terms of transition from an instantaneous to a progressive nucleation mechanism, morphological and aesthetic characteristics of the copper surface and thickness of the film. Thus, TU was proved to strongly influence the copper electrodeposition process acting as a catalyzer, in a sense, of the nucleation and growth process.

The combination of kinetic data and morphological analysis applied in this part of the present *Ph.D.* thesis could be applied to a different type of organic additive in order to link data obtainable prior the deposition of a metal film and the information obtainable directly from the metal film characterization.

Future analyses could link different organic additive to a specific pattern of kinetic data, helping to select the best range of additive concentration during the development of an innovative bath, without the need to explore extremely wide concentrations range. In my case, this type of analysis will be mandatory to select an organic additive to control tin nucleation and growth on the way to establish the best combination of organic additives in the bronze electrodeposition bath. In order to obtain an improvement of the bronze coatings structure and simplify the sulphuration process needed to obtain Cu_2ZnSnS_4.

3 Non-PGM sustainable catalytic surfaces for energy production

Much of the energy production is currently derived from fossil fuels [119]. The immoderate use of this type of nonrenewable resources could cause, in a relatively short time, the depletion of oil, leading to devastating consequences both from the energy point of view and from the political and socio-economic point of view. The dependence on these resources, in particular on the part of the most developed countries, derives mainly from the good energy yield of fossil fuels measured, in the economic sphere, by the EROEI (Energy Returned On Energy Invested) index. This is calculated as the ratio between the energy produced and the energy consumed in the production process [120] for each energy source. The EROEI makes it possible to determine whether the latter can satisfy the needs of a high industrialized society, for which an EROEI of between 5 and 9 is required (for example, photovoltaic EROEI = 6, nuclear EROEI = 5, oil and gas EROEI= 10 [121,122]). The EROEI index is not trivial to be calculated for each energy source, because it depends on different economic, political, and geographical parameters. Overall, the gradual reduction of fossil fuels, together with the considerable environmental impact caused by their use [123], led to find alternative sustainable systems for energy production and storage. Examples are the use of fuel cells for powering electric vehicles for city transport [124] or the use of fuel cells in regenerative fuel mode to store hydrogen as the energy vector [125].

3.1 Fuel cells technology

FCs (or Fuel Cells) are devices able to directly convert the chemical energy deriving from the oxidation of a given fuel into electrical energy, avoiding thermal processes. There has not been a serious commitment to the development and use of fuel cells before the end of the twentieth century. Only in the last two decades the greater interest in alternative methods for energy generation, which do not involve the use of non-renewable resources, has contributed to the increasingly in-depth study of this kind of devices.

One of the major advantages in the use of fuel cells lies in the type of reaction products. In the case of a hydrogen/oxygen fuel cell, for example, the overall reaction leads to the production of water, a by-product that does not constitute a risk factor at the environmental level [126]. Although there are various types, fuel cells have a common basic scheme: they are composed of two electrodes (anode and cathode) connected by an external circuit and separated by an electrolyte which, in most cases, determines the type of cell [127]. For example, in a cell with a polymeric membrane, at the anode we see the oxidation of hydrogen with the production of protons. The latter pass through the electrolyte, while the electrons reach the cathode through the external circuit.

$$H_2 \rightarrow 2H^+ + 2e^-$$

Simultaneously at the cathode we have reduction of oxygen to give O^{2-} which combines with the H^+ developed at the anode forming water.

$$O_2 + 4e^- \rightarrow 2O^{2-}$$
$$O^{2-} + 2H^+ \rightarrow H_2O$$

The electricity generated by the cell depends on the free energy of the reaction. The latter is in turn linked to the equilibrium potential difference between the two electrodes according to the relation:

$$\Delta G^0 = -nF\Delta E^0 \tag{3.1}$$

Where n represents the number of electrons exchanged, F the Faraday constant and ΔE^0 is the equilibrium potential difference defined as:

$$\Delta E^0 = E^0_{cathode} - E^0_{anode} \tag{3.2}$$

The experimentally measured potential is far from the thermodynamic equilibrium potential due to overvoltage phenomena (η) derived from the passage of current and other parasitic potential falls, such as the poor mass transport observed in some real systems [126]. A generic reaction that can occur on the electrode (cathode), $Ox + n^- \leftrightarrows Red$, can be decomposed in a series of elementary steps. For the electroactive species to take place, Ox, it must spread from the massive phase of the solution to the surface of the electrode, be absorbed on it and here undergoes a reduction; the product obtained, Red, must be desorbed and diffused in the mass phase of the solution (Fig. 3.1). The current produced on the electrode is directly related to the progress of the reaction under examination. If thermodynamically permissible, the forward speed is closely linked to the kinetics of the reaction itself. In this case, the speed depends on the slower elementary process, called the rate determining step, so it affects the amount of current generated. A certain overvoltage is connected to each current density produced by an elementary process. The total overvoltage can be considered as the sum of the various contributions related to the different phases of the reaction, listed below [128]:

- Overvoltage deriving from mass transfer (ηMT)

- Overvoltage due to electron transfer on the electrode surface (ηCT);
- Overvoltage related to reactions that occur before or after the charge transfer;
- Overvoltage due to phenomena occurring on the electrode surface such adsorption and desorption.

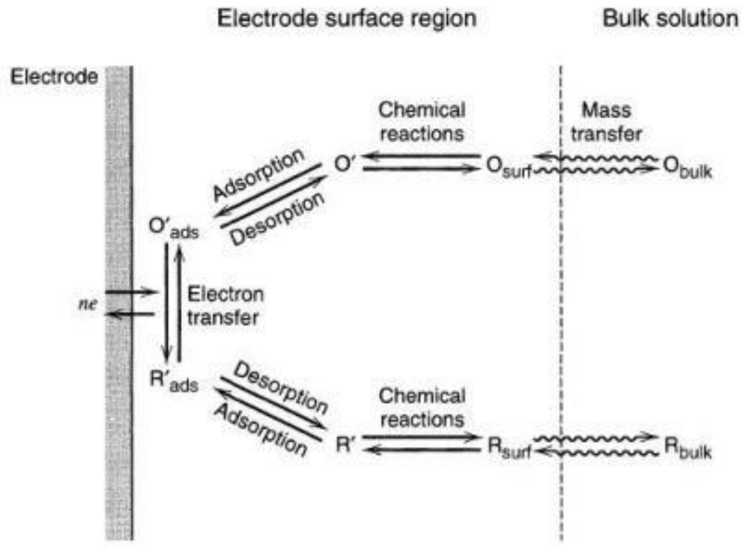

Figure 3.1 - Processes that constitute a generic reaction to the electrode [128].

Being heterogeneous reactions, the actual voltage is expressed as a function of the current density, j, and is defined as:

$$\Delta E(j) = E_c(j) - E_a(j) = \Delta E_0 - [|\eta_a(j)| + |\eta_c(j)| + R_e j] \tag{3.3}$$

Where Re is the resistance of the electrolyte, which contributes to the drop in potential, while η_a(j) and η_c(j) are the overvoltage potentials defined as [126]:

$$\eta_a(j) = E_a(j) - E_{0,a} \tag{3.4}$$

$$\eta_c(j) = E_c(j) - E_{0,c} \tag{3.5}$$

Overvoltage has an important influence on the efficiency of energy conversion. In general, energy efficiency, ε, is defined as the ratio between usable and produced energy. In a thermal machine the maximum efficiency is limited by the efficiency of Carnot, ε_R^{termic}, defined as:

$$\varepsilon_R^{termic} = \frac{W_r}{(-\Delta H)} = 1 - \frac{T_2}{T_1} \tag{3.6}$$

In which W_r is the reversible work, -ΔH the variation of enthalpy of the reaction and T_1 and T_2 the absolute temperatures for the process carried out by the thermal machine. While Carnot's efficiency often does not exceed 50% [129], fuel cells, in theory, would be able to convert all the energy provided by the reaction. For a cell the efficiency is calculated as:

$$\varepsilon_R^{cell} = \frac{W_e}{(-\Delta H)} = 1 - \frac{T\Delta S}{\Delta H} \tag{3.7}$$

In which W_e is the electric work and ΔS the variation of entropy. As previously anticipated, in real systems the overpowering phenomena negatively affect the yield. This effect is quantified by electrochemical efficiency, ε_V, which is also a useful value when comparing different fuel cells (with the same reaction):

$$\varepsilon_V = \frac{\Delta E}{\Delta E_0} = 1 - \frac{[|\eta_a(j)| + |\eta_c(j)| + R_e j]}{\Delta E_0} \tag{3.8}$$

Another negative contribution to efficiency is given by faradic efficiency, ε_F, defined as:

$$\varepsilon_F = \frac{I_{exp}}{I_{max}} = \frac{n_{exp} \cdot F \cdot v_i}{n_{max} \cdot F \cdot v_i} = \frac{n_{exp}}{n_{max}} \tag{3.9}$$

As can be deduced from the equation just described, the faradic efficiency considers possible phenomena of heterogeneous catalysis and parallel reactions that decrease the number of electrons exchanged causing a lowering of the produced current. In summary, the efficiency of a fuel cell, ε_{fc}, can be calculated by combining the contributions just shown:

$$\varepsilon_{fc} = \varepsilon_R^{cella} \cdot \varepsilon_V \cdot \varepsilon_F \cdot \varepsilon_H \cdot U \tag{3.10}$$

The last two terms in the equation are respectively the heat yield, ε_H, and the fuel utilization percentage, U [126]. From the constructive point of view fuel cells are generally made up of flat and porous electrodes interspersed with a thin layer of electrolyte. This configuration makes it possible to organize the cells in series, called "stacks", to have access to any power.

The reactions that take place in the fuel cell involve the oxidation of the hydrogen to the anode and the reduction of the oxygen at the cathode. Both reactions are thermodynamically favored but, especially in the case of oxygen reduction, there are limits linked to the kinetics that make the intervention of a catalyst necessary.

3.1.1 PEM or AEM-FCs?

State of the art low temperature proton exchange membrane fuel cells (PEM-FCs) are compact, yet high power-density systems ideal for automotive applications. Corrosion problems associated with the acidic nature of the proton exchange membrane (PEM) and the high cost of the platinum based anodic and cathodic electrocatalysts and of the Nafion® membrane, are the main limiting factor for these devices. Replacing the PEM with an alkaline anion exchange polymeric electrolyte (AEM) is one way to overcome these problems. H_2/O_2 fed anion exchange membrane fuel cells (AEM-FCs) are the most attractive alternative to traditional PEM-FCs. In fact, the alkaline environment is less corrosive for FC components and allows in principle the use of non-noble metal-based catalysts. Platinum-based electrocatalysts are the main limiting factor hindering the large-scale development of proton exchange membrane fuel cells. The major issues are the high cost of this metal and to the high Pt loading necessary to speed up the sluggish ORR reaction in H_2/O_2 PEM-FCs. Another limiting factor of platinum-based catalysts is the CO poisoning effect which hinders the catalytic effect of the precious metal surface. Unfortunately, Pt and its alloys are the best catalytic materials for the hydrogen reactions and for the oxygen reduction reaction performed in acidic environments. Platinum is also the only metal that can tolerate the strong acidic environment of proton exchange membranes. Operating in an alkaline environment is the only way to overcome these issues as in principle non platinum electrocatalysts (PGM), even non noble based electrocatalysts (non-PGM), can be used and the reactions kinetics are generally faster with respect to acidic conditions. Alkaline conditions are also much less corrosive for FCs components. Regarding the cathodic catalyst, in alkaline environment platinum can be replaced by choice of non-noble metals.

3.2 Oxygen reduction reaction in FCs

The oxygen reduction reaction (ORR) takes place at the cathode. In aqueous electrolytes, it can follow two different mechanisms: an indirect mechanism, with two electrons, with the formation of hydrogen peroxide which is subsequently reduced to water:

$$O_2 + 2e^- + 2H^+ \rightarrow H_2O_2$$
$$H_2O_2 + 2e^- + 2H^+ \rightarrow 2H_2O$$

and mechanism that leads directly to the production of water by exchanging four electrons [130]:

$$O_2 + 4e^- + 4H^+ \rightarrow 2H_2O$$

In terms of efficiency, the direct mechanism is preferable as it has a better energy conversion. Furthermore, hydrogen peroxide, formed in the indirect process, can produce free radicals with the risk of damage to the system [131]. In any case, both mechanisms depend the oxygen adsorption and dissociation steps, specific for each type of catalyst used [126].

This part of my *Ph.D.* thesisis focused on the study of non-PGM catalysts enhancing the oxygen reduction reaction in AEM-FCs which were selected as the election type of fuel cells for the advantages with respect to PEM-FCs already discussed in the previous section.

In this regard a potential cathode electrocatalyst based on pyrolyzed carbon was studied starting from waste materials such as tires. End of life tires (ELTs) show a difficult disposal and recycling process. Their methods of recovery can be divided in three main types: physical, chemical, and thermal. In the last method, we sought a way of recovering ELTs using pyrolysis [132]. The presence of carbon black, an excellent absorber, employed as filler in ELTs, enables the use of microwave pyrolysis, in which electromagnetic energy is transformed into thermal energy [133], and allows uniform heating [134]. Chars obtained by pyrolysis can be used to produce electrocatalysts for fuel cells. Their catalytic activity depends on the presence of metals that speed up the ORR kinetics [135] coupled with their high porosity that allows to absorb large oxygen amounts [132,136–140].

The aim of this work was to improve the activity of raw chars using simple and cheap methods such as electrodeposition. Considering the catalytic activities of single metals in chars, Co and Cu show a synergic activity: the first one assists the electron transfer and the second one enhances oxygen adsorption onto the electrode surface; in particular, Co can break the O-O bond of O_2 molecules, accelerating the first reaction step of ORR [135]. The cheapest electrodes can be produced by doping cheap materials with nanoparticles [141] which can increase peak current and reduce overpotential promoting reaction

kinetics [142,143]. Particles at the nanometre scale can be obtained by using different ways: (I) chemical reduction from colloidal solution; (II) electrodeposition [144]; and (III) sonochemical reduction. In this part of my *Ph.D.* thesis, I applied the last two methods to increase cobalt and copper amount in ELTs chars.

3.2.1 Study of catalytic activity by RRDE

The RRDE technique allows a direct and complete study of the oxygen reduction reaction as it allows us to estimate both the reaction intermediates and the secondary products. This rotating electrode hydrodynamic voltammetric technique involves the use of two working electrodes. A central disk and a concentric ring are separated by an insulating layer and mounted on the lower interface of a cylindrical support of inert material in which it has metal contacts and that is screwed to the rotation system. The disc and the ring act as separate working electrodes or a controlled potential is applied to each of them independently of each other (Fig. 3.2).

Figure 3.2 - RRDE Electrode with glassy carbon disc and platinum ring.

The rotation of the electrode causes the solution to drag towards the surface and the laminar motion in the vicinity of the electrode causes a tangential displacement, therefore the concentric geometry ensures that the electroactive species encounters the primary electrode (the central one) and subsequently the products of the reaction are transported to the ring where a second redox reaction takes place, Fig. 3.3.

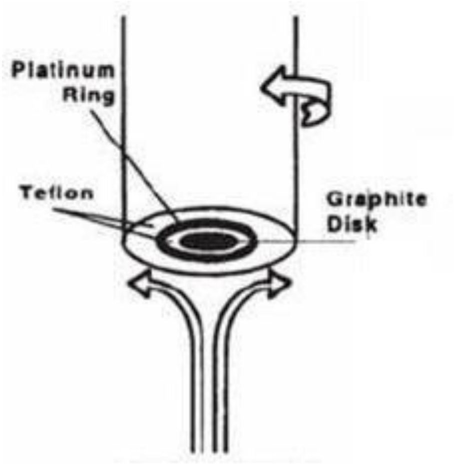

Figure 3.3 - Reagent flow on the electrode.

In the RRDE technique the disk current is the sum of all possible faradic currents that occur at that given potential. The electrode rotation causes the removal of the species produced after an electrochemical reaction from the disk to the ring. The latter is held to such a potential as to cause a preferential reaction (the opposite that occurs to the disc) of a single species, in such a way as to estimate the latter.

The RRDE technique is used in the study of the oxygen reduction reaction where it allows to estimate the number of electrons exchanged and the quantities of water and hydrogen peroxide produced during the reaction. Potential scanning takes place on the disk while the ring is set to a constant potential so that the oxygen reduction reaction (to give H_2O or H_2O_2) takes place on the disk and the oxidation of hydrogen peroxide is eventually present at the ring produced on the disc. In the operating conditions the current measured at the disk I_D is given by the sum of all the charge transfer processes that take place in the working potential range, and therefore is:

$$I_D = I_{H2O2} + I_{H2O} \tag{3.11}$$

By applying to the ring, a potential finely tuned for the oxidation of the hydrogen peroxide produced at the disc, the current recorded on the ring (I_R) is due to the fraction of hydrogen peroxide molecules that reach the ring from the disc.

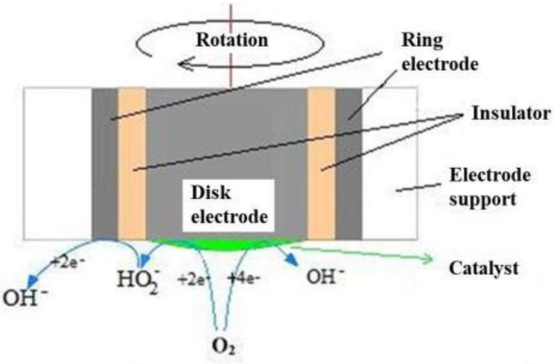

Figure 3.4 Reactions that occur on the RRDE electrode

It is therefore necessary to introduce a term N (Collection Efficiency) defined as the fraction of matter that passes from the disk to the ring and that the ring manages to "capture". In fact, not all the molecules produced will be able to reach the ring. The theoretical value of this parameter depends on the geometry of the system and can be calculated by knowing the three rays of the electrodes used (disc radius, ring radius and Teflon separator radius). The value must be between 0 and 1 and is generally between 0.2-0.3. The N value can be obtained experimentally, by performing a potential scan of a solution containing a known redox pair (generally ferrocyanide/ferricyanide) and calculating the ratio between the limit currents of the ring and of the disc (I_R/ I_D). The fraction of current measured at the disc due to the oxygen molecules reduced to H_2O_2 (I_{H2O2}) is given by the ratio between the current measured at the ring and N:

$$I_{H2O2} = I_R/N \tag{3.12}$$

The difference can therefore be obtained from the current due to the reduction of oxygen to water:

$$I_{H2O} = I_D - I_{H2O2} \tag{3.13}$$

The ratio between the total current measured on the disc and the number of electrons exchanged (n) must be equal to the sum of the currents caused by the reduction of oxygen to water and hydrogen peroxide:

$$\frac{I_D}{n} = \frac{I_{H2O}}{4} + \frac{I_{H2O2}}{2} \tag{3.14}$$

By rearranging the terms, one finds the formula for calculating the number of electrons exchanged per oxygen molecule:

$$n = \frac{4I_D}{I_D + I_R/N} = \frac{4I_D}{I_D + I_{H2O2}} \tag{3.15}$$

3.3 Deposition of cobalt and copper on row chars from End-of-Life tyres as non-PGM catalyst for ORR in AEM-FCs

In this section will be presented the study of two different methods to enrich raw chars derived from pyrolyzed waste tires. Co and Cu NPs enriched chars were studied as alternative catalysts to be implemented in AEM-FCs due to their ability to speed up oxygen reduction reaction in the cathodic side of the cell. The concept behind this work regards the possibility to substitute PGM which to the state of the art represent the best choice in terms of fuel cell catalysts.

3.3.1 Experimental

In this study, it was combined the use of cheap electrodes made of chars obtained from recycled tyres with the enrichment of earth abundant (and cheap) metals, namely Co and Cu. Were compared deposition methods and effective amount of metal deposited with their electrocatalytic performance. In addition, the evolution of deposited materials on the optimized electrode before and after electrocatalysis was monitored using scanning transmission electron microscopy (STEM) and X-Ray photoelectron spectroscopy (XPS).

Char materials were obtained from Michelin tyres (model Agilis 81 195/65 R16C) using the experimental conditions defined in [145]. Tyres were fragmented and dried in an oven with a temperature of 65 °C for 48 h. Dried fragments were pyrolyzed in a microwave oven MW Lab Unit (Microglass) working at 2.45 GHz with a maximum power of 2.4 kW. The solid residue was homogenized obtaining raw chars. The sample with the highest power/mass^2 (P/M^2) ratio during pyrolysis (see [146]) was labelled "*CHraw*" and was selected for the metal enrichment process below.

3.3.1.1 Sonochemical deposition

Sonochemical deposition was applied to the *CHraw* sample following the experimental procedures reported in [147,148]. Co nanoparticles were prepared from an aqueous solution 0.2 M of cobalt hydroxide carbonate ($Co_2CO_3(OH)_2$) with the addition of citric acid 0.05 M to favor the carbonate dissolution and control nanoparticles' structure and dimensions. Similarly, Cu nanoparticles were prepared from a similar solution with $CuCl_2$. A volume (5 mL) of ethanol and 25 mg of chars were added to the solution and then sonicated for 90 min. At the end of the deposition, samples were dried and centrifuged at room temperature to speed up the drying process to obtain two sets of samples: char with sonochemically deposited Cu and Co labelled, respectively, "*CHscCu*" and "*CHscCo*".

3.3.1.2 Electrochemical deposition

Electrochemical deposition of Co was performed using a char-based ink (using sample *CHraw*) and dropcasting it on a glassy carbon electrode, using the method described in [149]. To determine the optimal potential and experimental conditions for the deposition, a cyclic voltammetry on the ink in a buffer solution $NH_4OH/HClO_4$ (pH = 9.2) containing $5 \cdot 10^{-3}$ M Co(II) was performed. The deposition was then conducted through chronoamperometry with a constant potential of -850 mV (vs. Ag/AgCl/KCl sat.) under constant magnetic stirring. Before the deposition, to clean the deposited ink surface, was performed a linear scanning voltammetry of stripping in a cleaning solution from -750 to 600 mV (vs. Ag/AgCl/KCl sat.) with a scan rate of 10 mV/s. The electrode was transferred in a beaker containing 50 mL of Co(II) solution, previously flushed with N_2 for 30 min. Chronoamperometry with a constant potential of -850 mV (vs. Ag/AgCl/KCl sat.) was performed as a function of time to make a cobalt electrochemical deposition series with electrodepositions lasting 5, 15, 30, 60 and 90 s. The resulting samples were labelled as "*CHecCo5s*", "*CHecCo15s*", "*CHecCo30s*", "*CHecCo60s*", and "*CHecCo90s*", respectively. The amount of Co deposited on the electrode was theoretically calculated by Faraday's laws of electrolysis and empirically measured by inductively coupled plasma atomic emission spectroscopy (ICP-AES) analysis. Deposited quantities are reported in Table 3.1. The stability of the deposited material was confirmed by stripping linear sweep voltammetry (LSV) where no dissolution peak is observed.

Sample	**Time (s)**	**Charge (C)**	**Deposited Mass (mg)**
CHecCo5s	5	$1.97 \cdot 10^{-3}$	$6.02 \cdot 10^{-4}$
CHecCo15s	15	$3.67 \cdot 10^{-3}$	$1.12 \cdot 10^{-3}$
CHecCo30s	30	$5.874 \cdot 10^{-3}$	$1.79 \cdot 10^{-3}$
CHecCo60s	60	$7.36 \cdot 10^{-3}$	$2.25 \cdot 10^{-3}$
CHecCo90s	90	$1.017 \cdot 10^{-3}$	$3.11 \cdot 10^{-3}$

Table 3.1 - Deposited charge related to different Co deposition time and associated deposited mass per electrode.

3.3.1.3 Inductively Coupled Plasma-Atomic Emission Spectroscopy (ICP-AES)

Metal content deposition was evaluated through ICP-AES analysis, carried out using a microwave mineraliser, (CEM Mars Xpress) and a spectrophotometer with inductively coupled argon plasma (Perkin Elmer Optima 2000 OES DV). The results are reported in Table 3.2.

Sample	Cu (ppm)	Cu (mg)	Co (ppm)	Co (mg)
CHraw	38.5	$8.47 \cdot 10^{-6}$	162	$3.56 \cdot 10^{-5}$
CHscCu	1140	$2.21 \cdot 10^{-4}$	/	/
CHscCo	/	/	235000	$5.17 \cdot 10^{-2}$
CHecCo5s	/	/	1800	$3.96 \cdot 10^{-4}$
CHecCo15s	/	/	4710	$1.04 \cdot 10^{-3}$
CHecCo30s	/	/	7140	$1.57 \cdot 10^{-3}$
CHecCo60s	/	/	13600	$2.98 \cdot 10^{-3}$
CHecCo90s	/	/	19485	$4.27 \cdot 10^{-3}$

Table 3.2 - Metal content from ICP-AES analysis after sonochemical (*CHsc*) and electrochemical (*CHec*).

3.3.1.4 Scanning transmission Electron Microscopy (STEM)

Samples for STEM analyses were prepared by finely crushing powders of electrode material and depositing them directly onto (10 nm) holy carbon films supported by standard TEM copper grids following the procedure described in [150]. STEM analyses were performed using a double aberration corrected scanning/transmission electron microscope operating at 200 KeV (JEM 2200FS, JEOL Japan Ltd.). High angle annular dark field (HAADF) STEM images were obtained using an inner collection semi-angle of 70 mrad and an outer collection semi-angle of 180 mrad. STEM energy dispersive X-ray (EDX) analyses were done using a 100 mm^2 UltraDry windowless EDX silicon drift detector and the Pathfinder™ X-ray microanalysis software (Noran system 7, Thermo Fisher Scientific Inc.) for data analysis and display.

3.3.1.5 X-ray Photoelectron Spectroscopy (XPS)

XPS was done in ultra-high vacuum conditions (UHV) with an Al Kα X-ray source at 1486.6 eV (VSW Scientific Instrument Limited, model TA10) and a hemispheric magnetic analyser (VSW Scientific Instrument Limited, model HA100) with a 12-channel detector. The source power was set to 120W with a 44-eV collection energy. Samples were transferred into the UHV chamber and cleaned with a low energy sputtering for 3 min before starting the analyses. Spectra were acquired with an energy dispersion of 0.5 eV/channel and 0.1 eV for overview and high-resolution spectra acquisition, respectively. Spectra were analysed using CasaXPS software. Calibration was done fixing the energy of the aliphatic C 1s transition at 284.8 eV [151–153].

3.3.1.6 Electrochemical measurements

Electrochemical characterisation involved cyclic voltammetry (CV) and LSV using Rotating Ring-Disk Electrode (RRDE). The experimental setting was composed by a cell containing a 0.1 M KOH solution and three electrodes: (a) reference electrode Ag/AgCl/KCl sat. with a potential of +0.197 V with respect to a Normal Hydrogen Electrode (NHE); (b) platinum wire as counter electrode; and (c) RRDE as working electrodes, consisting of a glassy carbon (GC) disk insert (Ø 5 mm; $A = 0.196\ cm^2$) and a Pt ring ($A = 0.11\ cm^2$). Each electrode was connected to a PGSTAT 100 N bi-potentiostat able to simultaneously record both disk and ring current. The RRDE electrode was attached to a modulated speed rotator (MSR) model 636 A from Pine Instrument Co. Electrocatalytic activity of chars was tested preparing 0.5 g of an ink which contained catalyst (2%wt), water (52%wt), ethanol (26%wt) and Nafion solution (20%wt). The ink was sonicated for 30 min and drop-casted on the glassy carbon electrode using a 20 μL pipette. The resulting electrode was dried at room temperature. To verify the electrocatalytic activity of the samples, cyclic voltammetry was carried out with a potential range from +0.1 to -0.85 V with a scan rate of 5 mV/s. The 0.1 M KOH solution was saturated O_2 gases. In all cases, a clear oxygen reduction peak is observed under O_2

saturation. As a control experiment, with a saturation of the solution with N_2, it was verified that the oxygen reduction peak was not observed. Starting from these results, RRDE experiments were performed using a scan rate of 5 mV/s in the potential range from +0.1 to -0.85 V (vs. Ag/AgCl/KCl sat.) for the modified GC electrode while the Pt ring electrode was held at a potential of +0.6 mV. Disk and ring current were obtained using RRDE electrode rotational speed of 1600 revolutions per minute (rpm). RRDE calibration was led for each sample determining empirically the collection efficiency number (N) following the RRDE manufacturer (Pine Instrument Co.) procedure through ring (I_R)/disk (I_D) current ratio ($N = I_R/I_D$) registered during LSV of a N_2 saturated solution of 10 ppm $K_3Fe(CN)_6$ in KCl 0.1 M at scan rate of 5 mV/s in the potential range of +0.4 V to -1.3 V and holding the ring with constant potential of +0.6 V at 1600 rpm.

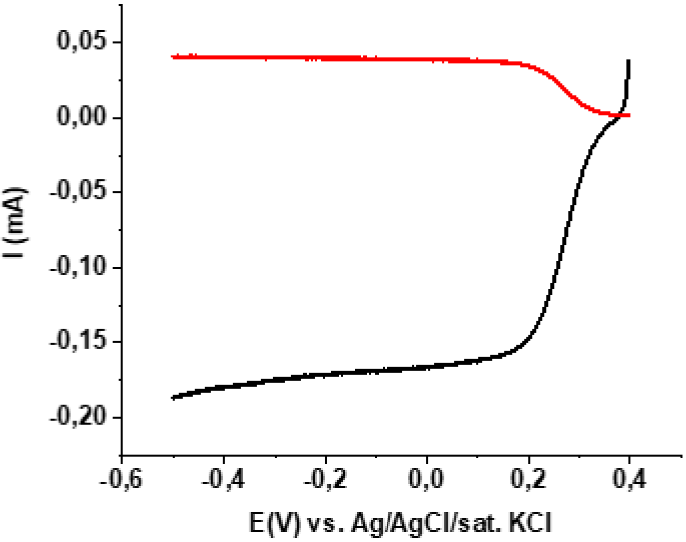

Figure 3.5 - Typical LSV obtained from sample *CHecCo30s* by RRDE with a solution of $K_3Fe(CN)_6$ to calculate the collection efficiency (N) (Black line I_D, red line I_R).

Once N was determined, the electron transfer number exchanged per O_2 molecule occurring during the ORR process (n) was calculated using Equation (3.15) [154], for each sample.

$$n = \frac{4I_D}{I_D + I_R/N} \tag{3.15}$$

Based on the number of electrons exchanged per O_2 molecule, the H_2O and H_2O_2 percentages produced during the ORR process were calculated by Equation (3.16).

$$\%H_2O_2 = \left(2 - \frac{n}{2}\right) \cdot 100 \tag{3.16}$$

The onset potential was estimated through the determination of the first derivative curve of the disk current SI [155]. The onset potential is the value of potential that coincides with the intersection among the curve tangent and the continuation of baseline.

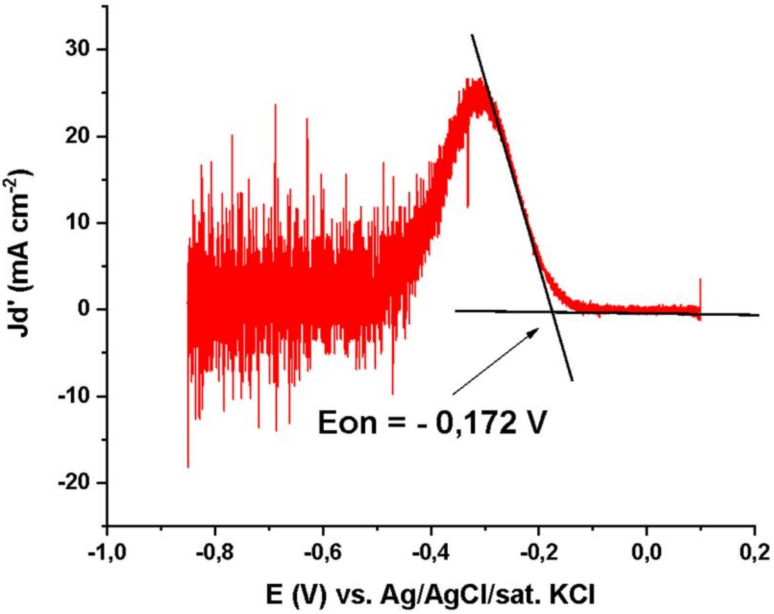

Figure 3.6 - Example of first derivative curve of disk current to determine onset potential value on *CHec30s*.

3.3.2 Results

The onset potential and the number of exchanged electrons was the parameters considered to state the catalytic activity of electrocatalysts. The onset potential represents the limit value at which a reaction starts to evolve in significant quantities while the number of exchanged electrons allows the assessment of the principal reaction pathway in ORR. A catalyst should preferably promote a four-electron exchange leading to H_2O formation and avoid a two-electron exchange that results in H_2O_2 because of its negative influence on yields and corrosive effects on the membrane used in fuel cells. The results from linear sweep voltammetry (LSV) are reported in Figure 3.7.

Electrochemical data (Table 3.3) demonstrated an improvement in catalytic activity of the electrochemical modified char.

Sample	**E_{ON} (V)**	**N Experimental**	**N Empirical**	**% H_2O_2**
CHraw	-0.21	3.53	0.25	23.5
CHscCu	-0.225	2.91	0.20	54.5
CHscCo	-0.183	3.19	0.21	40.5
CHecCo5s	-0.184	3.94	0.25	3.0
CHecCo15s	-0.180	3.95	0.25	2.5
CHecCo30s	-0.172	3.98	0.25	1.0
CHecCo60s	-0.184	3.96	0.25	2.0
CHecCo90s	-0.193	3.94	0.25	3.0

Table 3.3 - Synopsis of electrolytic data collected from sonochemical and electrochemical deposition of Co and Cu.

In the case of sonochemical deposition, it was possible to observe a worsening in catalytic activity compared to ink exclusively made of *CHraw*. This can be attributed to an excess of material deposited (as confirmed by ICP-AES analysis). Co fully covering the char surface would prevent the correct adsorption of oxygen. This led to more negative values of the onset potential compared to the one measured for *CHraw*. In addition, a decrease in exchanged electrons (around 2.90) was observed with a consequent increase in the percentage of hydrogen peroxide produced (around 15%). Cu deposition brought worse catalysis yield, with a production of 40% of hydrogen peroxide (3.19 exchanged electrons). Ink samples of *CHraw* after Co electrodeposition showed an increased catalytic efficiency with respect to ink exclusively made of char. In fact, a higher onset potential of -197 mV was observed with an electron exchange close to 4, and a production of hydrogen peroxide always under 2%.

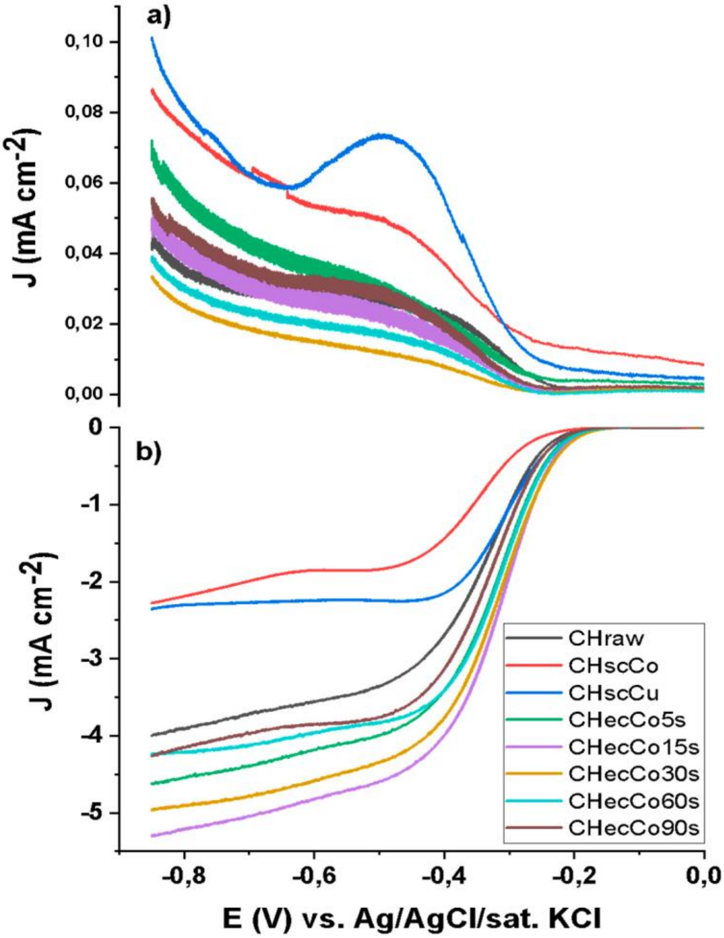

Figure 3.7 - ORR RRDE electrocatalytic performance of samples obtained from sonochemical and electrochemical deposition of Co and Cu on *CHraw*: (a) ring; and (b) disk current density.

In Figure 3.8, using the data shown in Figure 3.7 and Table 3.3, for the electrochemical deposition case, were plotted the potential values as a function of deposition time. Data showed a volcano-like trend, in agreement with Sabatier principle [156]. This is typical of a mechanism where the O_2 adsorption is the rate-determining step. The increase in potential on the left branch of the “volcano” profile can be attributed to the increase of deposited

Co onto the surface, while the decrease on the right branch can be associated with an excessive coverage in Co with a consequent reduced capability of oxygen adsorption from the underneath char. Alongside the increase in deposition time, a progressive enhancement in catalytic activity was observed, peaking at a deposition time of 30 s. In this case, a substantial enhancement of all studied parameters was observed, obtaining an onset potential of -172 mV, exchanged electrons up to 3.98 per O_2 and hydrogen peroxide production under 1% (0.65%).

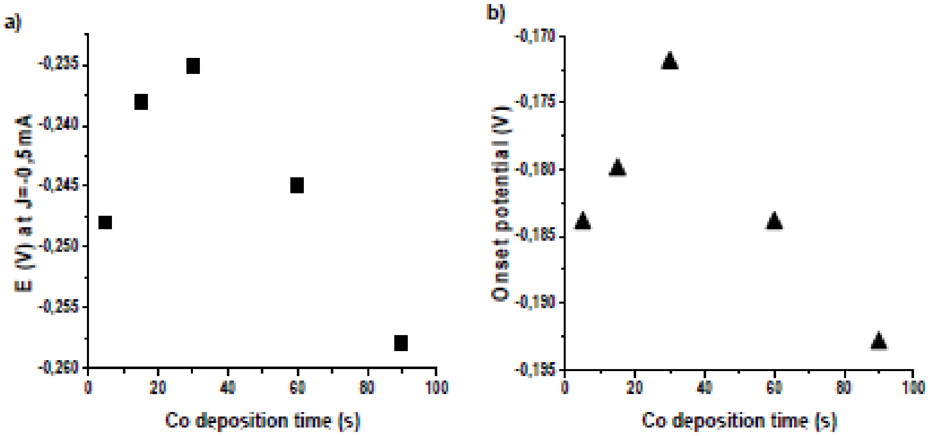

Figure 3.8 - Volcano curves as obtained by plotting: (a) the potential values at j = -0.5 mA cm^{-2}; and (b) onset potential values versus time of Co electrochemical deposition.

To verify the stability of sample *CHecCo30s*, it was tested for 10 min in an alkaline solution saturated with O_2 at a potential of -0.6 V. In Figure 3.9, can be observed that under these conditions the number of exchanged electrons per oxygen molecule were maintained constant (near $4e^-/O_2$) demonstrating a good stability. The ORR mechanism associated with the optimal sample implies the breakdown of the O-O bond without any intermediate steps by observing a $4e^-$ exchange for O_2 molecule, meaning a direct formation of water molecules.

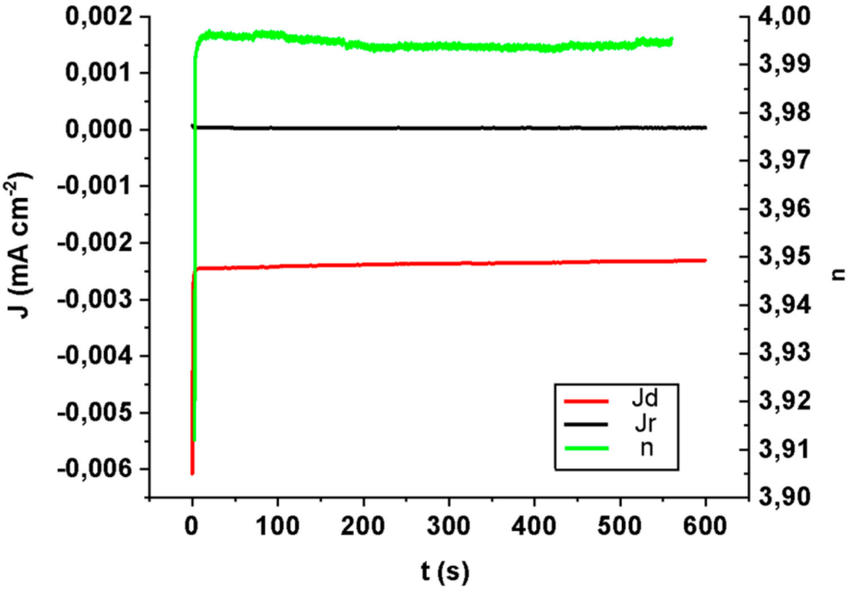

Figure 3.9 - Time stability test (galvanostatic RRDE experiment) for a sample after electrochemical deposition f Co: ring and disk currents, together with n, the number of exchanged electrons per O_2 molecule over time.

CHraw powder samples were investigated by STEM; overview HAADF images of typical char grains can be seen in Figure 3.10. Grains of submicron size showed the presence of nanoparticles (indicated by the red arrow in Fig. 3.10.a). High-Resolution Bright Field (HR-BF) STEM images revealed the crystalline nature of the nanoparticles, as well as a mixed amorphous and graphitised char material (Figure 3.10.c,d). EDX analysis on the nanoparticle showed they are made of Zn and S. These nanoparticles are the remnants of the vulcanisation process, as reported in [157]. The ORR mechanism is improved by the presence of the metal; however, the effect is not at the same level as for the added Co material (see results for *CHraw*).

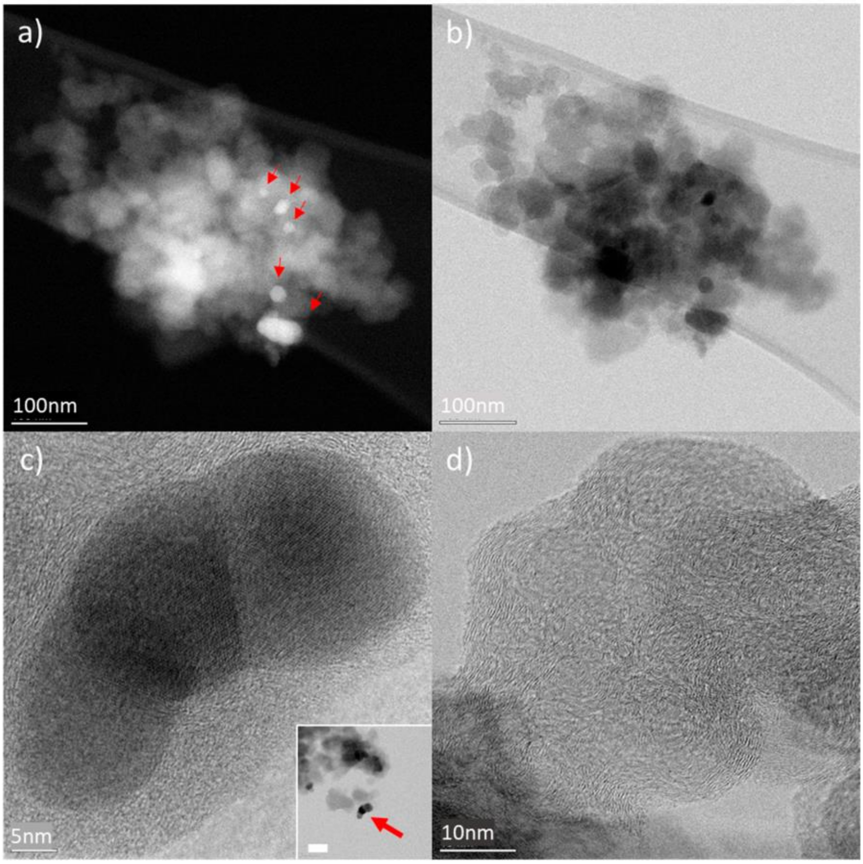

Figure 3.10 - HAADF (a) and BF STEM (b) images of typical sub-micron clusters of raw char sample crashed powder supported by amorphous carbon film. Z contract in HAADF STEM images show the presence of inorganic nanocrystals (indicated by the red arrows). HR-BF STEM images of nanoparticles showing good crystallinity (a) as well as the degree of graphitisation of the char material (c). Inset in (c) shows an overview of the flake containing the nanoparticles (bar corresponds to 50 nm).

The sample with optimal electrocatalytic performance corresponding to 30 sec. deposition (sample *CHecCo30s*) was investigated by STEM before and after electrocatalysis. The sample after electrodeposition showed a uniform coverage of Co in the form of a network-like structure, as shown in the HAADF images in Figure 3.11. Bigger Nanoparticles in Figure 3.11.a are ZnS NPs, while whiter areas in Figure 3.11.b are associated to Nafion® ($C_7HF_{13}O_5S{\cdot}C_2F_4$) residues.

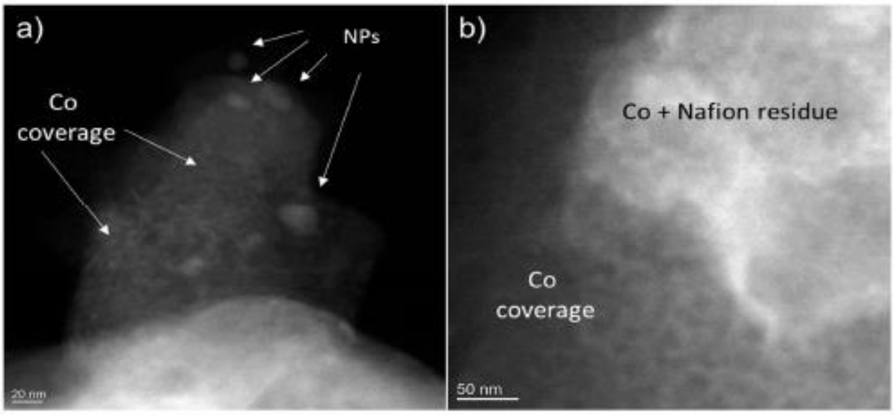

Figure 3.11 - HAADF images of typical char grains after Co electrodeposition. Larger NPs in (a) are ZnS. Co is uniformly covering the grains surfaces with a network of islands. Whiter areas in (b) contain fluorine due to the presence of residues of Nafion® used to treat the sample.

HAADF STEM images (Figure 3.12) showed that after the stability measurements two types of materials with different textures were observed on the chars: well defined nanoparticles and smaller accumulation of material at the edges of char grains. EDX analyses confirmed that bigger nanoparticles are made of ZnS, while the other material was due to the redistribution of Co during the electrocatalysis process where the Co network broke-up with migration of Co material towards the edges and grain boundaries of char.

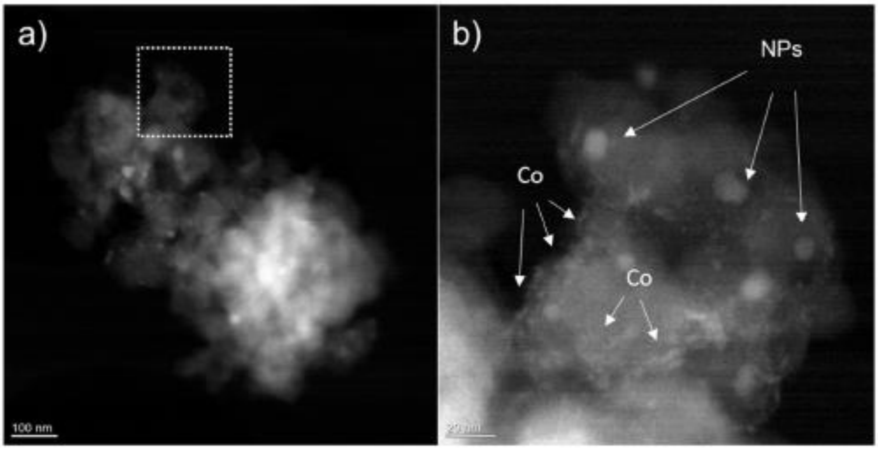

Figure 3.12 - (a) HAADF STEM overview image showing a grain of material after stability measurements. (b) A higher magnification image corresponding to the dotted box areas in (a). Nanoparticles are visible as well as the remnant of the Co electrodeposited network.

High-resolution XPS spectra obtained in the ranges 815–765 and 1055–1015 eV around the Co 2p and Zn 2p transition, respectively, are reported in Figure 3.13. Spectra were acquired for samples before and after the stability measurements. The Zn 2p profile remained the same with the addition of a shoulder towards high energy, indicating an increase in oxidation of the ZnS nanoparticles. A shift towards higher energies was visible in the Co peak, suggesting oxidation of the material. Such oxidation did not influence the catalytic efficiency of the cell, as shown in Figure 3.9.

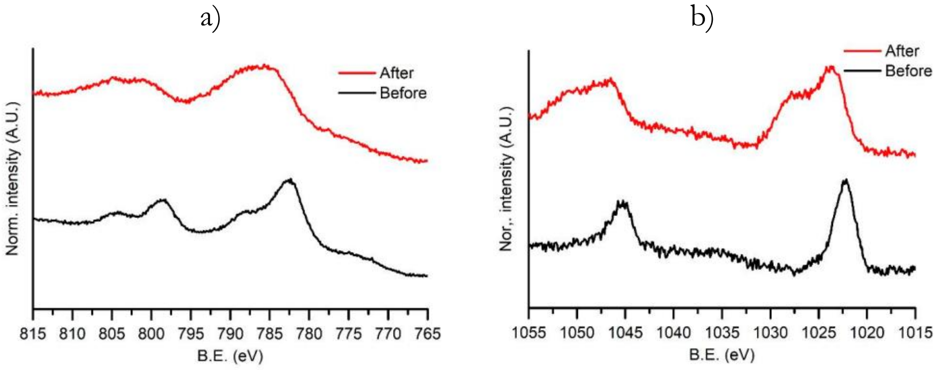

Figure 3.13 - (a) High-resolution XPS for the Co 2p peaks in the range 815–765 eV. (b) High-resolution XPS for the Zn 2p peaks in the range 1055–1015.

3.3.3 Final remarks and outlooks

With the aim of finding an efficient substitute to noble metals in the catalysis of oxygen reduction reaction and at the same time to efficiently recycle waste automobile tyres, efforts were made to strengthen the catalytic activity of chars obtained from MAP of waste tyres. Two metal enrichment methods, namely sonochemical and electrochemical deposition, were used to deposit Co and Cu on char. The catalytic efficiency of samples was evaluated by obtaining onset potential values and the number of exchanged electrons in oxygen reduction reaction in alkaline medium using hydrodynamic voltammetry RRDE technique. Samples enriched by electrochemical deposition were found to have better catalytic efficiency with respect to sonochemical deposited samples where excessive material was deposited on the char surfaces. Char electrodes enriched with Co showed a maximum positive shift of 40 mV with respect to raw char electrodes. This brought the number of exchanged electrons per O_2 molecule during ORR close to 4 (Pt value) corresponding to a reduction in the production of unwanted oxygen peroxide from 23% for raw chars to 1% for the optimal deposition conditions of *CHecCo30s* sample. In addition, chars deposited with sonochemical Cu, although showing a similar onset potential as for the optimal Co samples, resulted in a production of 40% H_2O_2 corresponding to a reduced catalytic efficiency. Galvanostatic measurements of the optimal sample showed good catalytic efficiency stability over time. STEM analyses showed a uniform network-like Co coverage of the char surface before the stability test, whereas material rearrangement was observed after it. XPS analysis showed Co slightly oxidised after the treatment. Both changes did not seem to interfere with the efficiency of the semi-cell. This part of the thesis proved that it is possible to increase the catalytic activity of chars after deposition of an inexpensive metal such as Co: chars derived from end-of-life tyres can be easily transformed with a sustainable treatment in both economic and energetic terms (electrodeposition) to produce green energy. Future developments will regard the assembly of a complete AEM-FC to test its performances in terms of energy production and stability over work cycles.

4 Thin palladium films exploiting an electroless route

4.1 Introduction

The importance of palladium lies in its unique ability to adsorb hydrogen and catalyse hydrogenation and dehydrogenation reactions. Palladium plays a fundamental role in a wide range of applications: in the energy field for the production [158], storage [159] and use of hydrogen in catalytic fuel cells [160–162] but even in the chemical synthesis field with application in optoelectronics [163] and biology [164,165]. It is estimated that palladium is the element with the highest hydrogen adsorption capacity, managing to store volumes equal to 935 times its own [166]. These characteristics make this element extremely functional for the development and production of new energy systems not dependent on oil, such as fuel cells [159]. Nowadays, palladium is mainly used in the automotive sector, in the production of catalytic converters: in 2020 China requested a 30% increase in the quantity of palladium inside them [167]. The major problem related to the use of palladium is its high and constantly growing cost, due to the scarce quantity extracted around the world, the increasing need to transition from an economy based on oil to one based on hydrogen [168] and the very high demand from the automotive sector to achieve increasingly stringent environmental standards in vehicle emissions. To stem this defect and make an eco-sustainable system advantageous, even economically, it is essential to study the techniques for producing thin films of palladium, to avoid the use of massive metal while preserving the surface properties that have made it so widespread. The application of precious metal coatings in different sectors is always facing the challenge to reduce the metal amount still maintaining the surface properties obtained by the material (e.g., corrosion resistance, wear resistance, conductivity, aesthetical appearance, catalytic performance, etc.) to improve the economic sustainability of the process. Looking to the comparison of the price evolution (€/g, Figure 4.1) of the three most employed precious metals from the automotive to the luxury industrial sectors, can be seen that palladium has had the greatest price growth in the last four years. For this reason, the research and development of a highly sustainable route to produce high quality palladium coatings could be of interest from different points of view of application.

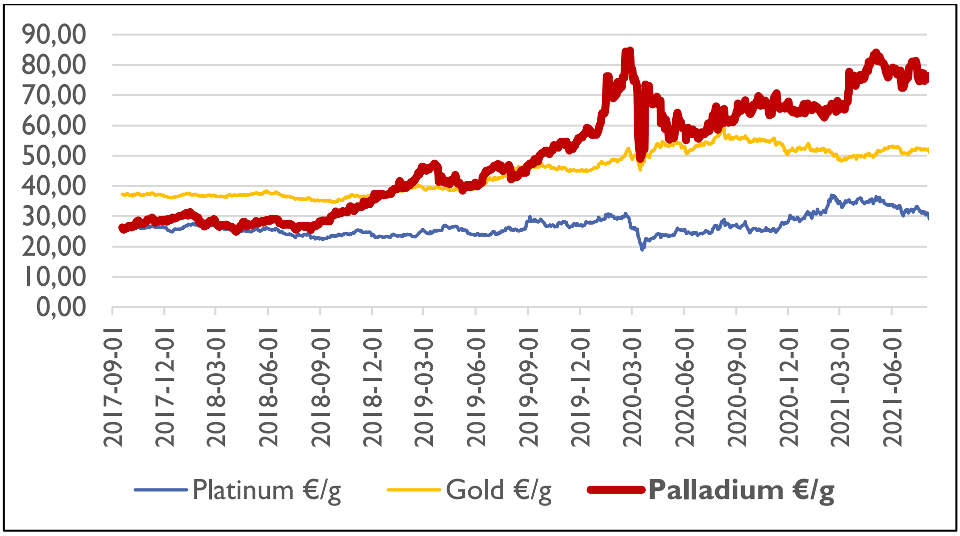

Figure 4.1 - Platinum, gold, and palladium price trends over last four years (Source: www.heraeus.com).

Palladium is particularly popular in the electroplating industry for luxury jewellery and accessories in which is used as intermediate layer and/or top layer with thickness ranging from 0.1 μm to 5 μm [85]. In this sector, palladium films obtained from an electroless deposition could open the doors to a more cost-effective industrial process respect to the electrodeposition one.

Electroless deposition techniques differ from electroplating due to the absence of external current designed to promote the reduction of the species to be deposited on the substrate. In electroplating techniques, the growth of the deposit depends on the surface current density, which, for irregular geometries is not uniformly distributed over the cathodic area, leading to non-uniform deposits. This problem does not occur with electroless depositions (given the non-use of external current) making these techniques excellent for use on substrates with exotic and irregular shapes [169].

The aim of this part of my *Ph.D.* work was the development of a cost-effective technique or combination of techniques able to produce high quality Pd thin films with tailorable thickness onto copper substrates. To obtain a Pd layer with a very cost-effective procedure, electroless plating techniques were selected as the election procedures.

Copper was chosen as base material because is a common material used as substrate as well as intermediate layer in electroplating and surface finishing industry thanks its semi-noble behaviour, the high levelling power (if electroplated), and the brightness of the copper surfaces. Unfortunately, the electroless deposition of palladium on copper is not trivial and can lead to some issues. These problems come to the presence of concentrated ammonia in most of the electroless palladium baths, in fact a pre-deposition step is mandatory on Cu substrates. As proof of the fact that ammonia acts as an etchant on copper surfaces, its effect has also been studied in literature as a copper surface polishing agent [170]. In the case of this work the ammonia etchant behaviour is detrimental for the formation of a continuous and adherent Pd layer.

Two different types of electroless deposition techniques were used, displacement deposition and chemical deposition. The displacement deposition technique (PDP, Palladium Displacement Plating) is a process in which the ions of a metal nobler than the metal substrate are reduced on the substrate due to a galvanic exchange reaction, producing a deposited film [169].

Chemical plating is the most used electroless deposition technique [171] (PCP, Palladium Chemical Plating) because is more efficient than displacement plating baths allowing to obtain palladium deposition rates of over 2.5 μm/h at 50-60 °C of deposition temperature [172]. The deposit is formed exclusively on catalytically active substrates, thanks to the reduction of metal ions in solution by a reducing agent present in the bath. Chemical deposition is defined as a process in which one has the formation of a metal film through a controlled chemical reaction, catalysed by the same deposited metal [173]. This technique is widely used to deposit metallic films on non-metallic surfaces, e.g. glass and ceramics, through a pre-treatment to make catalytically activates the surfaces [174,175].

Unlike chemical deposition processes, displacement plating does not include external reducing agent, it ends as soon as the noblest metal, palladium in this case, completely covered the substrate. For this reason, this technique can produce only very thin films, that is an advantage for catalytic applications but an issue for decorative applications. Chemical plating has the advantage of selectively deposit on the conductive area of the substrate, a useful feature in various areas, such as the preparation of printed circuits [176]. Electroless deposition can be found in literature in a large number of metal/substrate combinations [177,178]. For example, metallization of semiconductor surfaces [179,180], deposition of Ag-Pd alloys [181,182], deposition of Pt on Ti surface [183], deposition of noble metals on Ge [184], Cu film formation on metal nitrides [185], Cu and Ni deposition on Al surfaces [186–189], metallization of carbon nanotubes [190] and deposition of Ag, Cu and Au surfaces [191,192] but in the particular case of Pd on Cu can be found a limited number of reports [171,176,193], where the authors did not study neither the homogeneity of the deposits over the entire substrate area nor their thickness or their adhesion and stability over time. Moreover, the combination of different electroless techniques to develop a complete process with tailorable Pd thickness has never been studied, to the best of my knowledge. In particular in its work Djokic [171] studied the influence of temperature and pH on the deposition rate of Pd-P alloys analysing their crystalline structure. Johnson [176] studied both the aging of the plating solution and the thickness of the obtained Pd layer, but due to the date of publish (1961) the thickness data obtained could be revised by more modern techniques. Ojani [194] studied the electroless deposition of Pt-Pd alloys as catalysts for HER (Hydrogen Evolution Reactions) reporting the composition and the surface morphology of the deposited alloys but without paying attention on the adhesion of the obtained structures.

In this work I attempted to combine two different palladium electroless processes on the way to deposit palladium films with tailored thickness on copper. To reach this aim, selected PDP baths were tested to obtain thin palladium films. Low thickness palladium films have the dual role of being applied as an affordable catalytic surface in the energy and automotive sector or protecting copper substrates from the subsequent PCP baths based on ammonia, which are the best performing palladium chemical plating baths available in literature to my knowledge [172,176]. Ammonia-based PCP baths used, exploited hypophosphite as reducing agent for the formation of the palladium coating. This type of formulation was the best alternative to the hydrazine-based PCP baths in terms of performance, although the palladium film could incorporate phosphorus forming Pd-P alloys [169,171]. Hydrazine represents the first type of reducing agent studied for the chemical deposition of different metals such as nickel, copper [195–197] and also palladium [198]. Hydrazine represents a less green and safe alternative to hypophosphite due to its hazardous properties such as flammability and toxicity [199].

4.2 Study of combined electroless techniques for palladium coatings with tailorable thickness

In this section will be presented the development of a combined technique based on different electroless deposition processes of palladium onto copper substrates. Ultra-thin palladium films were analysed from the thickness point of view applying an innovative method based on a standardless approach to overcome the limits of traditional methods (i.e., XRF or metallographic analysis of film sections). The strategy developed allowed to obtain palladium coatings free of surface defects in a wide range of thicknesses (from nano to microfilms).

4.2.1 Experimental

In this work three different PDP solutions were tested to study the displacement electroless deposition of palladium, both as a method to obtain nanometre-sized continuous layer and as a pre-deposition treatment applicable to PCP on the way to produce high-quality micrometre-sized palladium layers. These three different displacement deposition solutions from three different authors were selected as the sole alternatives available in literature.

All the solutions involved in this study were prepared with Ultrapure water (18.2 MΩ, TOC < 5 ppb) obtained by Sartorius Arium® mini system (Göttingen, Germany). The PDP solutions were prepared using different quantities of $PdCl_2$ salt 99.9% (Alfa Aesar, Heysham, Lancashire LA3 2XY, United Kingdom) and HCl 37% (VWR AnalaR® NORMAPUR®, Radnor, PA, USA). The PCP solution were obtained using the same $PdCl_2$ salt and

HCl purchased before for PDP solutions and were added NH_3 28% (VWR AnalaR® NORMAPUR®, Radnor, PA, USA), $NaH_2PO_2 \cdot H_2O$ (Carlo Erba, Cornaredo, Italy) and NH_4Cl (Merck Millipore Suprapur®, Burlington, MA, USA).

In Table 4.1 are reported the composition of PDP solutions studied.

Bath	**$PdCl_2$ (as Pd)**		**HCl (37%)**	
	mM	$g \cdot L^{-1}$	M	$mL \cdot L^{-1}$
A	9.4	1.66	0.6	50
B	28.2	5	2.6	216
C	0.56	0.1	0.006	0.5

Table 4.1 - Palladium displacement plating baths nomenclature and their relative composition.

Solutions A, B and C developed respectively by Djokić [171], Johnson [176] and Pearlstein [172] were prepared simply adding palladium salt in HCl solution, stirred until complete dissolution of the salt at room temperature.

The bath developed by Pearlstein and Weightman [172] (Table 4.2), was selected as the PCP solution used in this work due to its efficiency and its stability over time and work cycles.

Reagent	**Concentration**
$PdCl_2$	2 $g \cdot L^{-1}$
HCl (37%)	4 $mL \cdot L^{-1}$
NH_3 (28%)	160 $mL \cdot L^{-1}$
$NaH_2PO_2 \cdot H_2O$	10 $g \cdot L^{-1}$
NH_4Cl	27 $g \cdot L^{-1}$
Temperature	55°C
Deposition time	60 min.

Table 4.2 - Palladium chemical plating bath composition and conditions.

To obtain the best performances in terms of Pd film quality and bath stability, the PCP solution (presented in Table 4.2) preparation were carried out meticulously. The Pd solution was prepared by dissolving 0.1 g of $PdCl_2$ in a flask containing 0.2 mL of 37% HCl. Within it, palladium was presented in the form of $[PdCl_4]^{2-}$. To the previously prepared solution, was added 8 mL of 28% NH_3 little by little under stirring, forming a light-pink precipitate. The flask was closed and left under stirring for an hour until the solution became transparent. It was then left to mature for a total of 24 hours. Transparency indicated the formation of the chelate $[Pd(NH_3)_4]Cl_2$. The contents of the flask were subsequently filtered into a 25 mL flask with the use of a syringe and a glass fibre filter, to remove any pollutants which could lead to the deterioration of the solution. In parallel to this, a solution of sodium hypophosphite monohydrate was made by dissolving 0.5 g in 25 mL of Ultrapure water. Finally, the two solutions were combined in a 50 mL flask.

The copper substrates (pure copper, dimensions 50 mm x 10 mm x 1 mm) used in the entire work was pre-treated by different steps. The pre-treatment of copper substrates is an irreplaceable step due to the copper oxide layer naturally formed over the entire surface, which passivate it blocking the galvanic exchange reaction between copper atoms and palladium ions which produce the electroless deposited film.

First, the metallic slabs were polished with a polishing machine using a polishing soft brush and polishing wax. Then, to completely remove the organic residues due to the polishing wax, it was necessary to stir the copper plates inside toluene for about 3 minutes and rinse with abundantly Ultrapure water. Each copper plate was masked with the help of Teflon tape to obtain a reproducible deposition area (approximately 1 cm x 1 cm on the bottom of the plate) and further degreasing with acetone was performed. Second step, an electrochemical cathodic degreasing was then carried out using copper as cathode and a mixed oxide counter electrode inside an alkaline degreasing solution commercially available (DEXO 102, Italfimet, Arezzo, Italy). Copper plates were then, rinsed with Ultrapure water, dipped in a neutralization solution (H_2SO_4 0.5 M), and rinsed newly with Ultrapure water. The cathodic degreasing acts as a pre-treatment for copper surface as it removes copper oxide by the H_2 bubbling and organic residues by the soap in solution. All the Pd depositions were performed at 20 °C (except where differently stated). Both the beaker and the stir bar (when used) were carefully cleaned with a piranha solution and aqua regia after each single use.

Scanning electron microscope coupled with an energy dispersive X-ray spectroscopy detector (SEM-EDS) analysis was performed with Hitachi (Tokyo, Japan) S2300 using an acceleration voltage of 20 keV, equipped with Thermo-Fisher Scientific (Waltham, MA, USA) Noran System 7 detector and analysed with Pathfinder™ 1.3 software.

Equivalent metal film thickness determination by EDS spectra was made possible applying the K-ratio method [200,201]. Selecting a particular X-ray emission signal of an element (in this case Kα for copper and Lα for palladium) in the EDS spectra, the ratio between the area of this signal derived from the metal layer with a specific thickness and the one derived from the bulk metal is called K-ratio. In this case NIST DTSA-II software [202] was used to simulate EDS spectra of different palladium films with known thickness using Monte Carlo approach [200,201] applying the work parameters of the Hitachi SEM used for real samples. The calibration curve obtained from the simulated K-ratios *vs* standard metal film thickness was used to interpolate K-ratio values obtained from real palladium films with unknown thickness. The thickness values calculated by this method are "equivalent thicknesses" obtained by interpolating a regression curve.

Optical microscopy analysis (OM) was carried out with Nikon Eclipse L 150 (Tokyo, Japan) with images acquisition software NIS-Elements F 2.20.

X-ray fluorescence spectroscopy (XRF) of palladium films on copper was carried out using a Bowman BA-100 (Schaumburg, IL, USA) previously calibrated with Bowman certified palladium standard (0.99 μm) on bulk copper.

4.2.2 Results

Extensive bibliographic research and preliminary deposition tests were performed to verify the performances of deposition for both PDP and PCP solutions. Then the three PDP solutions presented in the previous section were selected to test which of them allow to obtain the best performances in terms of film thickness and morphology. Each solution was tested combining different deposition time and the presence or the absence of stirring. The list of performed tests is reported in Table 4.3.

Sample	PDP solution	stirring	Deposition time (s)
#1	A	No	30
#2	A	No	90
#3	C	No	30
#4	C	No	90
#5	B	No	30
#6	B	No	90
#7	A	Yes	30
#8	A	Yes	90
#9	C	Yes	30
#10	C	Yes	90
#11	B	Yes	30
#12	B	Yes	90

Table 4.3 - Deposition conditions for PDP samples obtained from baths A, B and C.

The deposition parameters selected to produce samples from #1 to #12 were chosen to compare the performances of the PDP solution in presence and in absence of stirring, combining two deposition times. The shorter deposition times respect to those already studied in literature (12 minutes in the case of Johnson's work [176]) were selected in order to study the possibility to obtain an ultrathin-but-continuous palladium layer, to persecute the sustainability in terms of precious metal amount, which is the one of the main aims at the basis of this work.

Once the depositions were completed (Figure 4.2), the plates thus obtained were rinsed abundantly with Ultrapure water and dried under nitrogen flow. To address the film quality and thickness, the deposits obtained were analysed through various techniques with OM, SEM-EDS and XRF.

Figure 4.2 - Aesthetic appearance of palladium films obtained by displacement plating. Sample numbers are reported on the uncoated part of each sample.

4.2.2.1 Palladium displacement plating characterization

Due to the very low amount of palladium deposited with the PDP method, SEM-EDS analysis was used to measure the film thickness. The EDS spectra of the specimens made of copper with various thickness palladium were simulated with NIST DTSA-II software. From the spectra the K-ratio were calculated to build the calibration curve (Figure 4.3) [200,201]. K-ratios are defined as the ratio between the peak intensity (X-ray counts) for the element of interest in the sample and the peak intensity of the pure element at the same energy. Then the spectra of real samples were recorded, the K-ratio was calculated, and the thickness obtained by means the calibration curve.

The calibration curve for the thickness determination was built simulating the following thicknesses of palladium on copper: 0 nm, 5 nm, 10 nm, 20 nm, 50 nm, 75 nm (Figure 4.3 inset). The simulated points were not equally spaced because the correlation between thickness and K-ratio is exponential, in this way the fitting is more reliable and optimized, keeping the number of points low. For low metal thicknesses the correlation between K-ratio and thickness values can be approximated by a second-grade equation which provide a simpler regression maintaining a high reliability ($R^2 > 0.999$).

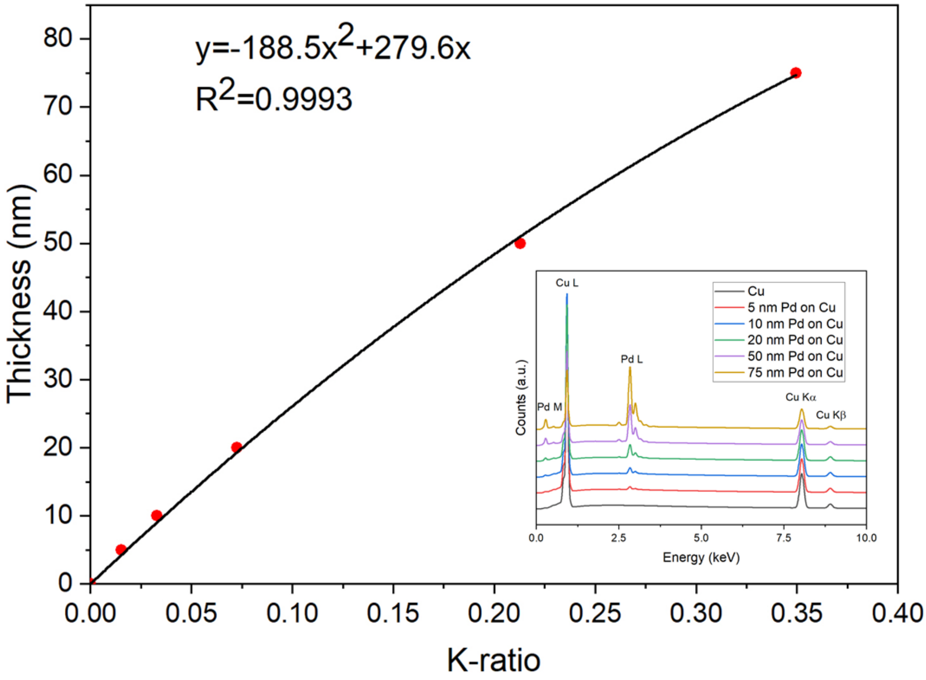

Figure 4.3 - Fitting curve of simulated standard palladium film thicknesses and relative K-ratio. In figure are reported the fitting equation and the R^2 value of the fitting equation. The inset shows the simulated spectra used to obtain the K-ratios.

The thicknesses obtained with the K-ratios through the calibration curve are reported in Table 4.4. The standard deviation was calculated from the values provided by the EDS spectra.

Sample	K-ratio	EDS thickness (nm)	Std. Dev. (± nm)
#1	0.006	1.7	0.3
#2	0.015	4.2	0.3
#3	0.000	0	/
#4	0.003	0.8	0.3
#5	0.039	10.6	0.3
#6	0.084	22.2	0.2
#7	0.010	2.8	0.3
#8	0.034	9.3	0.3
#9	0.004	1.1	0.3
#10	0.022	6.1	0.3
#11	0.070	18.6	0.2
#12	0.168	41.7	0.4

Table 4.4 - Equivalent thickness results by EDS spectra of palladium displacement plating samples.

From the results obtained, comparing the same deposition solution, the increase of deposition time seemed to act in a more relevant way than the presence or the absence of stirring on the obtained thickness. Although also the presence of stirring contributed to increase the Pd thickness, guaranteeing a constant concentration of Pd ions at the substrate-solution interface. EDS analysis do not detect the presence of Pd in sample #3. For this reason, in Table 4.4 the K-ratio and the thickness values are 0.

OM was used to verify the absence or presence of discontinuities and defects due to an uncomplete coverage of the copper substrate. Samples #6, #8 and, #10 were observed by optical microscopy. These three samples were selected because they were the best results obtained from each deposition solution (A, B and C) in terms of macroscopical homogeneity and palladium thickness measured by K-ratio method. OM images of sample #6, #8 and #10 are reported in Figure 4.4.

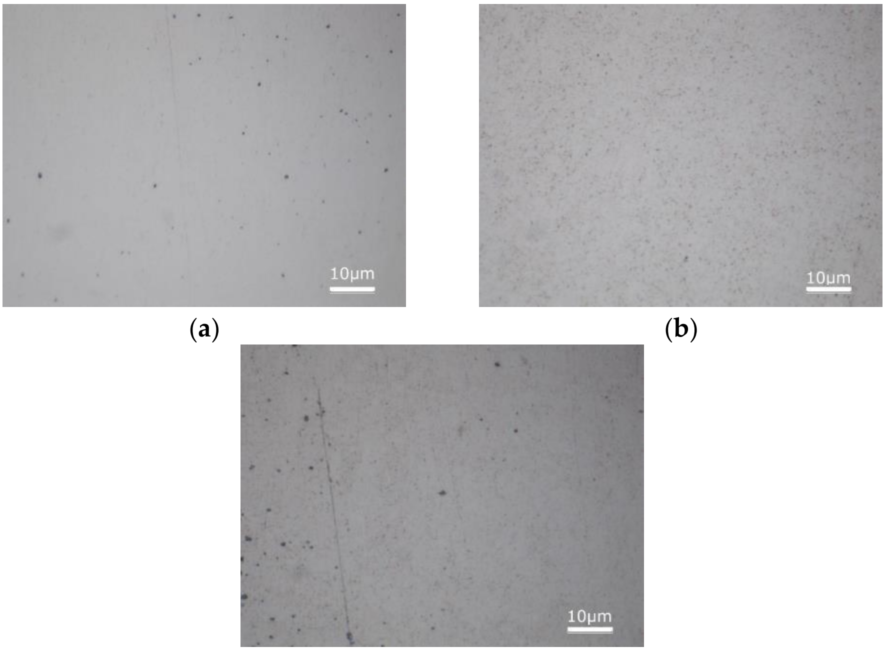

(**a**) (**b**)

(**c**)

Figure 4.4 - Optical microscopy images of samples (a) #6; (b) #8 and (c) #10 after palladium displacement deposition.

Comparing the three different samples from optical microscopy point of view, the surfaces resulted sufficiently homogeneous and compact as could be thought observing the samples with the naked eye. The presence of small bumps and scratches was attributed to the imperfections present on the copper substrate and not to the palladium deposition. Sample #6 represents the best result obtained using the PDP bath B, described by Johnson [176]; in the present work were used the same composition and the best conditions discovered by Johnson during his work (25°C, 250 mL/L HCl 32% = 216 mL/L HCl 37%, Pd 5 g/L) except for the deposition time, which was 12 minutes for Johnson and 90 seconds in the present work. Using its working conditions Johnson declared to obtain shiny Pd films of 70 μin (1.778 μm) without exfoliations (average deposition rate = 148 nm/min). In the present work I obtained a Pd deposit of 22.2 nm in 90 seconds (average deposition rate = 14.8 nm/min). The discrepancy between the two deposition rates could be explained considering the autocatalytic effect that Pd film has towards its deposition that could change the rates during the early minutes of deposition. Sample #8 was the best result in terms of surface defects obtained from the PDP solution A, developed by Djokic [171], though it cannot be compared with the results obtained by this author because he used the PDP bath only as a surface pre-treatment without paying attention on results derived from the displacement plating and the thickness of the film formed.

Sample #10 obtained from the PDP solution C, used by Pearlstein ad Weightman [172] represented the sample with the minor amount of palladium deposited beside the three best samples selected in the present work due to the low concentration of metal precursor in solution. Pearlstein used this PDP solution as a pre-treatment of the metal substrate without studying this treatment in dept. As in the case of Djokic work a comparison with the results obtained in the present work is not possible.

Sample #12, although showing a much higher palladium thickness than sample #6 (both obtained from deposition solution B), after 7 days showed a wide exfoliation of palladium film which was addressed to the poor adhesion of the film ascribed to the excess of residual internal stress [203]. During their formation, thin films can develop large intrinsic stresses [204,205]. These stresses can have a magnitude which exceeds that of the same bulk material. The residual internal stresses developed by thin films relax forming blisters or exfoliations (as in the case of PDP sample #12, Figure 4.5) in different time scales which goes from hours to days. For this reason, were selected 7 days as an acceptable time scale to monitoring the eventual relaxation of stresses developed by Pd films during deposition.

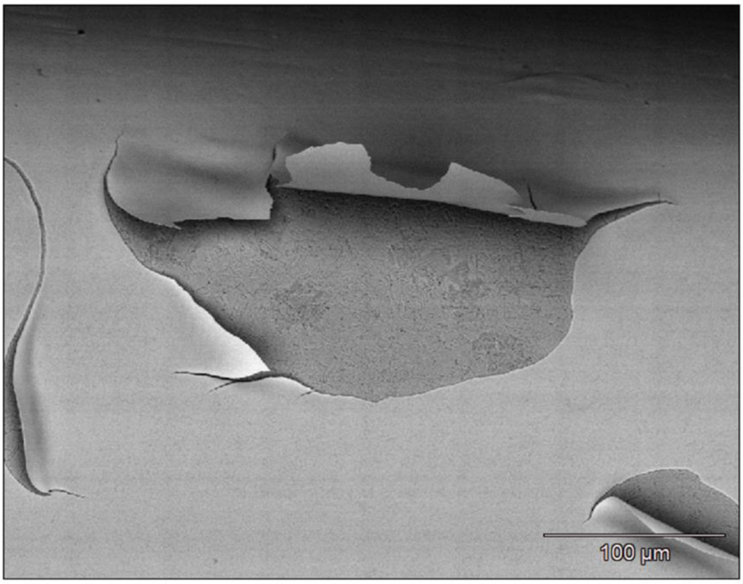

Figure 4.5 - Exfoliation occurred on sample #12 observed by SEM in backscattered electrons mode.

4.2.2.2 Palladium chemical plating characterization

To obtain an adherent deposited layer, is not sufficient that the copper substrate to be cleaned but it should also be not damaged by the PCP. The same PDP procedures followed for samples #6, #8 and #10, were applied as pre-deposition for PCP (obtaining the samples #6C, #8C and #10C respectively) to evaluate which one was the most protective one towards Cu base material, since copper is severely attacked by the high concentration of ammonia present in PCP solution. Beside that the effectiveness of PCP is valuable for application in which deposits in the micron range are requested. Each PDP pre-deposition were carried out immediately before PCP. The PCP depositions were performed without stirring, at a temperature of 55°C and for a duration of 60 minutes. In Figure 4.6 it is possible to observe the samples 7 days after the deposition. The copper substrate, which was not covered with a protective PDP, despite the facts that it was not immersed in the solution, was strongly corroded by the ammonia vapours. In the bottom part of the samples, where the pre-deposition was carried out, a homogeneous and shiny palladium deposit is visible. After one week, sample #6C underwent to a strong exfoliation, while the other two samples appeared intact to the naked eye. As can be seen from Figure 4.6, PCP sample #6C showed the copper substrate under the palladium exfoliation. The hypothesis on the failure of this sample regarded the poor stability of the PDP pre-deposition performed on this sample. As already observed for PDP sample #12, the relaxation of residual internal stresses developed by Pd thin film on copper was the origin of the detachment of the PDP+PCP palladium coating on sample #6C, occurred in a time range longer than the 7 days during which the PDP pre-deposition were monitored.

Figure 4.6 - Palladium chemical plating samples after 7 days of aging. Sample number is reported on the uncoated part of each sample (from left to right sample #6C, #8C, #10C).

The deposits obtained were analysed by XRF [101,206], the total palladium film thicknesses obtained summing PDP+PCP processes are shown in Table 4.5. The average values and the standard deviations were the result of three measurements carried out in different spots randomly chosen.

Sample	Average thickness (µm)	Std. Dev. (± µm)
#6C	1.59	0.16
#8C	1.69	0.18
#10C	1.78	0.06

Table 4.5 - XRF thickness determination of palladium coatings. In the second column are reported the thicknesses of the palladium coatings derived from PDP+PCP procedure.

In Figure 4.7 it is possible to appreciate the deposits analysed under OM, 7 days later the deposition processes. The deposit #10C was the most homogeneous, free of defects and even the thickest, while sample #6C presented extended exfoliations which brought to light the characteristic colour of the copper substrate and sample #8 showed cracks.

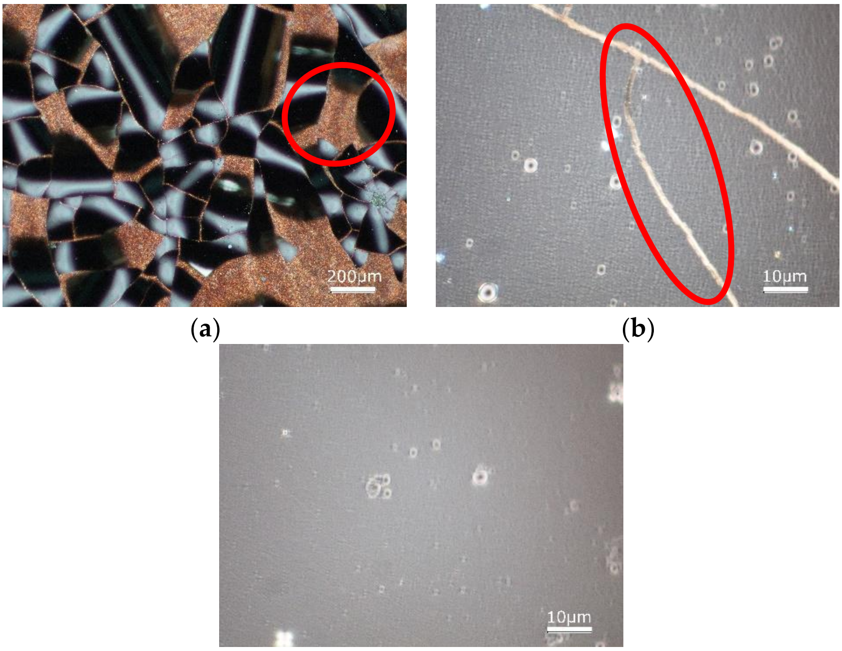

(a) (b)

(c)

Figure 4.7 - In figure are reported OM images of sample (a) #6C; (b) #8C and (c) #10C. For samples #6C and #8C can be observed the presence of cracks (e.g., the features highlighted by the red circles) while for sample #10C the surface results smooth and free of defects.

Sample #10C, obtained by the combined process of PDP + PCP applying the PDP and PCP solutions already exploited by Pearlstein and Weightman [172] showed the best results in terms of Pd film adhesion, homogeneity and absence of surface defects (cracks, blisters or exfoliations). In Pearlstein and Weightman work, the authors stated a deposition rate of over 2.5 μm/hr for the PCP on copper. In the present work applying the same conditions of the afore mentioned work, I obtained a growth of 1.78 μm of Pd in 1 hour. The discrepancy between the two values can be due to two main factors. In the Pearlstein's work the PDP pre-treatment is longer and is anticipated by another pre-treatment based on a tin electroless bath, which alters the catalytic activity of the surface on the oxidation of hypophosphite in the PCP bath. Second, the thickness determination method used in the present work for the PDP+PCP samples (X-Ray Spectroscopy) is more accurate than the gravimetric method applied by Pearlstein and co-worker being and indirect gravimetric determination.

4.2.3 Final remarks and outlooks

In conclusion, two different but combinable type of electroless deposition techniques were tested to obtain palladium films without cracks, exfoliations, or blisters on copper substrate. Applying palladium displacement deposition, I obtained some very thin metal films with equivalent thickness ranging from 6.1 to 22.2 nm measured with SEM-EDS K-ratio method. Moreover, the possibility to plate only the metallic surface of the substrate, which is the main feature of electroless plating based on galvanic displacement represent an interesting option in fuel cell electrodes fabrication with novel geometries in which palladium surface contours must be finely tuned.

Palladium films obtained by displacement plating on copper were used as protective undercoat to perform palladium chemical plating from an ammonia-based bath which otherwise could not be applied due the corrosive behaviour of ammonia for copper substrates. A high-quality palladium film with thickness of 1.78 μm (sample #10C) was obtained applying the combined procedure I studied using the Pearlstein and Weightman pre-deposition (solution C). This result is proof of the integrity of palladium coat obtained by displacement plating and represents a valuable alternative for applications where thick palladium films on copper are requested. The combination of PDP+PCP studied in the present part of my *Ph.D.* thesis could represent a valuable alternative to the palladium electroplating in jewellery and luxury goods industries where this metal is widespread as intermediate layer or topcoat. Palladium electroless plating is a valid alternative to electroplating thanks to the lower investment required for industrial plants and the electricity savings required for the process.

Future developments will regard the refine of the control of Pd thickness both in single and in combined techniques mode. Moreover, the Pd film needs to be characterized more in deep from the mechanical and compositional point of view based of specific areas of application to which it will be destined.

5 Conclusions

The first part of the *Ph.D.* thesis regarded the development of a cyanide-free bronze plating bath based on methanesulfonic acid as the electrolyte, which is considered environmental-friendly. Bronze plating baths developed were studied applying cyclic voltammetry to state the effect of the organic additive selected and to select the adequate deposition potentials to obtain a copper-tin alloy with a controlled ratio of the two metals. The aging of the six different deposition solutions produced was tested to select the most stable. The two most stable formulations were selected to produce bronze coatings using potentiostatic and galvanostatic deposition techniques. The morphology and the composition of the films were studied both in plan-view and in cross-section exploiting SEM-EDS. Moreover, the crystal structure of the films was studied by XRD. Utilizing the solution with a Cu:Sn molar ratio of 1:1 and a deposition potential of -0.55 V, EDS and XRD data confirmed the formation of a η' single-phase bronze with a Cu:Sn composition ≈ 2:1. Moreover, the SEM cross-section analyses showed a relatively uniform composition of this film. The elemental composition and the crystal structure of the films with deposition conditions of samples S4B made this electrodeposition approach a promising candidate for the synthesis of kesterite compounds which represent the final goal of this research.

A copper plating bath was derived from the bronze plating one, to study the effect of a brightening agent on the nucleation and growth mechanism of the metal film on the way to tailor the copper film structure. I explored the possibility to understand if an organic additive could have a relevant effect on the morphology of an electrodeposited film (e.g., brightener, leveler, suppressor, etc.) exploiting an "a priori" kinetic study instead of only morphological analysis on the metal coating. Exploiting cyclic voltammetry to study the effect of thiourea at three different concentrations (30, 60, 90 ppm) on the electrochemical behavior of copper ions in solution, three different copper deposition potentials were selected. Applying the different deposition potentials chronoamperometric studies were exploited to state if the copper film formation mechanism followed instantaneous or progressive nucleation and growth, varying the concentration of organic additive and deposition conditions. To analyze chronoamperometric data the Scharifker-Hills theoretical model was applied. Moreover, electrodeposited copper films were produced to compare kinetic data with real samples characterization. I found that increasing thiourea concentration the film formation mechanism approached the progressive one. The samples characterization reported that a good agreement between kinetic data and copper film characteristics was found up to 60 ppm of thiourea added. The highest organic additive concentration (90 ppm) resulted in an uncontrolled copper growth due to parasitic adsorption reactions of thiourea, not detectable by the kinetic study. I verified that kinetic analysis on the nucleation and growth path of a metal film could be a valuable way to discriminate the effect of an organic additive on the formation of metal coatings, and that thiourea resulted a valuable compound to control copper ions reduction on the way to improve the structure of bronze films and thus finally to obtain kesterite compounds.

The second part of the *Ph.D.* thesis regarded the study of new electrochemical pathways to develop catalytic surfaces based on both non-PGM and PGM. As non-PGM catalysts, was studied the enrichment with cobalt and copper of raw chars derived from the microwave-assisted pyrolysis of waste tyres. Two distinct enrichment paths were tested: sonochemical deposition of cobalt and copper, and electrochemical deposition of cobalt. Various samples were produced applying different deposition conditions. Each sample was studied from the electrocatalytic activity for ORR point of view. The enrichment process based on the electrodeposition of cobalt resulted the best one, being able to produce catalytic chars with an oxygen conversion to water up to 99% and very good stability over work cycles.

As PGM potential catalytic surface were studied electroless deposited palladium thin films on copper. Palladium films were produced applying to distinct electroless deposition techniques: displacement plating and chemical plating. The first one, being a self-limited reaction allowed to obtain palladium coatings in nanometers range whose thickness were studied exploiting the K-ratio method, based on the EDS signals detected during SEM-EDS analysis. Along this process, I obtained continuous palladium layers, free of defects, in the range from 6 to 20 nm. Nanometered palladium films obtained by displacement plating were also used as pre-treatment coatings to test a chemical plating bath. The palladium chemical plating bath studied was not suitable for the direct deposition on copper due to the presence of ammonia which could damage the substrate. Pre-treated samples were plated using the chemical plating bath obtaining a palladium coating without surface defects and thickness over 1.5 μm. This combined process could also be a sustainable alternative to electrodeposited palladium for the fashion industry.

Acknowledgments

Prof. Giovanni Zangari and Dr. Yunkai Sun (Department of Materials Science and Engineering, University of Virginia) are acknowledged for the useful discussion regarding structural and compositional data of Section 1.

Dr. Leonardo Lari and Dr. Vlado K. Lazarov (University of York and York-JEOL Nanocentre) are acknowledged for the morphological and compositional characterization of char samples in Section 3.

Prof. Claudio Fontanesi (Department of Engineering "Enzo Ferrari", University of Modena and Reggio Emilia) is acknowledged for the fruitful discussions regarding kinetic data in Section 2 and morphological results in Section 4.

LEM s.r.l. Socio Unico and the Laboratory of Applied Electrochemistry of the University of Florence are acknowledged for the technical, scientific, and human support over the entire *Ph.D.* work.

References

1. Survila, A.; Mockus, Z.; Kanapeckaitė, S.; Jasulaitienė, V.; Juškėnas, R. Codeposition of copper and tin from acid sulphate solutions containing polyether sintanol DS-10 and micromolar amounts of halides. *Electrochim. Acta* **2007**, *52*, 3067–3074, doi:10.1016/j.electacta.2006.09.040.
2. Survila, A.; Mockus, Z.; Kanapeckaitė, S.; Jasulaitienė, V.; Juškėnas, R. Codeposition of copper and tin from acid sulphate solutions containing polyether sintanol DS-10 and benzaldehyde. *J. Appl. Electrochem.* **2009**, *39*, 2021–2026, doi:10.1007/s10800-009-9914-2.
3. Survila, A.; Mockus, Z.; Kanapeckaitė, S.; Jasulaitienė, V.; Juškėnas, R. Codeposition of copper and tin from acid sulphate solutions containing gluconic acid. *J. Electroanal. Chem.* **2010**, *647*, 123–127, doi:https://doi.org/10.1016/j.jelechem.2010.06.015.
4. Barbano, E.P.; de Oliveira, G.M.; de Carvalho, M.F.; Carlos, I.A. Copper–tin electrodeposition from an acid solution containing EDTA added. *Surf. Coatings Technol.* **2014**, *240*, 14–22, doi:https://doi.org/10.1016/j.surfcoat.2013.12.005.
5. Correia, A.N.; Façanha, M.X.; de Lima-Neto, P. Cu–Sn coatings obtained from pyrophosphate-based electrolytes. *Surf. Coatings Technol.* **2007**, *201*, 7216–7221, doi:10.1016/j.surfcoat.2007.01.029.
6. Kasach, A.A.; Kharitonov, D.S.; Romanovskii, V.I.; Kuz'menok, N.M.; Zharskii, I.M.; Kurilo, I.I. Electrodeposition of Cu-Sn Alloy from Oxalic Acid Electrolyte in the Presence of Amine-containing Surfactants. *Russ. J. Appl. Chem.* **2019**, *92*, 835–841,

doi:10.1134/S1070427219060144.

7. Bengoa, L.N.; Tuckart, W.R.; Zabala, N.; Prieto, G.; Egli, W.A. Bronze electrodeposition from an acidic non-cyanide high efficiency electrolyte: Tribological behavior. *Surf. Coatings Technol.* **2014**, *253*, 241–248, doi:10.1016/j.surfcoat.2014.05.046.

8. Finazzi, G.A.; de Oliveira, E.M.; Carlos, I.A. Development of a sorbitol alkaline Cu–Sn plating bath and chemical, physical and morphological characterization of Cu–Sn films. *Surf. Coatings Technol.* **2004**, *187*, 377–387, doi:10.1016/j.surfcoat.2004.01.029.

9. D. Gernon, M.; Wu, M.; Buszta, T.; Janney, P. Environmental benefits of methanesulfonic acid . Comparative properties and advantages. *Green Chem.* **1999**, *1*, 127–140, doi:10.1039/A900157C.

10. Bengoa, L.N.; Pary, P.; Conconi, M.S.; Egli, W.A. Electrodeposition of Cu-Sn alloys from a methanesulfonic acid electrolyte containing benzyl alcohol. *Electrochim. Acta* **2017**, *256*, 211–219, doi:10.1016/j.electacta.2017.10.027.

11. Pewnim, N.; Roy, S. Electrodeposition of tin-rich Cu–Sn alloys from a methanesulfonic acid electrolyte. *Electrochim. Acta* **2013**, *90*, 498–506, doi:https://doi.org/10.1016/j.electacta.2012.12.053.

12. Low, C.T.J.; Walsh, F.C. Normal and anomalous electrodeposition of tin–copper alloys from methanesulphonic acid bath containing perfluorinated cationic surfactant. *Trans. IMF* **2008**, *86*, 315–325, doi:10.1179/174591908X304180.

13. Low, C.T.J.; Walsh, F.C. Electrodeposition of tin, copper and tin–copper alloys from a methanesulfonic acid electrolyte containing a perfluorinated cationic surfactant. *Surf. Coatings Technol.* **2008**, *202*,

1339–1349, doi:10.1016/j.surfcoat.2007.06.032.

14. Low, C.T.J.; Walsh, F.C. The stability of an acidic tin methanesulfonate electrolyte in the presence of a hydroquinone antioxidant. *Electrochim. Acta* **2008**, *53*, 5280–5286, doi:10.1016/j.electacta.2008.01.093.

15. Egli, A.; Chen, Q. Electroplating Bronze 2010, *2*, 3–8.

16. Weitershaus, K.; Zhang-Beglinger, W.; Guebey, J. Adhesion promotion of cyanide free white bronze 2015, 15.

17. Foyet, A.; Guebey, J.; Clauss, M. Cyanide-Free Electroplating Baths For White Bronze Based On Copper (I) Ions 2016, 21.

18. Foyet, A.; Guebey, J.; Clauss, M. Cyande-Free Electroplating Baths For White Bronze Based On Copper (I) Ions 2016, 13.

19. Beattie, S.D.; Dahn, J.R. Single Bath, Pulsed Electrodeposition of Copper-Tin Alloy Negative Electrodes for Lithium-ion Batteries. *J. Electrochem. Soc.* **2003**, *150*, A894, doi:10.1149/1.1577336.

20. Zanella, C.; Xing, S.; Deflorian, F. Effect of electrodeposition parameters on chemical and morphological characteristics of Cu–Sn coatings from a methanesulfonic acid electrolyte. *Surf. Coatings Technol.* **2013**, *236*, 394–399, doi:https://doi.org/10.1016/j.surfcoat.2013.10.020.

21. Berretti, E.; Calisi, N.; Capaccioli, A.; Capozzoli, L.; Hamouda, A.M.S.; Giaccherini, A.; Giurlani, W.; Ienco, A.; Martinuzzi, S.; Innocenti, M.; et al. Electrodeposited white bronzes on brass: Corrosion in 3.5 % sodium chloride solution. *Corros. Sci.* **2020**, *175*, 108898, doi:10.1016/j.corsci.2020.108898.

22. Rosley, R.; Jikan, S.S.; Badrulzaman, N.A.; Razak, S.N.A.; Roslan, M.S.

Effect of Different Complexing Agent on Surface Morphology and Microstructure of Cu-Sn-Zn Coatings Electrodeposited From Less Hazardous Electrolyte. *J. Phys. Conf. Ser.* **2020**, *1529*, 042004, doi:10.1088/1742-6596/1529/4/042004.

23. JÄGER-WALDAU, A. *PV Status Report 2019*; 2019;

24. Wolden, C.A.; Kurtin, J.; Baxter, J.B.; Repins, I.; Shaheen, S.E.; Torvik, J.T.; Rockett, A.A.; Fthenakis, V.M.; Aydil, E.S. Photovoltaic manufacturing: Present status, future prospects, and research needs. *J. Vac. Sci. Technol. A Vacuum, Surfaces, Film.* **2011**, *29*, 30801, doi:10.1116/1.3569757.

25. Zakery, A.; Elliott, S.R. Optical properties and applications of chalcogenide glasses: a review. *J. Non. Cryst. Solids* **2003**, *330*, 1–12.

26. Sugimoto, H.; Yagioka, T.; Nagahashi, M.; Yasaki, Y.; Kawaguchi, Y.; Morimoto, T.; Chiba, Y.; Aramoto, T.; Tanaka, Y.; Hakuma, H. Achievement of over 17% efficiency with 30× 30cm 2-sized Cu (InGa)(SeS) 2 submodules. In Proceedings of the 2011 37th IEEE Photovoltaic Specialists Conference; IEEE, 2011; pp. 3420–3423.

27. Green, M.A.; Hishikawa, Y.; Dunlop, E.D.; Levi, D.H.; Hohl-Ebinger, J.; Yoshita, M.; Ho-Baillie, A.W.Y. Solar cell efficiency tables (Version 53). *Prog. Photovoltaics Res. Appl.* **2019**, *27*, 3–12, doi:10.1002/pip.3102.

28. Peter, L.M. Towards sustainable photovoltaics: the search for new materials. *Philos. Trans. R. Soc. A Math. Phys. Eng. Sci.* **2011**, *369*, 1840–1856.

29. Mitzi, D.B.; Gunawan, O.; Todorov, T.K.; Barkhouse, D.A.R. Prospects and performance limitations for Cu–Zn–Sn–S–Se photovoltaic technology. *Philos. Trans. R. Soc. A Math. Phys. Eng. Sci.*

2013, *371*, 20110432.

30. Mitzi, D.B.; Gunawan, O.; Todorov, T.K.; Wang, K.; Guha, S. The path towards a high-performance solution-processed kesterite solar cell. *Sol. Energy Mater. Sol. Cells* **2011**, *95*, 1421–1436, doi:10.1016/j.solmat.2010.11.028.

31. Kumar, M.; Dubey, A.; Adhikari, N.; Venkatesan, S.; Qiao, Q. Strategic review of secondary phases, defects and defect-complexes in kesterite CZTS–Se solar cells. *Energy Environ. Sci.* **2015**, *8*, 3134–3159, doi:10.1039/C5EE02153G.

32. Chen, S.; Walsh, A.; Gong, X.; Wei, S. Classification of lattice defects in the kesterite Cu2ZnSnS4 and Cu2ZnSnSe4 earth-abundant solar cell absorbers. *Adv. Mater.* **2013**, *25*, 1522–1539.

33. Guo, Q.; Ford, G.M.; Yang, W.-C.; Walker, B.C.; Stach, E.A.; Hillhouse, H.W.; Agrawal, R. Fabrication of 7.2% Efficient CZTSSe Solar Cells Using CZTS Nanocrystals. *J. Am. Chem. Soc.* **2010**, *132*, 17384–17386, doi:10.1021/ja108427b.

34. Wang, W.; Winkler, M.T.; Gunawan, O.; Gokmen, T.; Todorov, T.K.; Zhu, Y.; Mitzi, D.B. Device Characteristics of CZTSSe Thin-Film Solar Cells with 12.6% Efficiency. *Adv. Energy Mater.* **2014**, *4*, 1301465, doi:10.1002/aenm.201301465.

35. Giurlani, W.; Zangari, G.; Gambinossi, F.; Passaponti, M.; Salvietti, E.; Di Benedetto, F.; Caporali, S.; Innocenti, M. Electroplating for Decorative Applications: Recent Trends in Research and Development. *Coatings* **2018**, *8*, 260.

36. Yan, C.; Sun, K.; Liu, F.; Huang, J.; Zhou, F.; Hao, X. Boost Voc of pure sulfide kesterite solar cell via a double CZTS layer stacks. *Sol.*

Energy Mater. Sol. Cells **2017**, *160*, 7–11, doi:https://doi.org/10.1016/j.solmat.2016.09.027.

37. Unveroglu, B.; Zangari, G. Towards phase pure kesterite CZTS films via Cu-Zn-Sn electrodeposition followed by sulfurization. *Electrochim. Acta* **2016**, *219*, 664–672, doi:https://doi.org/10.1016/j.electacta.2016.10.079.

38. Unveroglu, B.; Zangari, G. Effect of cell configuration on the compositional homogeneity of electrodeposited Cu-Zn-Sn alloys and phase purity of the resulting Cu2ZnSnS4 absorber layers. *Electrochim. Acta* **2017**, *255*, 347–357, doi:https://doi.org/10.1016/j.electacta.2017.08.155.

39. Brenner, A. Electrodeposition of copper-tin alloys. In *Electrodeposition of Alloys*; 1963; p. 734 ISBN 9781483223117.

40. Drissi-Daoudi, R.; Irhzo, A.; Darchen, A. Electrochemical investigations of copper behaviour in different cupric complex solutions: Voltammetric study. *J. Appl. Electrochem.* **2003**, *33*, 339–343, doi:10.1023/A:1024191404595.

41. elc ALR3002M bench power supply Available online: http://elc.fr/media/alr3002m_gb__091028600_1458_23062014.pdf.

42. Saunders, N.; Miodownik, A.P. The Cu-Sn (copper-tin) system. *Bull. Alloy Phase Diagrams* **1990**, *11*, 278–287.

43. Fürtauer, S.; Li, D.; Cupid, D.; Flandorfer, H. The Cu–Sn phase diagram, Part I: new experimental results. *Intermetallics* **2013**, *34*, 142–147.

44. CrystalMaker Software Ltd, Oxford, E. Generated using

CrystalDiffract®: a powder diffraction program for Mac and Windows Available online: www.crystalmaker.com.

45. CrystalMaker Software Ltd, Oxford, E. Images and video generated using CrystalMaker®: a crystal and molecular structures program for Mac and Windows Available online: www.crystalmaker.com.

46. Allmann, R.; Hinek, R. The introduction of structure types into the Inorganic Crystal Structure Database ICSD. *Acta Crystallogr. Sect. A Found. Crystallogr.* **2007**, *63*, 412–417.

47. R. M. Krishnan; Muralidharan, V.S. Electrochemical behaviour of Cu-NTA complexes. *Proc. Indian Acad. Sci. - Chem. Sci.* **1991**, *103*, 107–118, doi:10.1007/BF02843560.

48. Oztekin, Y.; Yazicigil, Z. Recovery of metals from complexed solutions by electrodeposition. *Desalination* **2006**, *190*, 79–88.

49. Anderegg, G. Critical survey of stability constants of NTA complexes. *Pure Appl. Chem.* **1982**, *54*, 2693–2758.

50. Suzuki, K.; Yasuda, M.; Yamasaki, K. Stability Constants of Picolinic and Quinaldic Acid Chelates of Bivalent Metals. *J. Phys. Chem.* **1957**, *61*, 229–231.

51. Portela, A.L.; Teijelo, M.L.; Lacconi, G.I. Mechanism of copper electrodeposition in the presence of picolinic acid. *Electrochim. Acta* **2006**, *51*, 3261–3268, doi:10.1016/j.electacta.2005.09.029.

52. Gamburg, Y.D.; Zangari, G. *Theory and Practice of Metal Electrodeposition*; Springer New York: New York, NY, 2011; ISBN 978-1-4419-9668-8.

53. Zech, N. Anomalous Codeposition of Iron Group Metals: I. Experimental Results. *J. Electrochem. Soc.* **1999**, *146*, 2886,

doi:10.1149/1.1392024.

54. Liu, X.J.; Kainuma, R.; Wang, C.P.; Ohnuma, I.; Ishida, K. Experimental investigation and thermodynamic calculation of the phase equilibria in the Cu-Sn and Cu-Sn-Mn systems. *Metall. Mater. Trans. A* **2004**, *35*, 1641–1654, doi:10.1007/s11661-004-0073-0.

55. Shim, J.H.; Oh, C.-S.S.; Lee, B.J.; Lee, D.N. Thermodynamic assessment of the Cu-Sn system. *Z Met.* **1996**, *87*, 205–212.

56. Kroupa, A.; Vizdal, J. The thermodynamic database for the development of modern lead-free solders. In Proceedings of the Defect and Diffusion Forum; Trans Tech Publ, 2007; Vol. 263, pp. 99–104.

57. Gierlotka, W.; Chen, S.; Lin, S. Thermodynamic description of the Cu–Sn system. *J. Mater. Res.* **2007**, *22*, 3158–3165, doi:10.1557/JMR.2007.0396.

58. Li, M.; Du, Z.; Guo, C.; Li, C. Thermodynamic optimization of the Cu–Sn and Cu–Nb–Sn systems. *J. Alloys Compd.* **2009**, *477*, 104–117, doi:https://doi.org/10.1016/j.jallcom.2008.09.141.

59. Li, D.; Franke, P.; Fürtauer, S.; Cupid, D.; Flandorfer, H. The Cu–Sn phase diagram part II: New thermodynamic assessment. *Intermetallics* **2013**, *34*, 148–158, doi:https://doi.org/10.1016/j.intermet.2012.10.010.

60. Juškėnas, R.; Mockus, Z.; Kanapeckaitė, S.; Stalnionis, G.; Survila, A. XRD studies of the phase composition of the electrodeposited copper-rich Cu–Sn alloys. *Electrochim. Acta* **2006**, *52*, 928–935, doi:https://doi.org/10.1016/j.electacta.2006.06.029.

61. Cavallotti, P.L.; Nobili, L.; Vicenzo, A. Phase structure of electrodeposited alloys. *Electrochim. Acta* **2005**, *50*, 4557–4565, doi:https://doi.org/10.1016/j.electacta.2005.03.060.

62. Beattie, S.D.; Dahn, J.R. Single-Bath Electrodeposition of a Combinatorial Library of Binary Cu1 − x Sn x Alloys. *J. Electrochem. Soc.* **2003**, *150*, C457–C460, doi:10.1149/1.1576769.

63. Fedotev, N.P.; Vyacheslavov, P.M. Phase structure of binary alloys produced by electrodeposition. *Plating* **1970**, *57*, 700–706.

64. Hubbell, J.H.; Seltzer, S.M. *Tables of X-ray mass attenuation coefficients and mass energy-absorption coefficients 1 keV to 20 MeV for elements Z= 1 to 92 and 48 additional substances of dosimetric interest*; National Inst. of Standards and Technology-PL, Gaithersburg, MD (United …, 1995;

65. Alex, S.; Chattopadhyay, K.; Basu, B. Tailored specular reflectance properties of bulk Cu based novel intermetallic alloys. *Sol. Energy Mater. Sol. Cells* **2016**, *149*, 66–74, doi:https://doi.org/10.1016/j.solmat.2016.01.002.

66. Alex, S.; Basu, B.; Sengupta, S.; Pandey, U.K.; Chattopadhyay, K. Electrodeposition of δ-phase based Cu–Sn mirror alloy from sulfate-aqueous electrolyte for solar reflector application. *Appl. Therm. Eng.* **2016**, *109*, 1003–1010, doi:https://doi.org/10.1016/j.applthermaleng.2016.04.104.

67. Soffa, W.A.; Laughlin, D.E. Diffusional phase transformations in the solid state. In *Physical Metallurgy*; Elsevier, 2014; pp. 851–1020.

68. Cai, W.; Nix, W.D. *Imperfections in crystalline solids*; Cambridge University Press, 2016; ISBN 1316571718.

69. Vystavel, T.; Palasantzas, G.; Koch, S.A.; De Hosson, J.T.M. Niobium nanoclusters studied with in situ transmission electron microscopy. *Appl. Phys. Lett.* **2003**, *83*, 3909–3911, doi:10.1063/1.1625789.

70. Vystavel, T.; Palasantzas, G.; Koch, S.A.; De Hosson, J.T.M. Nanosized iron clusters investigated with in situ transmission electron microscopy. *Appl. Phys. Lett.* **2003**, *82*, 197–199, doi:10.1063/1.1536716.

71. Brandes, M.C.; Kovarik, L.; Miller, M.K.; Mills, M.J. Morphology, structure, and chemistry of nanoclusters in a mechanically alloyed nanostructured ferritic steel. *J. Mater. Sci.* **2012**, *47*, 3913–3923, doi:10.1007/s10853-012-6249-x.

72. Van Zwol, P.; Derlet, P.M.; Van Swygenhoven, H.; Dudarev, S.L. BCC Fe surface and cluster magnetism using a magnetic potential. *Surf. Sci.* **2007**, *601*, 3512–3520, doi:https://doi.org/10.1016/j.susc.2007.06.069.

73. Ruvireta, J.; Vega, L.; Viñes, F. Cohesion and coordination effects on transition metal surface energies. *Surf. Sci.* **2017**, *664*, 45–49, doi:https://doi.org/10.1016/j.susc.2017.05.013.

74. Xia, Y.; Xiong, Y.; Lim, B.; Skrabalak, S.E. Shape-controlled synthesis of metal nanocrystals: simple chemistry meets complex physics? *Angew. Chem. Int. Ed. Engl.* **2009**, *48*, 60–103, doi:10.1002/anie.200802248.

75. Tatiparti, S.S. V; Ebrahimi, F. Potentiostatic versus galvanostatic electrodeposition of nanocrystalline Al–Mg alloy powders. *J. Solid State Electrochem.* **2012**, *16*, 1255–1262, doi:10.1007/s10008-011-1522-5.

76. Matsui, M. Study on electrochemically deposited Mg metal. *J. Power Sources* **2011**, *196*, 7048–7055,

doi:https://doi.org/10.1016/j.jpowsour.2010.11.141.

77. Popov, K.I.; Pavlović, M.G.; Maksimović, M.D.; Krstajić, S.S. The comparison of galvanostatic and potentiostatic copper powder deposition on platinum and aluminium electrodes. *J. Appl. Electrochem.* **1978**, *8*, 503–514.

78. Popov, K.I.; Pavlović, M.G.; Maksimović, M.D. Comparison of the critical conditions for initiation of dendritic growth and powder formation in potentiostatic and galvanostatic copper electrodeposition. *J. Appl. Electrochem.* **1982**, *12*, 525–531, doi:10.1007/BF00614978.

79. Banthia, S.; Sengupta, S.; Mallik, M.; Das, S.; Das, K. Substrate effect on electrodeposited copper morphology and crystal shapes. *Surf. Eng.* **2018**, *34*, 485–492.

80. Castro, M.; Cuerno, R.; Nicoli, M.; Vazquez, L.; Buijnsters, J.G. Universality of cauliflower-like fronts: from nanoscale thin films to macroscopic plants. *New J. Phys.* **2012**, *14*, 103039.

81. Orhan, G.; Hapçı, G. Effect of electrolysis parameters on the morphologies of copper powder obtained in a rotating cylinder electrode cell. *Powder Technol.* **2010**, *201*, 57–63, doi:https://doi.org/10.1016/j.powtec.2010.03.003.

82. Kong, C.; Sun, S.; Zhang, J.; Zhao, H.; Song, X.; Yang, Z. Nanocube-aggregated cauliflower-like copper hierarchical architectures: synthesis, growth mechanism and electrocatalytic activity. *CrystEngComm* **2012**, *14*, 5737–5740.

83. OriginPro 2018.

84. Heidari, G.; Mousavi Khoie, S.M.; Abrishami, M.E.; Javanbakht, M.

Electrodeposition of Cu–Sn alloys: theoretical and experimental approaches. *J. Mater. Sci. Mater. Electron.* **2015**, *26*, 1969–1976, doi:10.1007/s10854-014-2636-1.

85. Giurlani, W.; Zangari, G.; Gambinossi, F.; Passaponti, M.; Salvietti, E.; Di Benedetto, F.; Caporali, S.; Innocenti, M. Electroplating for Decorative Applications: Recent Trends in Research and Development. *Coatings* **2018**, *8*, 260, doi:10.3390/coatings8080260.

86. Haumesser, P.-H. *Nucleation and Growth of Metals*; Elsevier, 2016; ISBN 9781785480928.

87. Venables, J A Spiller, G D T and Hanbucken, M. Nucleation and growth of thin films. *Reports Prog. Phys.* **1984**, 399.

88. Giurlani, W.; Giaccherini, A.; Salvietti, E.; Passaponti, M.; Comparini, A.; Morandi, V.; Liscio, F.; Cavallini, M.; Innocenti, M. Selective Electrodesorption-Based Atomic Layer Deposition (SEBALD) of Bismuth under Morphological Control. *Electrochem. Soc. Interface* **2018**, *27*, 77–81, doi:10.1149/2.F08182if.

89. Scharifker, B.; Hills, G. Theoretical and experimental studies of multiple nucleation. *Electrochim. Acta* **1983**, *28*, 879–889, doi:10.1016/0013-4686(83)85163-9.

90. Jacobs, J.W.M. Note on a theory of three-dimensional electrochemical nucleation with diffusion-controlled growth. *J. Electroanal. Chem. Interfacial Electrochem.* **1988**, *247*, 135–144, doi:10.1016/0022-0728(88)80135-9.

91. Scharifker, B.R.; Mostany, J. Three-dimensional nucleation with diffusion controlled growth. *J. Electroanal. Chem. Interfacial Electrochem.* **1984**, *177*, 13–23, doi:10.1016/0022-0728(84)80207-7.

92. Sluyters-Rehbach, M.; Wijenberg, J.H.O.J.; Bosco, E.; Sluyters, J.H. The theory of chronoamperometry for the investigation of electrocrystallization. *J. Electroanal. Chem. Interfacial Electrochem.* **1987**, *236*, 1–20, doi:10.1016/0022-0728(87)88014-2.

93. Zoski, C.G. *Handbook of Electrochemistry*; Elsevier, 2007; ISBN 9780444519580.

94. Gunawardena, G.; Hills, G.; Montenegro, I.; Scharifker, B. Electrochemical nucleation. *J. Electroanal. Chem. Interfacial Electrochem.* **1982**, *138*, 225–239, doi:10.1016/0022-0728(82)85080-8.

95. Isaev, V.A.; Grishenkova, O. V.; Zaykov, Y.P. On the theory of 3D multiple nucleation with kinetic controlled growth. *J. Electroanal. Chem.* **2018**, *818*, 265–269, doi:10.1016/j.jelechem.2018.04.051.

96. Hyde, M.E.; Compton, R.G. A review of the analysis of multiple nucleation with diffusion controlled growth. *J. Electroanal. Chem.* **2003**, *549*, 1–12, doi:10.1016/S0022-0728(03)00250-X.

97. Kosov, A. V.; Grishenkova, O. V.; Semerikova, O.L.; Isaev, V.A.; Zaikov, Y.P. On the theory of cyclic voltammetry for multiple nucleation and growth: Scan rate influence. *J. Electroanal. Chem.* **2021**, *883*, 115056, doi:10.1016/j.jelechem.2021.115056.

98. Martino, T.; Partovi-Nia, R.; Chen, J.; Qin, Z.; Shoesmith, D.W. Mechanisms of Film Growth on Copper in Aqueous Solutions Containing Sulphide and Chloride under Voltammetric Conditions. *Electrochim. Acta* **2014**, *127*, 439–447, doi:10.1016/j.electacta.2014.02.050.

99. Zhang, J.; Li, Y.; Zhang, X.; Yu, Y.; Wang, S. Electrochemical nucleation and growth mechanism of aluminum on AZ31 magnesium

alloys. *Coatings* **2021**, *11*, 1–9, doi:10.3390/coatings11010046.

100. Dekanski, A.; Stevanović, J.; Stevanović, R.; Nikolić, B.Ž.; Jovanović, V.M. Glassy carbon electrodes. *Carbon N. Y.* **2001**, *39*, 1195–1205, doi:10.1016/S0008-6223(00)00228-1.

101. Giurlani, W.; Berretti, E.; Lavacchi, A.; Innocenti, M. Thickness determination of metal multilayers by ED-XRF multivariate analysis using Monte Carlo simulated standards. *Anal. Chim. Acta* **2020**, *1130*, 72–79, doi:10.1016/j.aca.2020.07.047.

102. Yi, Y.; Weinberg, G.; Prenzel, M.; Greiner, M.; Heumann, S.; Becker, S.; Schlögl, R. Electrochemical corrosion of a glassy carbon electrode. *Catal. Today* **2017**, *295*, 32–40, doi:10.1016/j.cattod.2017.07.013.

103. Krishnan, R.M.; Muralidharan, V.S. Electrochemical behaviour of Cu-NTA complexes. In Proceedings of the Proceedings of the Indian Academy of Sciences-Chemical Sciences; Springer, 1991; Vol. 103, pp. 107–118.

104. Wu, J.; Du, X.; He, Z.; Zhang, C.; Fu, D. Statistical investigation on the role of supporting electrolytes during NTA degradation on BDD anodes. *Environ. Sci. Pollut. Res.* **2016**, *23*, 5609–5617, doi:10.1007/s11356-015-5753-3.

105. Cofré, P.; Bustos, A. Voltammetric behaviour of the copper(II)-thiourea system in sulphuric acid medium at platinum and glassy carbon electrodes. *J. Appl. Electrochem.* **1994**, *24*, 564–568, doi:10.1007/BF00249859.

106. Kang, M.S.; Kim, S.-K.; Kim, K.; Kim, J.J. The influence of thiourea on copper electrodeposition: Adsorbate identification and effect on electrochemical nucleation. *Thin Solid Films* **2008**, *516*, 3761–3766,

doi:10.1016/j.tsf.2007.06.069.

107. Stangl, M.; Acker, J.; Oswald, S.; Uhlemann, M.; Gemming, T.; Baunack, S.; Wetzig, K. Incorporation of sulfur, chlorine, and carbon into electroplated Cu thin films. *Microelectron. Eng.* **2007**, *84*, 54–59, doi:10.1016/j.mee.2006.08.004.

108. Bolzán, A.E.; Haseeb, A.S.M.A.; Schilardi, P.L.; Piatti, R.C.V.; Salvarezza, R.C.; Arvia, A.J. Anodisation of copper in thiourea- and formamidine disulphide-containing acid solution. Part I. Identification of products and reaction pathway. *J. Electroanal. Chem.* **2001**, *500*, 533–542, doi:10.1016/S0022-0728(00)00217-5.

109. Alodan, M.; Smyrl, W. Effect of thiourea on copper dissolution and deposition. *Electrochim. Acta* **1998**, *44*, 299–309, doi:10.1016/S0013-4686(98)00060-7.

110. Kirchnerová, J.; Purdy, W.C. The mechanism of the electrochemical oxidation of thiourea. *Anal. Chim. Acta* **1981**, *123*, 83–95, doi:10.1016/S0003-2670(01)83161-5.

111. Bolzán, A.E.; Wakenge, I.B.; Piatti, R.C.V.; Salvarezza, R.C.; Arvia, A.J. The behaviour of copper anodes in aqueous thiourea-containing sulphuric acid solutions. Open circuit potentials and electrochemical kinetics. *J. Electroanal. Chem.* **2001**, *501*, 241–252, doi:10.1016/S0022-0728(00)00535-0.

112. Yarnitzky, Ch.; Schreiber-Stanger, R. Adsoprtion stripping square-wave voltammetry of copper ions in the presence of thiourea. *J. Electroanal. Chem* **1986**, *214*, 65–78.

113. Riveros, G.; León, M.; Ramírez, D.; Hernández, L.; Martín, F.; Romero, R.; Dalchiele, E.A. Study of the Nucleation and Growth Mechanisms

of Copper Electrodeposition on Bare and Nitrogen-Doped Reduced Graphene Oxide Modified SnO 2 :F/glass Substrates . *J. Electrochem. Soc.* **2020**, *167*, 122508, doi:10.1149/1945-7111/abb281.

114. Sun, M.; O'Keefe, T.J. The effect of additives on the nucleation and growth of copper onto stainless steel cathodes. *Metall. Trans. B* **1992**, *23*, 591–599, doi:10.1007/BF02649719.

115. Grujicic, D.; Pesic, B. Electrodeposition of copper: the nucleation mechanisms. *Electrochim. Acta* **2002**, *47*, 2901–2912, doi:https://doi.org/10.1016/S0013-4686(02)00161-5.

116. Fabricius, G.; Kontturi, K.; Sundholm, G. Influence of thiourea on the nucleation of copper from acid sulphate solutions. *Electrochim. Acta* **1994**, *39*, 2353–2357, doi:10.1016/0013-4686(94)00207-X.

117. Martínez-Ruíz, A.; Palomar-Pardavé, M.; Batina, N. Overpotential deposition of copper on an iodine-modified Au(111) electrode. *Electrochim. Acta* **2008**, *53*, 2115–2120, doi:10.1016/j.electacta.2007.09.011.

118. Palomar-Pardavé, M.; González, I.; Batina, N. New Insights into Evaluation of Kinetic Parameters for Potentiostatic Metal Deposition with Underpotential and Overpotential Deposition Processes. *J. Phys. Chem. B* **2000**, *104*, 3545–3555, doi:10.1021/jp9931861.

119. Shafiee, S.; Topal, E. When will fossil fuel reserves be diminished? *Energy Policy* **2009**, *37*, 181–189, doi:10.1016/j.enpol.2008.08.016.

120. Murphy, D.J.; Hall, C.A.S. Year in review-EROI or energy return on (energy) invested. *Ann. N. Y. Acad. Sci.* **2010**, *1185*, 102–118, doi:10.1111/j.1749-6632.2009.05282.x.

121. Bardi, U. Energy Prices and Resource Depletion: Lessons from the Case of Whaling in the Nineteenth Century. *Energy Sources, Part B Econ. Planning, Policy* **2007**, *2*, 297–304, doi:10.1080/15567240600629435.

122. Hall, C.A.S.; Lambert, J.G.; Balogh, S.B. EROI of different fuels and the implications for society. *Energy Policy* **2014**, *64*, 141–152, doi:10.1016/j.enpol.2013.05.049.

123. Johnson, E. Climate Change Policy: A Survey. *Environ. Impact Assess. Rev.* **2003**, *23*, 127, doi:10.1016/S0195-9255(02)00103-8.

124. Office of Energy Efficiency & Renewable Energy 2016-2020 Strategic Plan and Implementing Framework. **2016**, 36.

125. Smith, W. The role of fuel cells in energy storage. *J. Power Sources* **2000**, *86*, 74–83, doi:10.1016/S0378-7753(99)00485-1.

126. Carrette, L.; Friedrich, K.A.; Stimming, U. Fuel Cells - Fundamentals and Applications. *Fuel Cells* **2001**, *1*, 5–39, doi:10.1002/1615-6854(200105)1:1<5::aid-fuce5>3.0.co;2-g.

127. *Fuel Cell Systems*; Blomen, L.J.M.J., Mugerwa, M.N., Eds.; Springer US: Boston, MA, 1993; ISBN 978-1-4899-2426-1.

128. Bard, A.J.; Faulkner, L.R. *Electrochemical Methods: Fundamentals and Applications, 2nd Edition*; John Wiley & Sons, 2000; ISBN 9781118312803.

129. Curzon, F.L.; Ahlborn, B. Efficiency of a Carnot engine at maximum power output. *Am. J. Phys.* **1975**, *43*, 22–24, doi:10.1119/1.10023.

130. Katsounaros, I.; Schneider, W.B.; Meier, J.C.; Benedikt, U.; Biedermann, P.U.; Auer, A.A.; Mayrhofer, K.J.J. Hydrogen peroxide electrochemistry on platinum: towards understanding the oxygen

reduction reaction mechanism. *Phys. Chem. Chem. Phys.* **2012**, *14*, 7384, doi:10.1039/c2cp40616k.

131. Wang, B. Recent development of non-platinum catalysts for oxygen reduction reaction. *J. Power Sources* **2005**, *152*, 1–15, doi:10.1016/j.jpowsour.2005.05.098.

132. Pantea, D.; Darmstadt, H.; Kaliaguine, S.; Roy, C. Heat-treatment of carbon blacks obtained by pyrolysis of used tires. Effect on the surface chemistry, porosity and electrical conductivity. *J. Anal. Appl. Pyrolysis* **2003**, *67*, 55–76, doi:10.1016/S0165-2370(02)00017-7.

133. Gasparatos, A.; von Maltitz, G.P.; Johnson, F.X.; Lee, L.; Mathai, M.; Puppim de Oliveira, J.A.; Willis, K.J. Biofuels in sub-Sahara Africa: Drivers, impacts and priority policy areas. *Renew. Sustain. Energy Rev.* **2015**, *45*, 879–901, doi:10.1016/j.rser.2015.02.006.

134. Chen, K.-S.; Lin, Y.-C.; Hsu, K.-H.; Wang, H.-K. Improving biodiesel yields from waste cooking oil by using sodium methoxide and a microwave heating system. *Energy* **2012**, *38*, 151–156, doi:10.1016/j.energy.2011.12.020.

135. Wang, Y.; Balbuena, P.B. Design of Oxygen Reduction Bimetallic Catalysts: Ab-Initio-Derived Thermodynamic Guidelines. *J. Phys. Chem. B* **2005**, *109*, 18902–18906, doi:10.1021/jp0543779.

136. Yang, D.-S.; Chaudhari, S.; Rajesh, K.P.; Yu, J.-S. Preparation of Nitrogen-Doped Porous Carbon Nanofibers and the Effect of Porosity, Electrical Conductivity, and Nitrogen Content on Their Oxygen Reduction Performance. *ChemCatChem* **2014**, n/a-n/a, doi:10.1002/cctc.201400035.

137. Eisenberg, D.; Stroek, W.; Geels, N.J.; Sandu, C.S.; Heller, A.; Yan, N.;

Rothenberg, G. A Simple Synthesis of an N-Doped Carbon ORR Catalyst: Hierarchical Micro/Meso/Macro Porosity and Graphitic Shells. *Chem. - A Eur. J.* **2016**, *22*, 501–505, doi:10.1002/chem.201504568.

138. Ansari, M.S.; Jebakumar Immanuel Edison, T.N.; Lee, Y.R. Enhanced electrocatalytic and supercapacitive performance using the synergistic effect of defect-rich N/S co-doped hierarchical porous carbon. *Sustain. Energy Fuels* **2020**, *4*, 5697–5708, doi:10.1039/D0SE00980F.

139. Khan, Z.; Park, S.O.; Yang, J.; Park, S.; Shanker, R.; Song, H.-K.; Kim, Y.; Kwak, S.K.; Ko, H. Binary N,S-doped carbon nanospheres from bio-inspired artificial melanosomes: A route to efficient air electrodes for seawater batteries. *J. Mater. Chem. A* **2018**, *6*, 24459–24467, doi:10.1039/C8TA10327E.

140. Kim, S.; Park, H.; Li, O.L. Cobalt Nanoparticles on Plasma-Controlled Nitrogen-Doped Carbon as High-Performance ORR Electrocatalyst for Primary Zn-Air Battery. *Nanomaterials* **2020**, *10*, 223, doi:10.3390/nano10020223.

141. Welch, C.M.; Compton, R.G. The use of nanoparticles in electroanalysis: a review. *Anal. Bioanal. Chem.* **2006**, *384*, 601–619, doi:10.1007/s00216-005-0230-3.

142. Kaluža, L.; Larsen, M.J.; Zdražil, M.; Gulková, D.; Vít, Z.; Šolcová, O.; Soukup, K.; Koštejn, M.; Bonde, J.L.; Maixnerová, L.; et al. Highly loaded carbon black supported Pt catalysts for fuel cells. *Catal. Today* **2015**, *256*, 375–383, doi:10.1016/j.cattod.2015.02.016.

143. Kaluža, L.; Larsen, M.J.; Morales, I.J.; Cavaliere, S.; Jones, D.J.; Rozière, J.; Kallistová, A.; Dytrych, P.; Gulková, D.; Odgaard, M. Synthesis of

Pt/C Fuel Cell Electrocatalysts: Residual Content of Chloride and Activity in Oxygen Reduction. *Electrocatalysis* **2016**, *7*, 269–275, doi:10.1007/s12678-016-0312-3.

144. Liu, S.; Yu, J.; Ju, H. Renewable phenol biosensor based on a tyrosinase-colloidal gold modified carbon paste electrode. *J. Electroanal. Chem.* **2003**, *540*, 61–67, doi:10.1016/S0022-0728(02)01276-7.

145. Undri, A.; Sacchi, B.; Cantisani, E.; Toccafondi, N.; Rosi, L.; Frediani, M.; Frediani, P. Carbon from microwave assisted pyrolysis of waste tires. *J. Anal. Appl. Pyrolysis* **2013**, *104*, 396–404, doi:10.1016/j.jaap.2013.06.006.

146. Passaponti, M.; Rosi, L.; Frediani, M.; Salvietti, E.; De Luca, A.; Giaccherini, A.; Innocenti, M. Microwave Assisted Pyrolysis of Waste Tires: Study and Design of Half-Cells SOFCs with Low Environmental Impact. *ECS Trans.* **2017**, *78*, 1933–1940, doi:10.1149/07801.1933ecst.

147. Wang, huihua; Wang, C.; Liu, L.; Qu, T.; Wang, D.; Kang, Z. Synthesis of Co-Fe-Pd nanoparticles via ultrasonic irradiation and their electro-catalytic activity for oxygen reduction reaction. *Appl. Catal. A Gen.* **2018**, *560*, 103–110, doi:10.1016/j.apcata.2018.04.034.

148. Ruiz-Camacho, B.; Martínez Álvarez, O.; Rodríguez-Santoyo, H.H.; López-Peréz, P.A.; Fuentes-Ramírez, R. Mono and bi-metallic electrocatalysts of Pt and Ag for oxygen reduction reaction synthesized by sonication. *Electrochem. commun.* **2015**, *61*, 5–9, doi:10.1016/j.elecom.2015.09.023.

149. Zafferoni, C.; Cioncoloni, G.; Foresti, M.; Dei, L.; Carretti, E.; Vizza, F.; Lavacchi, A.; Innocenti, M. Synergy of Cobalt and Silver Microparticles Electrodeposited on Glassy Carbon for the

Electrocatalysis of the Oxygen Reduction Reaction: An Electrochemical Investigation. *Molecules* **2015**, *20*, 14386–14401, doi:10.3390/molecules200814386.

150. Lari, L.; Nuttall, C.J.; Copley, M.P.; Potter, R.J.; Simon, J.; Mingo, N.; Ozkaya, D. Characterization of nanoembedded alloyed thermoelectrics. *J. Phys. Conf. Ser.* **2014**, *522*, 012040, doi:10.1088/1742-6596/522/1/012040.

151. Muniz-Miranda, M.; Muniz-Miranda, F.; Caporali, S.; Calisi, N.; Pedone, A. SERS, XPS and DFT investigation on palladium surfaces coated with 2,2'-bipyridine monolayers. *Appl. Surf. Sci.* **2018**, *457*, 98–103, doi:10.1016/j.apsusc.2018.06.232.

152. Calisi, N.; Caporali, S.; Milanesi, A.; Innocenti, M.; Salvietti, E.; Bardi, U. Composition-Dependent Degradation of Hybrid and Inorganic Lead Perovskites in Ambient Conditions. *Top. Catal.* **2018**, *61*, 1201–1208, doi:10.1007/s11244-018-0922-5.

153. Borri, C.; Calisi, N.; Galvanetto, E.; Falsini, N.; Biccari, F.; Vinattieri, A.; Cucinotta, G.; Caporali, S. First Proof-of-Principle of Inorganic Lead Halide Perovskites Deposition by Magnetron-Sputtering. *Nanomaterials* **2019**, *10*, 60, doi:10.3390/nano10010060.

154. Bagotzky, V.S.; Tarasevich, M.R.; Radyushkina, K.A.; Levina, O.A.; Andrusyova, S.I. Electrocatalysis of the oxygen reduction process on metal chelates in acid electrolyte. *J. Power Sources* **1978**, *2*, 233–240, doi:10.1016/0378-7753(78)85014-9.

155. Passaponti, M.; Savastano, M.; Clares, M.P.; Inclán, M.; Lavacchi, A.; Bianchi, A.; García-España, E.; Innocenti, M. MWCNTs-Supported Pd(II) Complexes with High Catalytic Efficiency in Oxygen Reduction

Reaction in Alkaline Media. *Inorg. Chem.* **2018**, *57*, 14484–14488, doi:10.1021/acs.inorgchem.8b02695.

156. Medford, A.J.; Vojvodic, A.; Hummelshøj, J.S.; Voss, J.; Abild-Pedersen, F.; Studt, F.; Bligaard, T.; Nilsson, A.; Nørskov, J.K. From the Sabatier principle to a predictive theory of transition-metal heterogeneous catalysis. *J. Catal.* **2015**, *328*, 36–42, doi:10.1016/j.jcat.2014.12.033.

157. Passaponti, M.; Rosi, L.; Savastano, M.; Giurlani, W.; Miller, H.A.; Lavacchi, A.; Filippi, J.; Zangari, G.; Vizza, F.; Innocenti, M. Recycling of waste automobile tires: Transforming char in oxygen reduction reaction catalysts for alkaline fuel cells. *J. Power Sources* **2019**, *427*, 85–90, doi:10.1016/j.jpowsour.2019.04.067.

158. PATEL, N.; PATTON, B.; ZANCHETTA, C.; FERNANDES, R.; GUELLA, G.; KALE, A.; MIOTELLO, A. Pd-C powder and thin film catalysts for hydrogen production by hydrolysis of sodium borohydride. *Int. J. Hydrogen Energy* **2008**, *33*, 287–292, doi:10.1016/j.ijhydene.2007.07.018.

159. Adams, B.D.; Chen, A. The role of palladium in a hydrogen economy. *Mater. Today* **2011**, *14*, 282–289, doi:10.1016/S1369-7021(11)70143-2.

160. Bambagioni, V.; Bianchini, C.; Marchionni, A.; Filippi, J.; Vizza, F.; Teddy, J.; Serp, P.; Zhiani, M. Pd and Pt–Ru anode electrocatalysts supported on multi-walled carbon nanotubes and their use in passive and active direct alcohol fuel cells with an anion-exchange membrane (alcohol=methanol, ethanol, glycerol). *J. Power Sources* **2009**, *190*, 241–251, doi:10.1016/j.jpowsour.2009.01.044.

161. Miller, H.A.; Lavacchi, A.; Vizza, F.; Marelli, M.; Di Benedetto, F.;

D'Acapito, F.; Paska, Y.; Page, M.; Dekel, D.R. A Pd/C-CeO 2 Anode Catalyst for High-Performance Platinum-Free Anion Exchange Membrane Fuel Cells. *Angew. Chemie Int. Ed.* **2016**, *55*, 6004–6007, doi:10.1002/anie.201600647.

162. Calderón Gómez, J.; Moliner, R.; Lázaro, M. Palladium-Based Catalysts as Electrodes for Direct Methanol Fuel Cells: A Last Ten Years Review. *Catalysts* **2016**, *6*, 130, doi:10.3390/catal6090130.

163. Tsuda, T.; Choi, S.-M.; Shintani, R. Palladium-Catalyzed Synthesis of Dibenzosilepin Derivatives via 1, n -Palladium Migration Coupled with anti -Carbopalladation of Alkyne. *J. Am. Chem. Soc.* **2021**, *143*, 1641–1650, doi:10.1021/jacs.0c12453.

164. Du, S.; Wang, W.-F.; Song, Y.; Chen, Z.; Wu, X.-F. Palladium-Catalyzed Cascade Carbonylative Synthesis of 1,2,4-Triazol-3-ones from Hydrazonoyl Chlorides and NaN 3. *Org. Lett.* **2021**, *23*, 974–978, doi:10.1021/acs.orglett.0c04167.

165. Kitamura, Y.; Murata, Y.; Iwai, M.; Matsumura, M.; Yasuike, S. Palladium-Catalyzed C–H Arylation of Benzofurans with Triarylantimony Difluorides for the Synthesis of 2-Arylbenzofurans. *Molecules* **2020**, *26*, 97, doi:10.3390/molecules26010097.

166. Greenwood, N.N.; Earnshaw, A. Chemistry of the Elements (1st Edition). **1984**, 268–327.

167. Hobson, P. *Reuters*. 2020,.

168. Vigne, S.A.; Lucey, B.M.; O'Connor, F.A.; Yarovaya, L. The financial economics of white precious metals — A survey. *Int. Rev. Financ. Anal.* **2017**, *52*, 292–308, doi:10.1016/j.irfa.2017.04.006.

169. Djokić, S.S. Electroless Deposition of Metals and Alloys. In *Modern Aspects of Electrochemistry*; Conway, B.E., White, R.E., Eds.; Springer US: Boston, MA, 2002; pp. 51–133 ISBN 978-0-306-47604-4.

170. Luo, Q.; Mackay, R.A.; Babu, S. V. Copper Dissolution in Aqueous Ammonia-Containing Media during Chemical Mechanical Polishing. *Chem. Mater.* **1997**, *9*, 2101–2106, doi:10.1021/cm970168s.

171. Djokić, S.S. Electroless Deposition of Palladium Using Hypophosphite as a Reducing Agent. *Plat. Surf. Finish.* **1999**, *86*, 104–107.

172. Pearlstein, F.; Weightman, R. Electroless Deposition of Palladium Alloys. **1973**.

173. Mallory, G.O.; Hajdu, J.B. *Electroless Plating*; 1st ed.; Elsevier, 1990; ISBN 9780815512776.

174. Fujinami, T.; Watanabe, J.; Honma, H. Catalytic activity and stability of mixed PdCl2/SnCl2 catalysts. *Trans. Inst. Met. Finish.* **1996**, *74*, 193–197, doi:10.1080/00202967.1996.11871125.

175. Hamaya, T.; Kumagai, Y.; Koshizaki, N.; Kanbe, T. Electroless Plating through Successive Pretreatment with Aminosilane and PdCl 2 . *Chem. Lett.* 1989, *18*, 1461–1464.

176. Johnson, R.W. Immersion Plating of the Platinum Group Metals. *J. Electrochem. Soc.* **1961**, *108*, 632, doi:10.1149/1.2428179.

177. Paunovic, M. Electroless Deposition of Metals and Alloys. *Electrochem. Transit.* **1992**, 479–497, doi:10.1007/978-1-4615-9576-2_30.

178. Ohno, I. Electroless Deposition of Alloys. *Mod. Electroplat. Fifth Ed.* **2011**, 499–506, doi:10.1002/9780470602638.ch22.

179. Magagnin, L.; Maboudian, R.; Carraro, C. Gold Deposition by

Galvanic Displacement on Semiconductor Surfaces: Effect of Substrate on Adhesion. *J. Phys. Chem. B* **2002**, *106*, 401–407, doi:10.1021/jp013396p.

180. CARRARO, C.; MABOUDIAN, R.; MAGAGNIN, L. Metallization and nanostructuring of semiconductor surfaces by galvanic displacement processes. *Surf. Sci. Rep.* **2007**, *62*, 499–525, doi:10.1016/j.surfrep.2007.08.002.

181. Chen, L.; Liu, Y. Synthesis and characterization of dendritic and porous Ag–Pd alloy nanostructures. *J. Colloid Interface Sci.* **2011**, *364*, 100–106, doi:10.1016/j.jcis.2011.08.018.

182. Wang, D.; Li, T.; Liu, Y.; Huang, J.; You, T. Large-Scale and Template-Free Growth of Free-Standing Single-Crystalline Dendritic Ag/Pd Alloy Nanostructure Arrays. *Cryst. Growth Des.* **2009**, *9*, 4351–4355, doi:10.1021/cg900217t.

183. Kokkinidis, G.; Papoutsis, A.; Stoychev, D.; Milchev, A. Electroless deposition of Pt on Ti—catalytic activity for the hydrogen evolution reaction. *J. Electroanal. Chem.* **2000**, *486*, 48–55, doi:10.1016/S0022-0728(00)00128-5.

184. Porter, L.A.; Choi, H.C.; Ribbe, A.E.; Buriak, J.M. Controlled Electroless Deposition of Noble Metal Nanoparticle Films on Germanium Surfaces. *Nano Lett.* **2002**, *2*, 1067–1071, doi:10.1021/nl025677u.

185. Wang, Z.; Ida, T.; Sakaue, H.; Shingubara, S.; Takahagi, T. Electroless Plating of Copper on Metal-Nitride Diffusion Barriers Initiated by Displacement Plating. *Electrochem. Solid-State Lett.* **2003**, *6*, C38, doi:10.1149/1.1541255.

186. Djokić, S.S. Cementation of Copper on Aluminum in Alkaline Solutions. *J. Electrochem. Soc.* **1996**, *143*, 1300–1305, doi:10.1149/1.1836634.

187. Hutt, D.A.; Liu, C.; Conway, P.P.; Whalley, D.C.; Mannan, S.H. Electroless nickel bumping of aluminum bondpads. I. Surface pretreatment and activation. *IEEE Trans. Components Packag. Technol.* **2002**, *25*, 87–97, doi:10.1109/6144.991180.

188. Hutt, D.A.; Liu, C.; Conway, P.P.; Whalley, D.C.; Mannan, S.H. Electroless nickel bumping of aluminum bondpads. II. Electroless nickel plating. *IEEE Trans. Components Packag. Technol.* **2002**, *25*, 98–105, doi:10.1109/6144.991181.

189. Watanabe, H.; Honma, H. Fabrication of Nickel Microbump on Aluminium Substrate Using Electroless Nickel Plating. *Trans. IMF* **1996**, *74*, 138–141, doi:10.1080/00202967.1996.11871113.

190. Qu, L.; Dai, L.; Osawa, E. Shape/Size-Controlled Syntheses of Metal Nanoparticles for Site-Selective Modification of Carbon Nanotubes. *J. Am. Chem. Soc.* **2006**, *128*, 5523–5532, doi:10.1021/ja060296u.

191. Mabbott, S.; Larmour, I.A.; Vishnyakov, V.; Xu, Y.; Graham, D.; Goodacre, R. The optimisation of facile substrates for surface enhanced Raman scattering through galvanic replacement of silver onto copper. *Analyst* **2012**, *137*, 2791, doi:10.1039/c2an35323g.

192. Liu, Y.-C.; Yang, S.-J. Improved surface-enhanced Raman scattering based on Ag–Au bimetals prepared by galvanic replacement reactions. *Electrochim. Acta* **2007**, *52*, 1925–1931, doi:10.1016/j.electacta.2006.07.057.

193. Ojani, R.; Raoof, J.B.; Hasheminejad, E. One-step electroless

deposition of Pd/Pt bimetallic microstructures by galvanic replacement on copper substrate and investigation of its performance for the hydrogen evolution reaction. *Int. J. Hydrogen Energy* **2013**, *38*, 92–99, doi:10.1016/j.ijhydene.2012.10.015.

194. Ojani, R.; Raoof, J.B.; Hasheminejad, E. One-step electroless deposition of Pd/Pt bimetallic microstructures by galvanic replacement on copper substrate and investigation of its performance for the hydrogen evolution reaction. *Int. J. Hydrogen Energy* **2013**, *38*, 92–99, doi:10.1016/j.ijhydene.2012.10.015.

195. Nobari, N.; Behboudnia, M.; Maleki, R. Palladium-free electroless deposition of pure copper film on glass substrate using hydrazine as reducing agent. *Appl. Surf. Sci.* **2016**, *385*, 9–17, doi:10.1016/j.apsusc.2016.05.033.

196. Kim, K.H.; Lim, T.; Park, K.J.; Koo, H.C.; Kim, M.J.; Kim, J.J. Investigation of Cu growth phenomena on Ru substrate during electroless deposition using hydrazine as a reducing agent. *Electrochim. Acta* **2015**, *151*, 249–255, doi:10.1016/j.electacta.2014.11.036.

197. Bulasara, V.K.; Thakuria, H.; Uppaluri, R.; Purkait, M.K. Nickel-ceramic composite membranes: Optimization of hydrazine based electroless plating process parameters. *Desalination* **2011**, *275*, 243–251, doi:10.1016/j.desal.2011.03.009.

198. Muench, F.; Oezaslan, M.; Svoboda, I.; Ensinger, W. Electroless plating of ultrathin palladium films: Self-initiated deposition and application in microreactor fabrication. *Mater. Res. Express* **2015**, *2*, doi:10.1088/2053-1591/2/10/105010.

199. Niemeier, J.K.; Kjell, D.P. Hydrazine and Aqueous Hydrazine

Solutions: Evaluating Safety in Chemical Processes. *Org. Process Res. Dev.* **2013**, *17*, 1580–1590, doi:10.1021/op400120g.

200. Giurlani, W.; Berretti, E.; Innocenti, M.; Lavacchi, A. Measuring the Thickness of Metal Coatings: A Review of the Methods. *Coatings* **2020**, *10*, 1211, doi:10.3390/coatings10121211.

201. Giurlani, W.; Innocenti, M.; Lavacchi, A. X-ray microanalysis of precious metal thin films: Thickness and composition determination. *Coatings* **2018**, *8*, doi:10.3390/coatings8020084.

202. NIST DTSA-II software Available online: https://www.nist.gov/services-resources/software/nist-dtsa-ii.

203. Abadias, G.; Chason, E.; Keckes, J.; Sebastiani, M.; Thompson, G.B.; Barthel, E.; Doll, G.L.; Murray, C.E.; Stoessel, C.H.; Martinu, L. Review Article: Stress in thin films and coatings: Current status, challenges, and prospects. *J. Vac. Sci. Technol. A Vacuum, Surfaces, Film.* **2018**, *36*, 020801, doi:10.1116/1.5011790.

204. Engwall, A.M.; Rao, Z.; Chason, E. Origins of residual stress in thin films: Interaction between microstructure and growth kinetics. *Mater. Des.* **2016**, *110*, 616–623, doi:10.1016/j.matdes.2016.07.089.

205. Chason, E.; Engwall, A.; Pei, F.; Lafouresse, M.; Bertocci, U.; Stafford, G.; Murphy, J.A.; Lenihan, C.; Buckley, D.N. Understanding Residual Stress in Electrodeposited Cu Thin Films. *J. Electrochem. Soc.* **2013**, *160*, D3285–D3289, doi:10.1149/2.048312jes.

206. Giurlani, W.; Berretti, E.; Innocenti, M.; Lavacchi, A. Coating Thickness Determination Using X-ray Fluorescence Spectroscopy: Monte Carlo Simulations as an Alternative to the Use of Standards. *Coatings* **2019**, *9*, 79, doi:10.3390/coatings9020079.